Spring 5-17-2013

Studies on Structure and Property of Polymer-based Nano-composite Materials

Yun Zhai
yzhai@my.uno.edu

Studies on Structure and Property of Polymer-based Nano-composite Materials

A Dissertation

Submitted to the Graduate Faculty of the
University of New Orleans
in partial fulfillment of the
requirements for the degree of

Doctor of Philosophy
in
Engineering and Applied Science
Mechanical Engineering

by

Yun Zhai

B.S. Southwest JiaoTong University, Chenddu, China, 2006
M.S. Southwest JiaoTong University, Chengdu, China, 2008

May, 2013

DEDICATION

To my parents：翟永斌 and 胡晓红

ACKNOWLEDGEMENT

First of all, I would like to show my thankfulness to my chief advisor Prof. David Hui for the opportunity to work with him on this promising project. Discussions with Prof. Hui always enlightened me a lot and helped to save me large amount of time on the experiment design. I would also like to thank Prof. Hui for offering me opportunity to travel to other research center and collecting valuable data from advanced facilities. His patience with me, guidance for my research and wise suggestion will always be deeply appreciated.

I would like to thank Dr. Kazim Akyuzlu, Dr. Weilie Zhou, Dr. Huimin Chen, and Dr. Hall Carsie for serving on my committee.

Acknowledgements are also due to the Defense Advanced Research Projects Agency for their financial support and Advanced Materials Research Institute at University of New Orleans for their advanced facilities and resources.

I am thankful to Dr. Kazim M. Akyuzlu, Dr. Dongming Wei, Dr. Carsie A. Hall, Dr. Weilie Zhou, Dr. Salvadore Guccione, Dr. Kenneth Holladay for all they have taught me and all the help they offered. Special thanks to Dr. Weilie Zhou's PhD student Kai Wang and postdoctoral Dr. Baobao Cao for the assistance on the training of scanning electron microscope and transmission electron microscopy.

I would also like to express my gratitude towards Prof. Mircea Chipara, University of Texas Pan American, for his advices, patience, and gentleness during my stay in Edinburg. Prof. Chipara's excellent physical view helped me a lot on the

experimental data interpretation. I also want to thank Prof. Chipara for the assistance on Raman spectroscopy characterization which helped me to identify the carbon nanotube feature in the composite materials.

Finally, I would like to thank my family for their unconditional love. Their encouragement and support are always my driving force on my academic development.

TABLE OF CONTENTS

ABSTRACT viii
CHAPTER 1 LITERATURE REVIEW 1
1.1. Introduction and Background 1
1.2. Layered Nano-Inclusion and Polymer Matrix 3
1.3. Structure of Single Wall Carbon Nanotube 6
1.4. Electronic Properties of Nanotubes 8
1.5. Mechanical Properties of Carbon Nanotubes 11
1.6. Application of Atomic Force Microscope 14
1.7. Raman Spectroscopy 20
1.8. Dispersion of Nanotube in Polymer 24
1.9. Fabrication of Nanotube/Polymer Composite 27
1.9.1 Solution Blending 27
1.9.2 Melt Blending 29
1.9.3 In Situ Polymerization 33
1.10. Application of Carbon Nanotube Composites 35
CHAPTER 2 TITANIUM DIOXIDE AND POLYANILINE COMPOSITE 36
2.1 Thermoelectric Effect and Applications 36
2.1.1 Seebeck Effect 36
2.1.2 Peltier Effect 38
2.1.3 Thomson Effect 38
2.1.4 Application of Thermoelectric Devices 39
2.2 Titanium Dioxide and Polyaniline Composite 41
2.3 Synthesis of TiO_2/PANI Nano-composites 42
2.4 Characterization of TiO_2/PANI Nano-composites 45
2.4.1 Scanning Electron Microscopy 45
2.4.2 X-Ray Powder Diffraction 47
2.4.3 Fourier Transform Infrared Spectroscopy 49
2.4.4 Thermogravimetry Analysis 52

2.4.5 Electrical Conductivity Measurement 54
2.4.5 The Seebeck coefficient Measurement 56
2.4.6 Figure of Merit 58
2.5 Summery 60
CHAPTER 3 POLYSTYRENE-ANATASE TITANIUM DIOXIDE NANOCOMPOSITE 61
3.1 Synthesis of Polystyrene/TiO_2 composites 61
3.2 Thermogravimetric Analysis 63
3.2.1 Introduction of TGA Curve and Avrami Equation 63
3.2.2 Interface between Polymer and Nanoparticles 65
3.2.3 Experimental Results and Discussions 65
3.2.4 Mathematical Simulation on Thermal Analysis 68
3.3 Raman Spectroscopy and Wide-angle X-ray Scattering 73
CHAPTER 4 POLYSTYRENE-POLYANILINE-TIO_2 TERNARY POLYMERIC NANOCOMPOSITE 78
4.1 Introduction 78
4.2 Methodology 80
4.3 Experimental Data 82
4.4 Conclusion 86
CHAPTER 5 POLYETHYLENE OXIDE-TIO_2 NANOCOMPOSITES 87
5.1 Introduction 87
5.2 Methodology 89
5.3 Experimental Data 90
5.4 Conclusion 104
CHAPTER 6 VINYL ACETATE-ETHYLENE AND CARBON NANOTUBE COMPOSITES 105
6.1 Structure Introduction 105
6.1.1 Single Wall Carbon Nanotube 105
6.1.2 Vinyl Acetate-ethylene Copolymer 108
6.1.3 Poly(3,4-ethylenedioxythiophene)/poly(styrenesulfonate) 110
6.1.4 Networks Created With a Polymer Emulsion 111
6.2 Processing Methods 113
6.2.1 Nanodebee 113
6.2.2 Production line 115
6.3 Experimental data 117

6.3.1 Scanning Electron Microscope Characterization 117
6.3.2 Raman Spectroscopy Characterization 119
6.3.3 Atomic Force Microscope Characterization 123
6.4 Calculation of Conducting Percolation in SWNT Composites 130
6.4.1 Assumptions 130
6.4.2 Calculation 133
CHAPTER 7 SUMMARY AND FUTURE WORK 136
REFERENCES 142
VITA 153

ABSTRACT

The mixing of polymers and nanoparticles makes it possible to give advantageous macroscopic material performance by tailoring the microstructure of composites. In this thesis, five combinations of nano inclusion and polymer matrix have been investigated.

The first type of composites is titanium dioxide/ polyaniline combination. The effects of 4 different doping-acids on the microstructure, morphology, thermal stability and thermoelectric properties were discussed, showing that the sample with HCl and sulfosalicylic dual acids gave a better thermoelectric property. The second combination is titanium dioxide/polystyrene composite. Avrami equation was used to investigate the crystallization process. The best fit of the mass derivative dependence on temperature has been obtained using the double Gaussian dependence. The third combination is titanium dioxide/polyaniline/ polystyrene. In the titanium dioxide/polyaniline/ polystyrene ternary system, polystyrene provides the mechanical strength supporting the whole structure; TiO_2 nanoparticles are the thermoelectric component; Polyaniline (PANI) gives the additional boost to the electrical conductivity. We also did some investigations on Polyethylene odide-TiO_2 composite. The cubic anatase TiO_2 with an average size of 13nm was mixed with Polyethylene-oxide using Nano Debee equipment from BEE international;

Single wall carbon nanotubes were introduced into the vinyl acetate-ethylene copolymer (VAE) to form a connecting network, using high pressure homogenizer (HPH). The processing time has been reduced to 1/60 of sonication for HPH to give better

sample quality. Theoretical percolation was derived according to the excluded volume theory, turning out the threshold (ϕ_c) as a function of aspect ratio (A) to be $\phi_c = 1 - \exp\left(-\frac{28+42A}{160+240A+60A^2}\right)$.

Key words: Single wall carbon nanotube, polymer, titanium dioxide, thermoelectric, percolation threshold, high pressure homogenizer.

CHAPTER 1 LITERATURE REVIEW

1.1. Introduction and Background

Polymer composites have broad applications in industry products, such as sporting goods, aerospace components, automobile, because the composite material combines the excellent physical properties of the Nano filler and the mechanical stability of the polymer matrix. The clay-reinforced resin was introduced in the early 1900's as one of the first mass-produced polymer-nanoparticle composites[1]. In early 1990s, Toyota researchers revealed the introduction of mica into nylon produced a five-fold increase in the yield and tensile strength of the material[2]. After that, the polymer-nanoparticle composites became a popular research area in material science and engineering. The final products do not have to be in nanoscale, but can be micro- or macroscopic in size. This surge in the field of nanotechnology has been greatly facilitated by the application of scanning tunneling microscopy and scanning probe microscopy in the early 1980s[3]. Also the increasing application of computer modeling and simulation has made it easier to design and predict the material performance at the nanoscale[4].

The material physical properties changes significantly when micro particles transits to nanoparticles. One main character of nanoscale materials is the large surface for a given volume. When the particle size transits from micro to nanoscale, the physical properties changes dramatically because many chemical and physical interaction are governed by the surface properties.

Figure 1.1 is the common particle geometries and their surface area-to–volume ratios. The area-to-volume ratios are dominated by the first term in the equation especially for the fiber and layered material. The second term (2/l and 4/l) is often omitted compared to the first term. Therefore when the particle diameter, layer thickness and fibrous material diameter change from micrometer to nanometer, the surface area-to-volume ratio will be affected by three orders of magnitude[5].

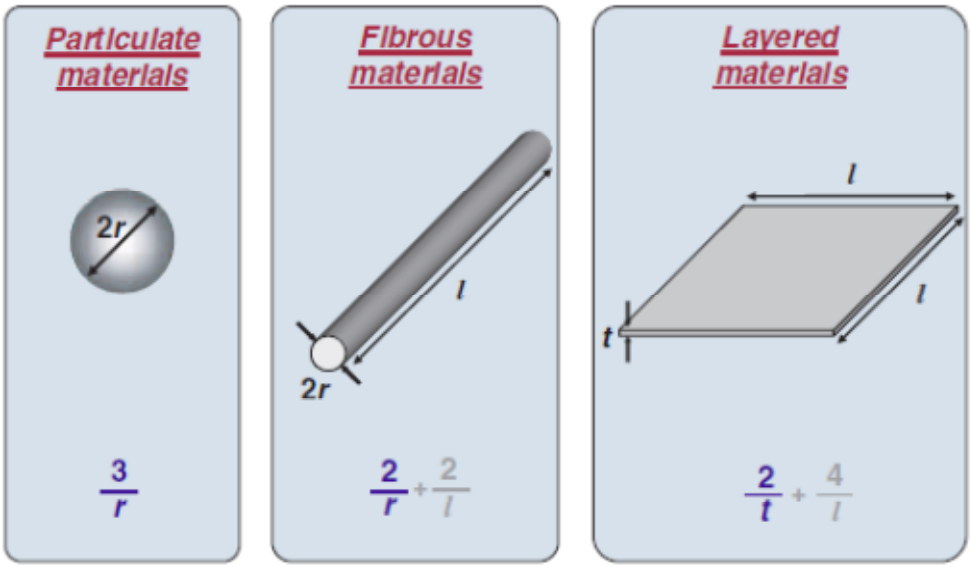

Figure 1.1 Common particle reinforcements/geometries and their respective surface area-to-volume ratios[5].

1.2. Layered Nano-Inclusion and Polymer Matrix

According to interaction between the nano layer and polymer matrix, three types of nanocomposites can be defined. We use layered silicate and polymer composite as example[6].

If no polymers get involved into the interspace between silicate layers, as shown in Figure 1.2(a), the layers exist as a separated phase in the matrix. This is so-called phase separated nanocomposite. The layered phase can be identified by X-Ray diffraction, Figure 1.3(a)[7]. When the polymer chain is intercalated between the silicate layers, it becomes intercalated nanocomposite. Since the interspaces between the layers are increased, the peak of layer phase shifts towards the lower angle values, Figure 1.3(b). If the nano layers are dispersed well enough with spacing larger than 8nm, the layer phase peak can no longer be detected in XRD pattern, as shown in Figure 1.3(c).

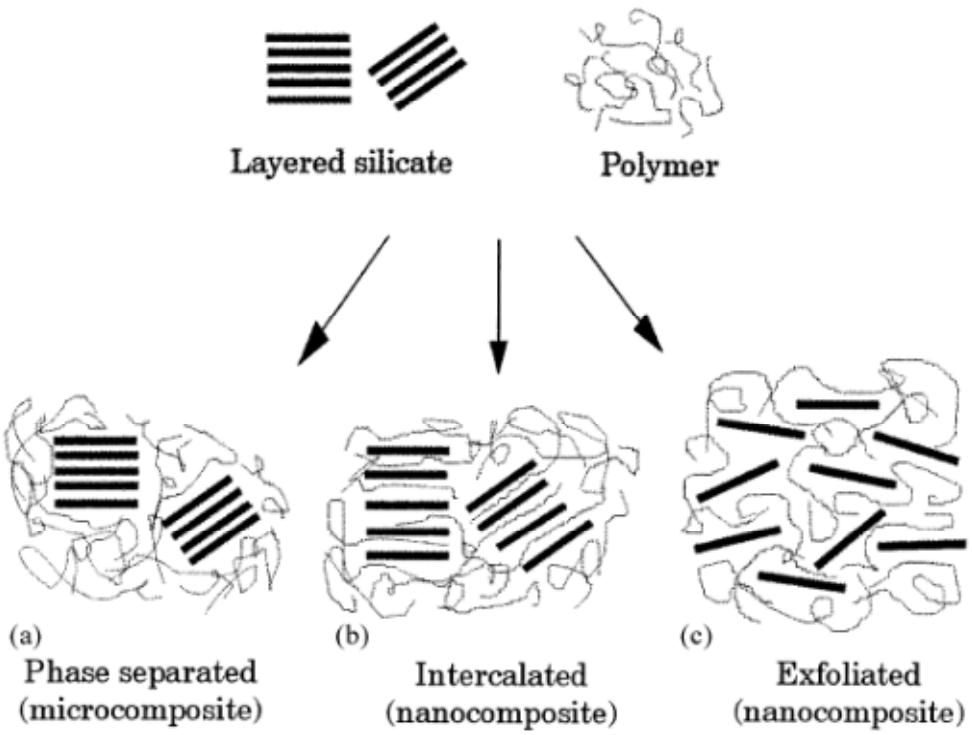

Figure 1.2 Different types of composite arising from the interaction of layered silicates and polymers[6]

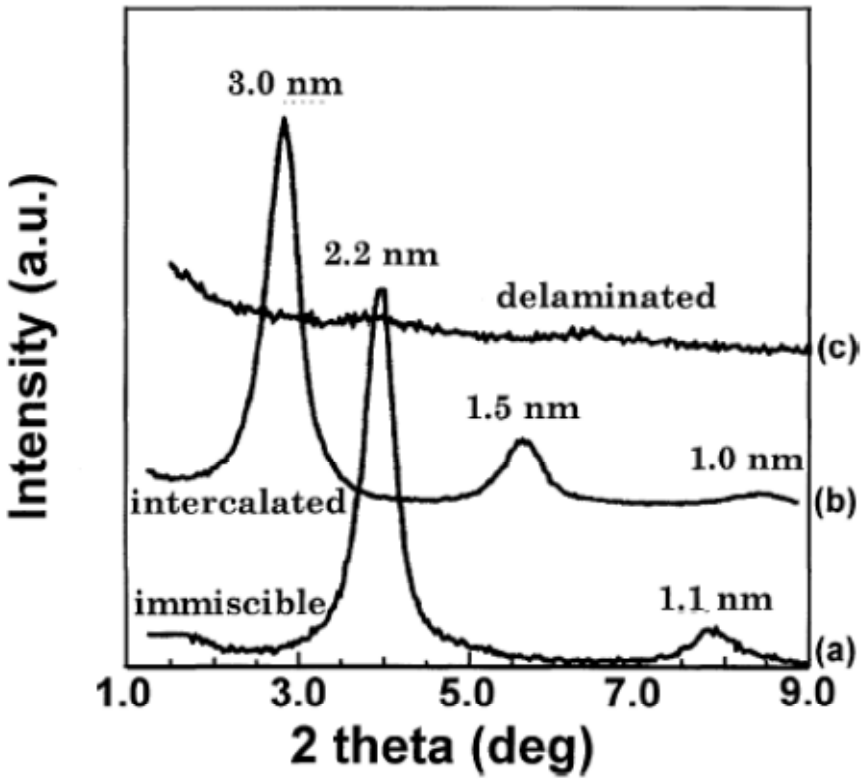

Figure 1.3 XRD patterns of: (a) phase separated microcomposite; (b)intercalated nanocomposite (c) exfoliated nanocomposite[7]

1.3. Structure of Single Wall Carbon Nanotube

Single wall carbon nanotube is a single layer of a graphite crystal rolled up into a seamless cylinder. The cylinder wall is 1 atom thick and the tube has 10-40 numbers of carbon atoms along the circumference and a micron scale length along the cylinder axis[8] (Figure 1.4).

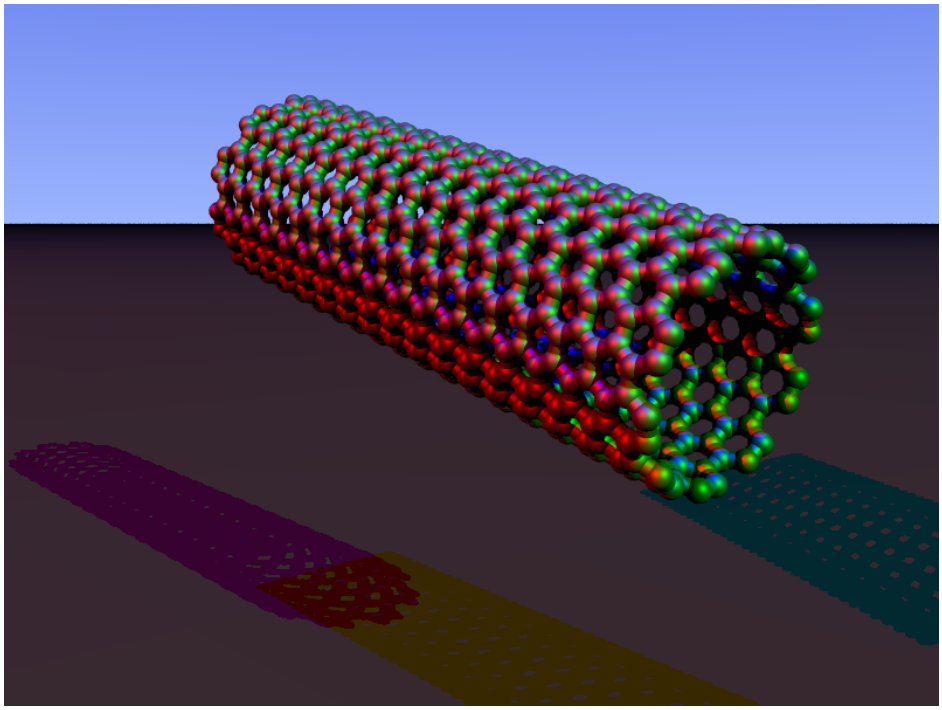

Figure 1.4 Single wall carbon nanotube

Each SWNT is specified by the chiral vectorC_h, which is often described by the pair of indices (n, m) that denote the number of unit vector $na_1$and ma_2 in the hexagonal honeycomb lattice.

$$C_h = na_1 + ma_2 = (n, m) \tag{1.1}$$

The physical meaning of chiral vector is the description of how graphite sheet is rolled up. The chiral angle θ is the angle between the unite vector a_1 and chiral vectorC_h, as showed in Figure 1.5. Three types of single wall carbon nanotube can be defined according to the chiral angle. When θ =0°, it is called zigzag nanotube; when θ =30°, it's called armchair nanotube; when $0° < \theta < 30°$, it's called chiral nanotube. The translation vector T is perpendicular to the chiral vectorC_h, meaning the axial direction of the nanotube cylinder and therefore the length of vector $|C_h|$ can be understood as circumference of bottom plane.

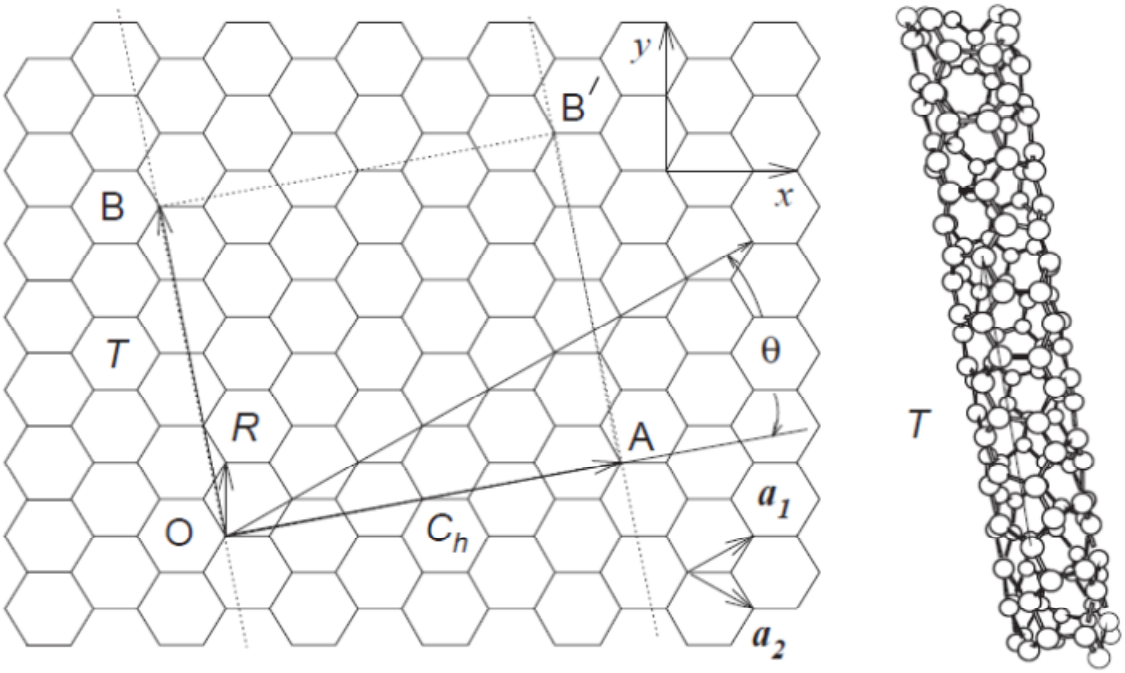

Figure 1.5 Chiral vector of single wall carbon nanotube.[9]

1.4. Electronic Properties of Nanotubes

In the field of material science, microstructure determines the physical properties of material. As for carbon nanotube, the electronic property mainly depends on two structure factors: the chirality and the diameter. As we mentioned before, the chirality of carbon nanotube can be described by a pair of indices(n, m). When $n = m$(armchair), the nanotubes show metallic properties; When $n - m = 3p$, where p is an integer, the nanotubes are expected to show metallic property; When $n - m \neq 3p$, the nanotubes are expected to semi-conducting materials[10]. Figure 1.6 shows the conducting properties with respect to chiralities on a 2-dimensional graphite sheet.

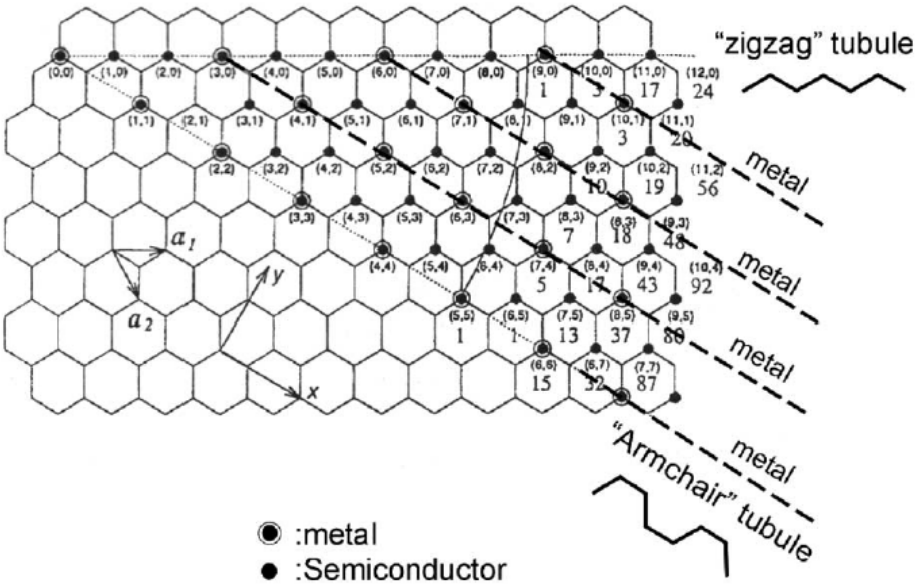

Figure 1.6 The 2D graphite sheet with given chirality[10].

When it comes to diameter, the band gap theory needs to be considered. As showed in Figure 1.7, the higher band gap energy between the conduction band and the valence band, the lower conductivities of the material.

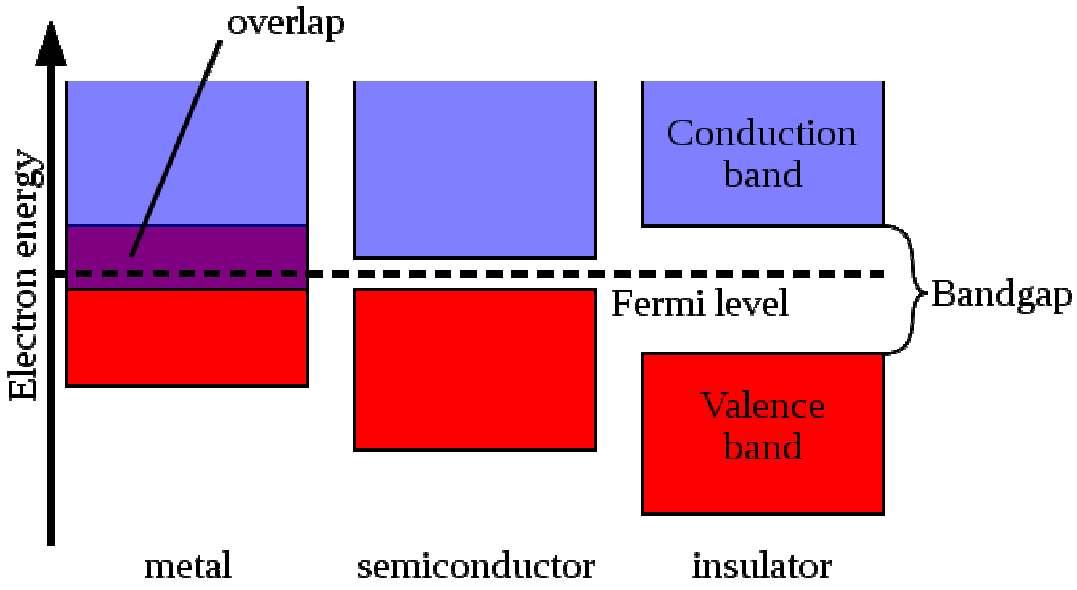

Figure 1.7 The electronic band structure of metals, semiconductors, and insulators

The band gap can be described as

(1.2)

where is the C-C tight-binding overlap energy; is the nearest neighbor C-C distance in graphite sheet; is the diameter of the nanotube. From this equation we can see the band gap energy is inversely proportional to the diameter of the nanotube. Wilder, Jeroen W. G et al experimentally showed the value of as a function of nanotube diameter ranging from 0.6 to 1.1nm[11], as showed in Figure 1.8.

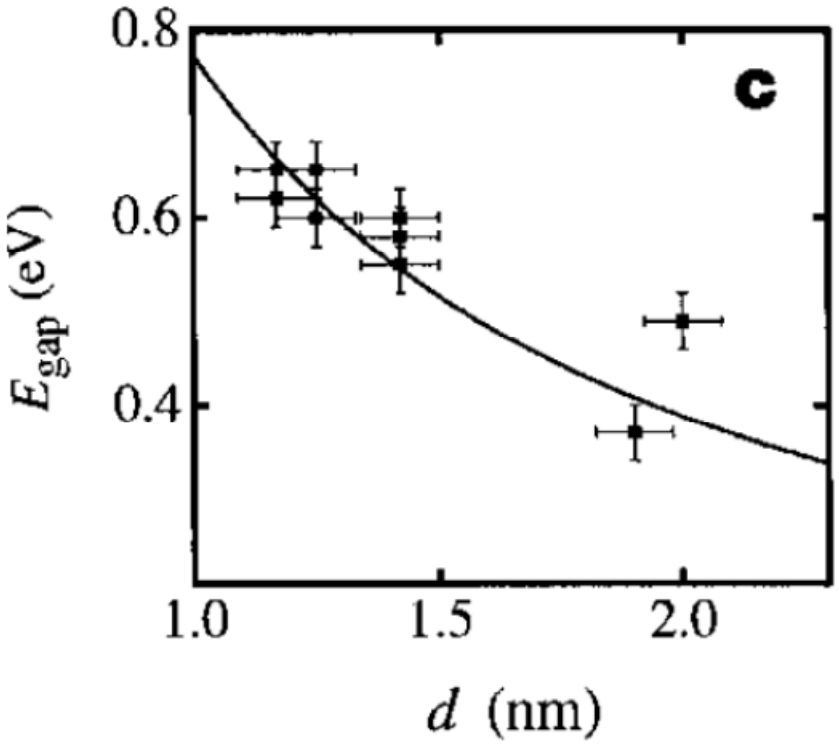

Figure 1.8 Energy gap versus diameter d for semiconducting chiral tubes[11].

1.5. Mechanical Properties of Carbon Nanotubes

Since the discovery of carbon nanotube[12-15], it was expected to display similar stiffness like graphite with in-plane modulus of 1.06TPa[16]. An empirical lattice dynamics model was used to predict the elastic properties of single and multilayered nanotubes[17], Figure 1.9. JP Lu concluded that elastic moduli are insensitive to size and helicity and the Young's and shear moduli of nanotubes are comparable to that of diamond.

(n_1,n_2)	R	B	Y	M	ν
(5,5)	0.34	0.7504	0.9680	0.4340	0.2850
(6,4)	0.34	0.7503	0.9680	0.4340	0.2850
(7,3)	0.35	0.7500	0.9680	0.4412	0.2849
(8,2)	0.36	0.7495	0.9681	0.4466	0.2847
(9,1)	0.37	0.7489	0.9681	0.4503	0.2846
(10,0)	0.39	0.7483	0.9682	0.4518	0.2844
(10,10)	0.68	0.7445	0.9685	0.4517	0.2832
(50,50)	3.39	0.7429	0.9686	0.4573	0.2827
(100,100)	6.78	0.7428	0.9686	0.4575	0.2827
(200,200)	13.56	0.7428	0.9686	0.4575	0.2827
Graphite[a]		0.0083	1.02	0.44	0.16
Graphite[b]		0.0083	0.0365	0.004	0.012
Diamond[c]		0.442	1.063	0.5758	0.1041

(n_1,n_2), index; R, radius in nm; B, Y, M, are bulk, Young's and shear moduli in units of TPa (10^{13} dyne/cm^2). ν is the Poisson ratio. Experimental values for graphite and diamond are listed for comparison.

Figure 1.9 Elastic moduli of selective single-layer nanotubes[17]

Wong et al made a direct measurement on elasticity, strength and toughness of multi wall nanotubes[18]. They used AFM to measure the bending force versus displacement along the unpinned lengths of nanotube, Figure 1.10. After the AFM tip made contact with nanobeam, the measured lateral force increased linearly as the nanobeam was elastically displaced from its equilibrium position.

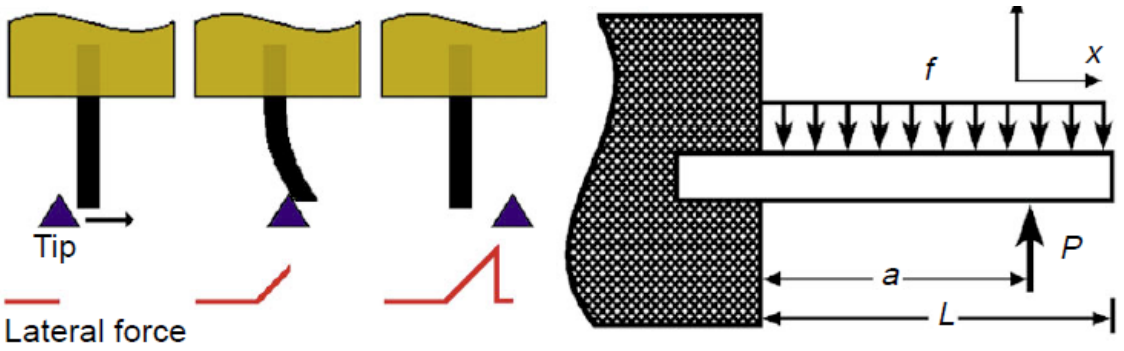

Figure 1.10 AFM tip scanning perpendicular to the axis of the nanobeam[18]

A typical F − d data was acquired to determine the E of a nanotube. According to the F − d curve, force constant as a function of position was obtained, Figure 1.11, where force constant $k(x) = \frac{dP}{dy}$ .They got the average E value of 1.28 ± 0.59TPa with no dependence on tube diameter, similar to the in-plane modulus of graphite 1.06TPa. The average bending strength for MWNTs was determined to be 14.2 ± 8.0GPa.

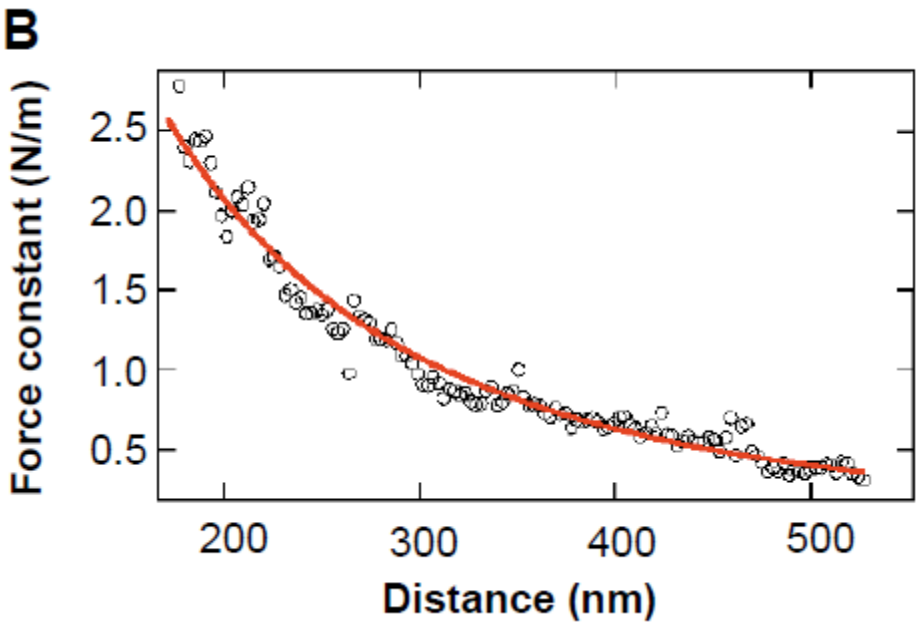

Figure 1.11 Dependence of force constant on position x along the axis of nanotube[18]

1.6. Application of Atomic Force Microscope

Atomic force microscope was invented by Binning, Quate and Gerber in 1986[19]. It is a powerful tool to detect the material surface topography in nano scale. Figure 1.12 is the central component of the AFM system used in this research. The major parts from top to bottom are laser head, probe holder and probe, scanner, motor control and base. The height value as a function of position (x, y) is collected when a sharp probe is scanned across the material surface.

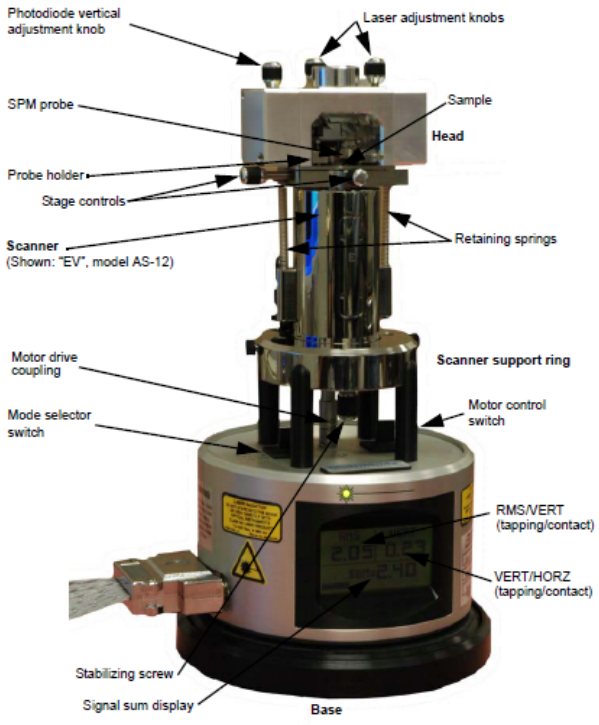

Figure 1.12 The central component of the AFM system

The laser path is showed in Figure 1.13. A laser is generated from the laser head 1 and then reflected by the mirror 2, hit the back of cantilever, reflected by the tilt mirror 4 and finally detected by the photodetector 5.

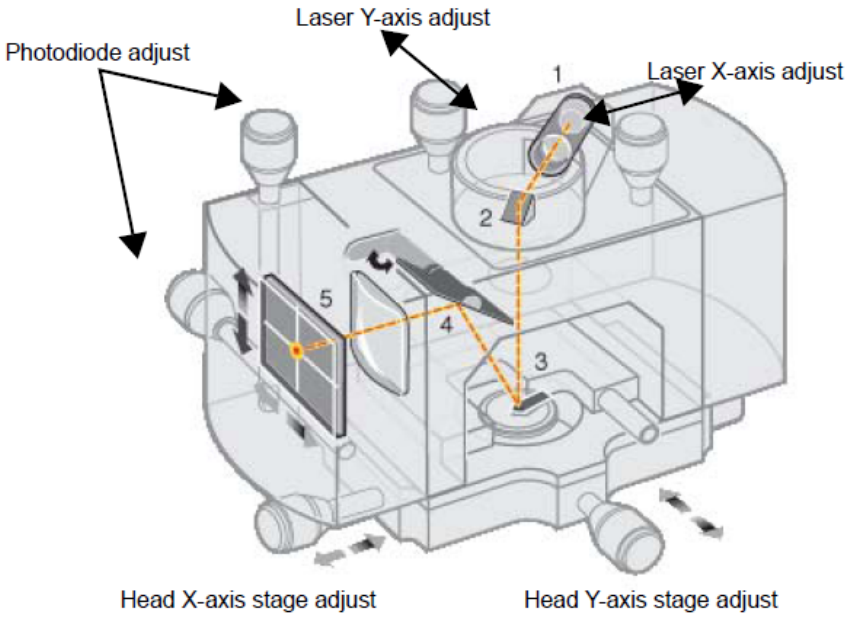

Figure 1.13 Multimode AFM laser head

There 2 typed of scanning method for this AMF: contact mode and tapping mode. Contact mode AFM operates by scanning a tip attached to the end of a cantilever across the sample surface while monitoring the change in cantilever deflection with a split photodiode detector. A feedback loop, Figure 1.14(a), maintains a constant deflection between the cantilever and the sample by vertically moving the scanner at each (x, y) data point to maintain a "setpoint" deflection. By maintaining a constant cantilever deflection, the force between the tip and the sample remains constant.

Tapping Mode AFM operates by scanning a tip attached to the end of an oscillating cantilever across the sample surface. The cantilever is oscillated at or slightly below its resonance frequency with amplitude ranging typically from 20nm to 100nm. The tip lightly "taps" on the sample surface during scanning, contacting the surface at the bottom of its swing. The feedback loop, Figure 1.14(b), maintains a constant oscillation amplitude by maintaining a constant RMS of the oscillation signal acquired by the split photodiode detector.

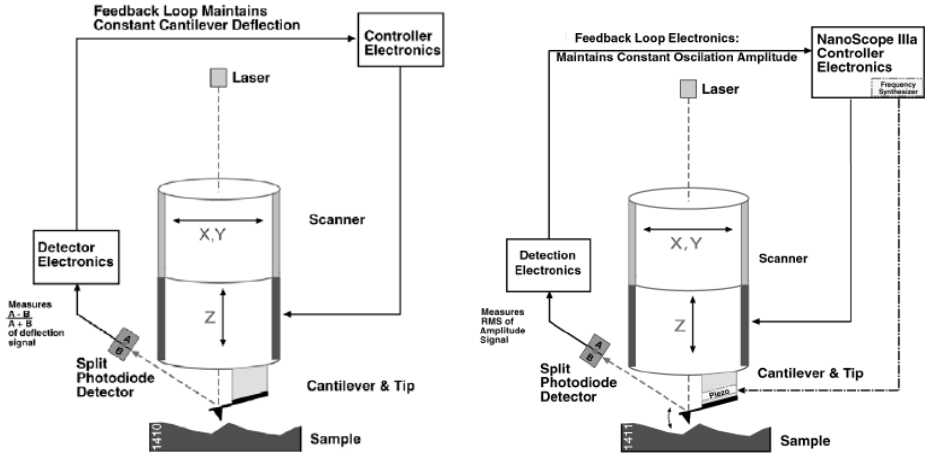

Figure 1.14 (a) contact mode (b) tapping mode

Atomic Force microscope can be used to detect interfacial adhesion between the nanotube and surrounding polymer[20]. One end of nanotube is attached on the tip of AFM and the other end is embedded in polymer matrix. During the polling out process, the interfacial shear strength can be measured by detecting the cantilever bending force, as showed in Figure 1.15. Increasing the nanotube embedded length causes the nanotube to break instead of pullout from the polymer. As a result, the forces required to pull out nanotubes embedded at various lengths can be record, Figure 1.16.

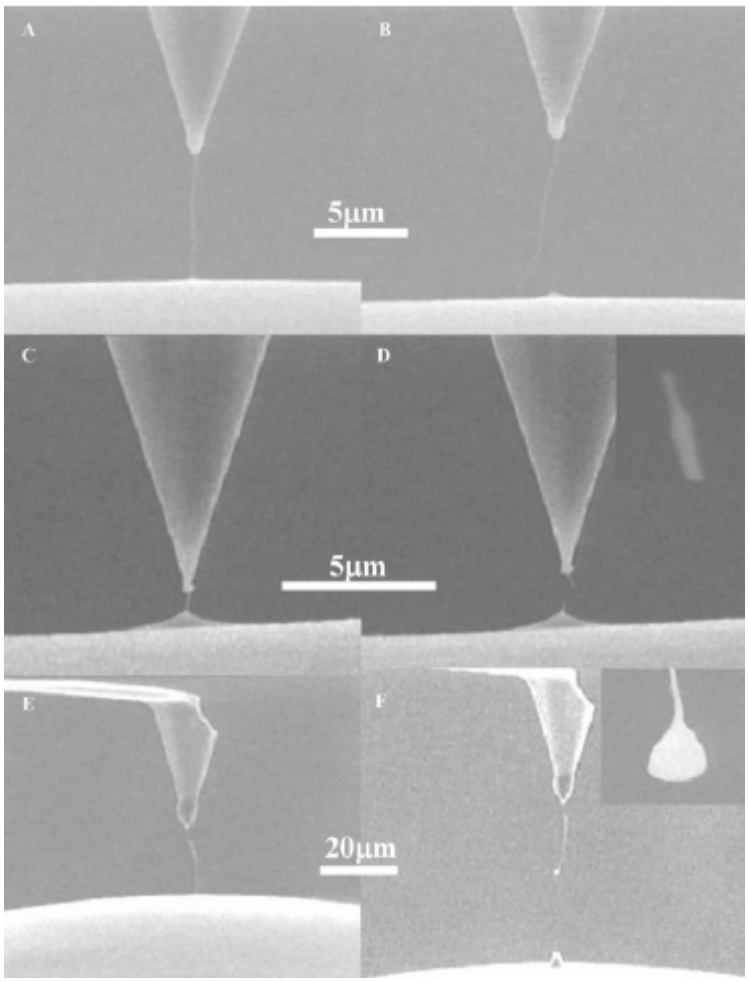

Figure 1.15 Pullout of nanotubes from a polymer using AFM tip[20]

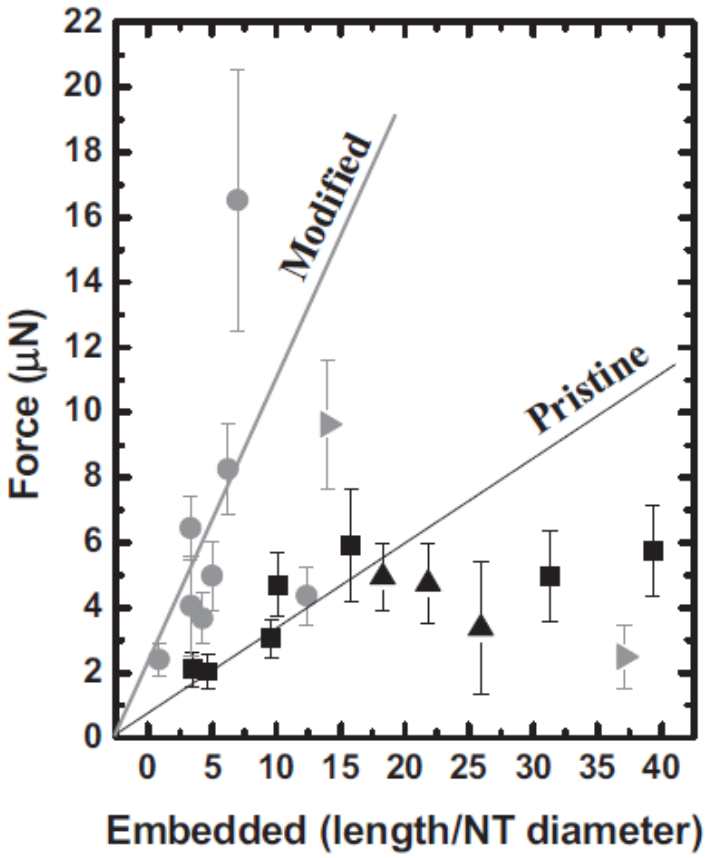

Figure 1.16 The force required to pull out nanotubes embedded at various lengths[20]

Atomic force microscopy-based nanoindentation can be used to map the nano scale mechanical properties like elasticity and stiffness. Dusan Losic et al performed nanoindentation on cribellum surface using Veeco Dimension 3000 AFM with diamond tip[21], Figure 1.17. Typical force penetration curve with loading and unloading can also be obtained.

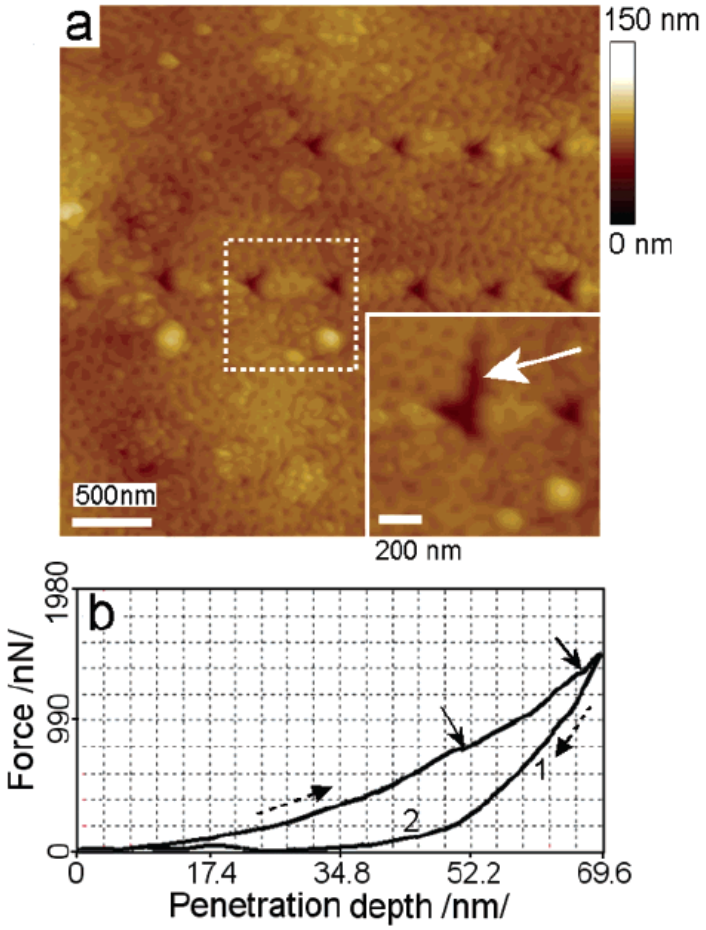

Figure 1.17 AFM image of nanoindentations performed on the cribellum surface and force penetration curve[21].

1.7. Raman Spectroscopy

When a strain is applied to a nano composite material, the interatomic distances of C-C change, and thus the vibrational frequencies of some of the normal modes change causing a Raman peak shift.

The Raman spectrum for nanotubes has been well documented by Rao, A. M et al[22]. They did lattice dynamics calculations based on C-C force constant. The intensities and frequencies turned out to agree well with Raman scattering measurement, Figure 1.18.

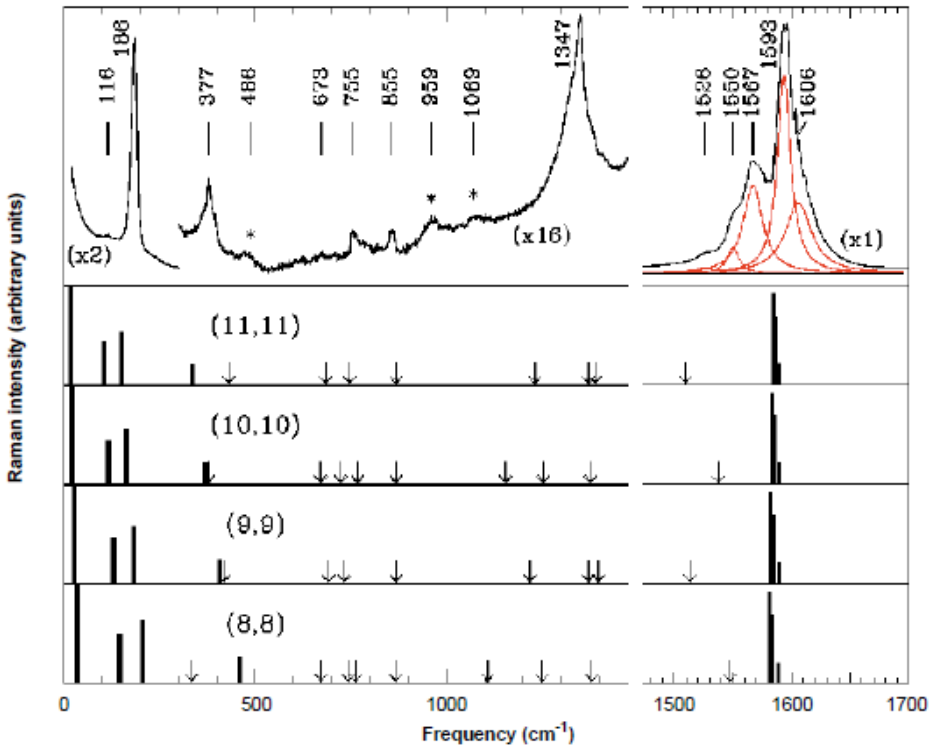

Figure 1.18 Raman spectrum (top) of SWNT samples and the calculated Raman spectra for armchair (n, n) nanotubes with n=8-9[22]

C.A. Cooper et al observed that G′ Raman band shifts to a higher wavenumber when the SWCTs is under hydrostatic pressure, Figure 1.19; while G′ Raman band shifts to a lower wavenumber when tensile stress is applied, Figure 1.20[23]. They demonstrated that the effective modulus of SWNTs dispersed in a composite could be over 1 TPa.

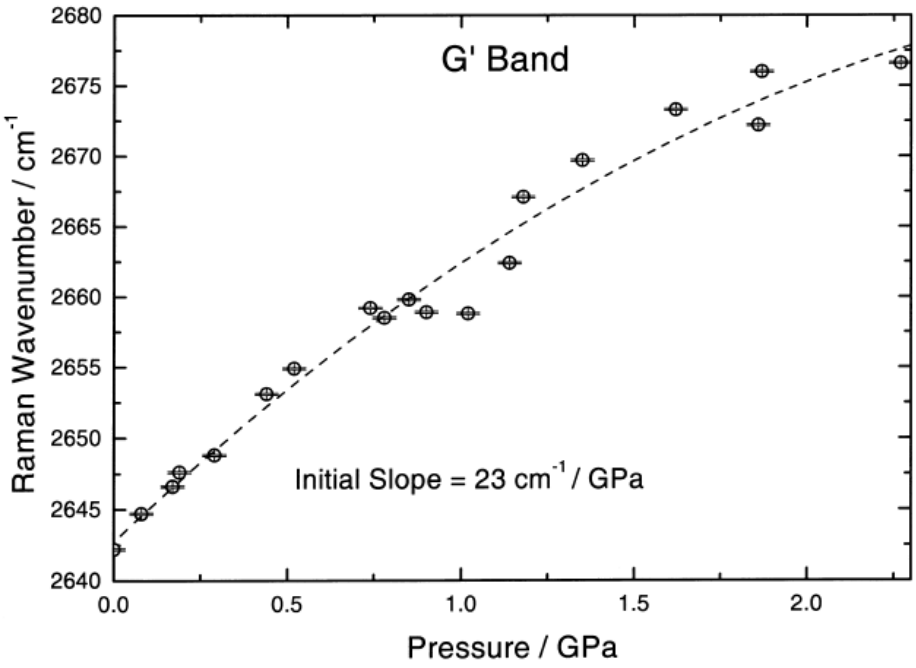

Figure 1.19 Pressure dependence of the pulsed laser SWNT G′ Raman peak[23]

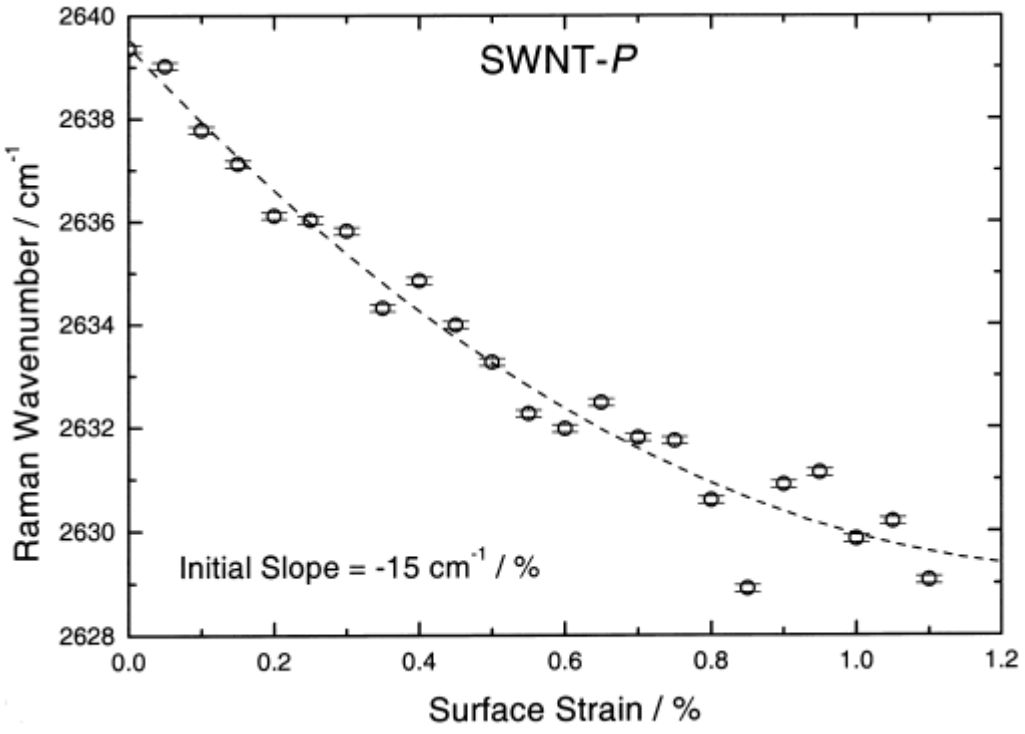

Figure 1.20 Variation of the G′ Raman peak position with tensile strain for pulsed laser SWNT dispersed in epoxy resin[23].

Schadler, L. St al found the second order band of multiwall carbon nanotube shifts slightly positive in tension and negatively in compression, Figure 1.21[24]. The large shift in compression compared to tension indicates that the MWCTs carry more strain in compression than in tension.

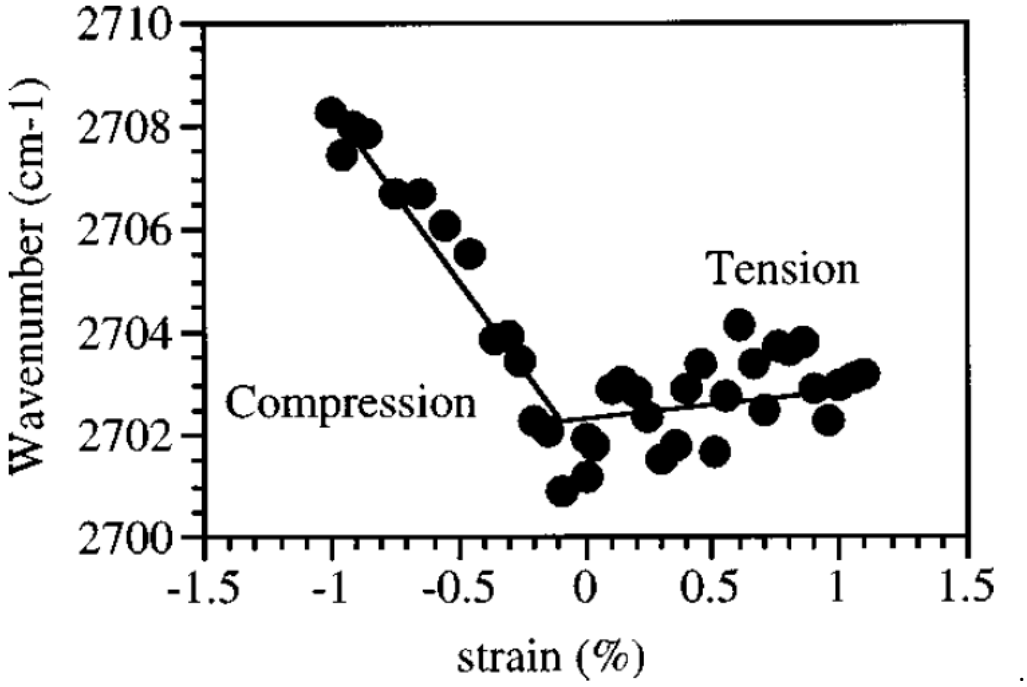

Figure 1.21 The second order Raman peaks shift of MWCTs under loading[24].

1.8. Dispersion of Nanotube in Polymer

It is quite a challenge to achieve a high degree dispersion of SWNTs in polymer matrix due to their tendency to aggregate in bundles and agglomeration[25]. Wise, K.E et al dispersed SWNTs in a nitrile functionalized polyimide matrix[26]. They observed G band upshifts in Raman spectra which indicate a noncovalenet interaction between nanotube and polymer, Figure 1.22.

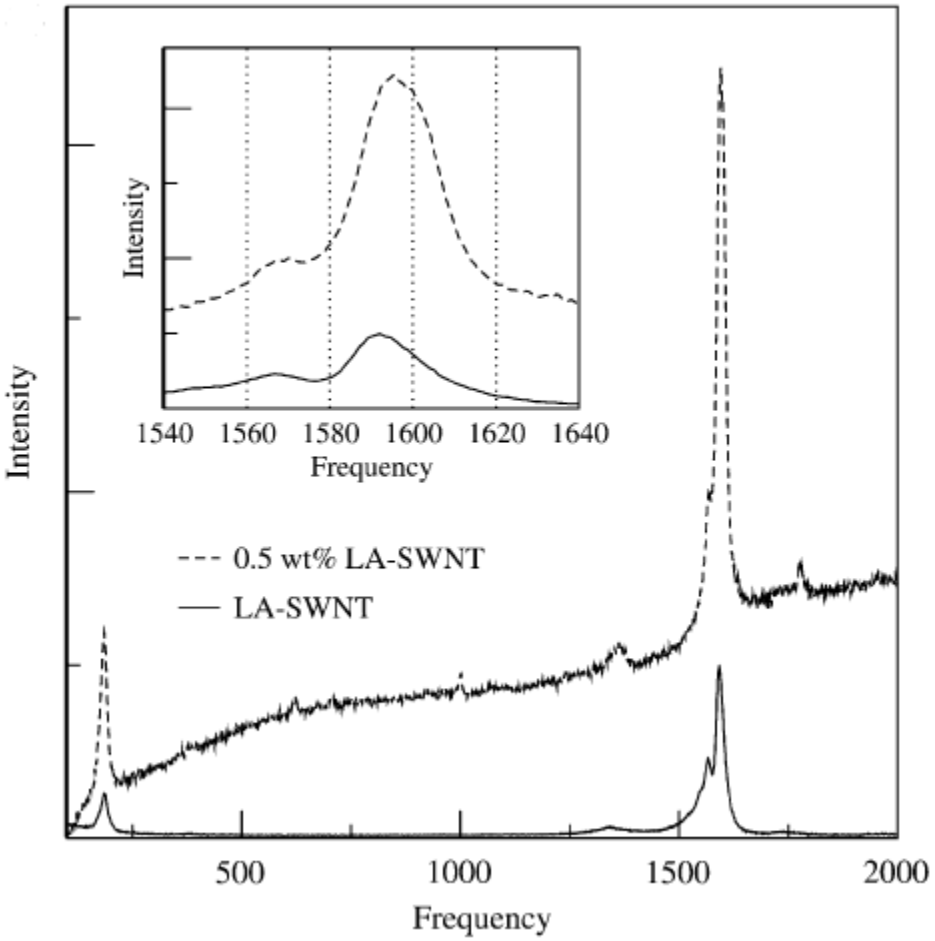

Figure 1.22 Raman spectra of SWNTs in isolation and in 0.5 wt% composite[26]

Badaire, Stéphane et al measured the dimentions of CNTs in dispersed state via Depolarized dynamic light scattering[27]. They studied the effect of sonication time and power on the dispersion of nanotube in surfactant solutions, as showed in Table 1.1. The diameter of the SWNT bundles decrease with the incraeasing of sonication time at a constant pressure.

	sonication power			
	20 W		40 W	
sonication time (min)	length (nm)	diameter (nm)	length (nm)	diameter (nm)
15			1156 ± 192	37.9 ± 5.4
30	2286 ± 948	40.6 ± 28.6	926 ± 155	30.7 ± 6.5
45	1494 ± 163	29.6 ± 17.6		
60	1368 ± 30	21.4 ± 10.7	863 ± 38	9.7 ± 3.0
90	1208 ± 121	13.9 ± 3.0	895 ± 34	3.8 ± 1.1
120	1146 ± 187	12.1 ± 2.5	822 ± 83	2.9 ± 0.7

Table 1.1 Influence of Sonication Time and Power on the Dimensions of CNT Bundles[27]

Barry J. Bauer et al used small angle neutron scattering to determine the average dispersion of large collection of SWNTs. They applied power law to measure the degree of aggregation[28]. For example, a slope of between -2 and -3 for a chain molecule such as polymer or a SWNT strongly suggests aggregation, Figure 1.23 Power law scattering from fractal objects[28].

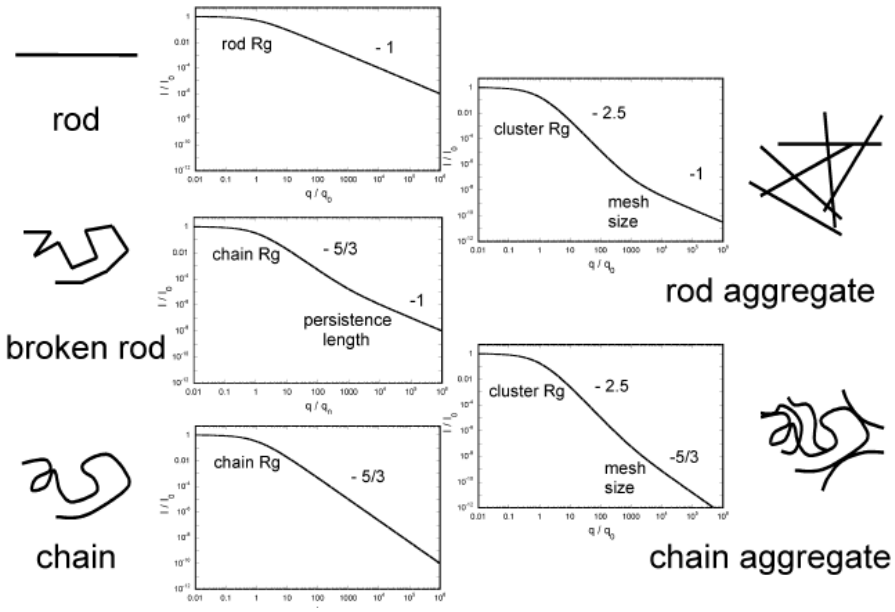

Figure 1.23 Power law scattering from fractal objects[28]

Dale W. Schaefer et al used small angle X-ray scattering to determine the morphology of carbon nanotube suspension on a scale of 1nm-50μm[29]. They found the morphology is dominated by a network structure of aggregated tubes instead of rod like tubes.

1.9. Fabrication of Nanotube/Polymer Composite

Three mainly fabrication methods have been used to synthesize nanotube/polymer composite: solution blending, melt blending and in situ polymerization. All methods are to improve the nanotube dispersion in polymer matrix because a homogeneous distribution of nanotube has a great influence on composite performance[30].

1.9.1 Solution Blending

The solution blending is the most popular method to fabricate the nano-composite[31]. Three major steps are involved in solution blending: disperse nanotubes in a solvent; mix the solvent with polymer which can be solid or emulsion; drying the solution into a solid composite. Before the drying process, usually a high power sonication is applied to make a temperately suspension with nanotube[32]. It is common for researchers to use different kinds of surfactants to modify the surface of the nanotube and make the tubes stable in the solution[33].

M. F. Islam et al used NaDDBS($C_{12}H_{25}C_6H_4SO_3Na$) as surfactant to exfoliate nanotube bundles into single tubes with a fraction of 63±5% in water[32]. They used tapping mode AFM to measure the fraction of single tubes. The tube diameters were derived from height measurements. As showed in Figure 1.24, the shaded regions define single tubes, at weight concentration of 0.1mg.ml there are 74±4% single tubes.

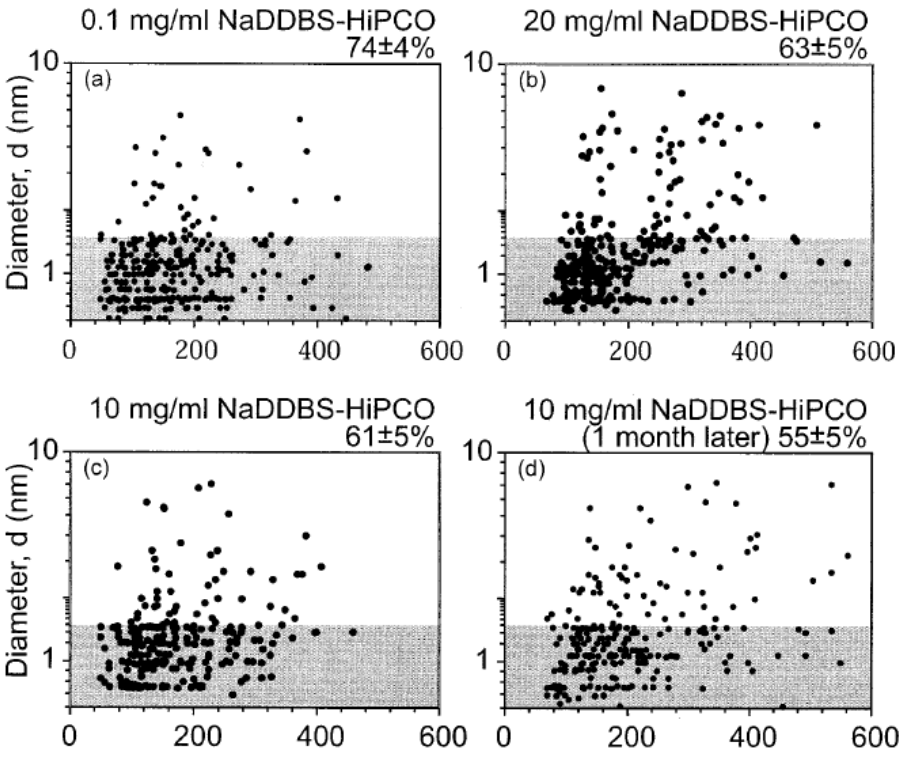

Figure 1.24 Length and diameter distribution of HiPCO tubes dispersed by the bath sonicator[32]

Xiaoyi Gong et al used Polyoxyethylene 8 lauryl as nonionic surfactant to dissolve nanotube in acetone with mechanical stirring[34]. The addition of 1 wt % carbon nanotubes in the composite increases the glass transition temperature from 63 °C to 88 °C. As shown in Figure 1.25(b), the agglomerated carbon nanotubes without surfactant can be easily separated from the matrix without breaking the nanotubes.

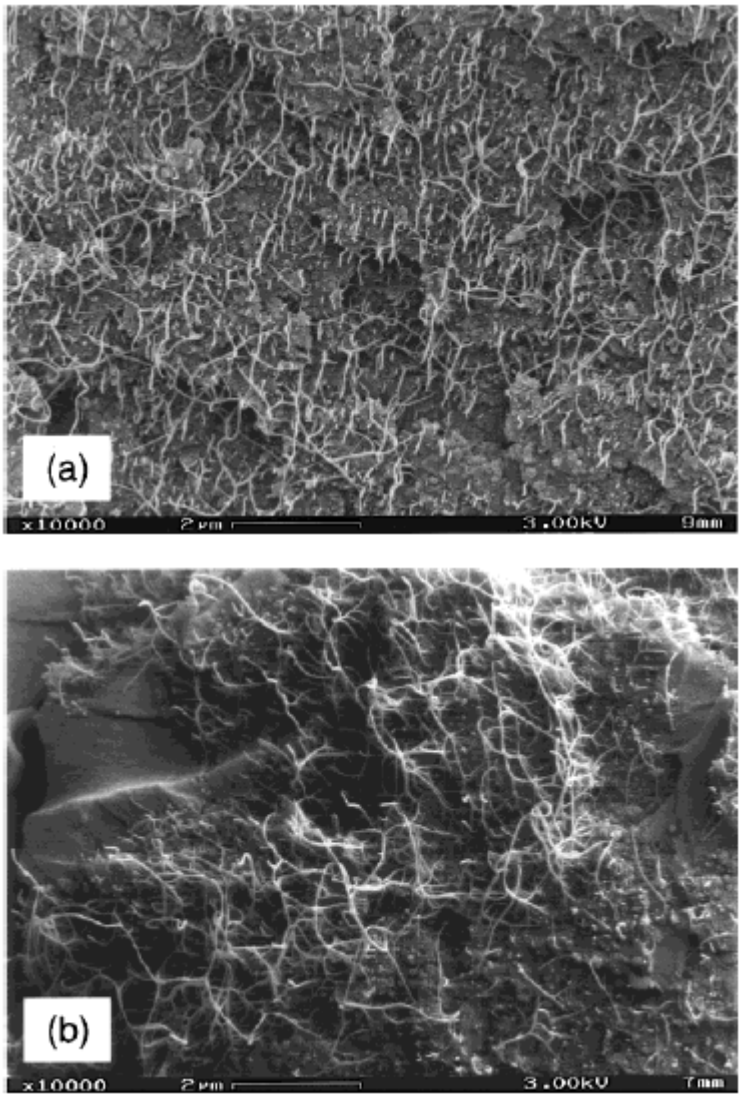

Figure 1.25 SEM photographs of carbon nanotubes on fracture surfaces of the composite samples: (a) with surfactant and (b) without surfactant[34]

1.9.2 Melt Blending

Melt processing method is suitable to deal with thermoplastic polymers which can be easily softened when heated. When the heating temperature is above the polymer glass transitionT_g, semi-crystalline polymers become soft enough to form a viscous liquid[35]. Then the nanoparticles can be mixed into the polymer by applying shearing force in the

form of compression molding, injection molding or extrusion[36]. Several groups have report their composite samples processed by melt blending in Polystyrene[37], PMMA[38], polypropylene[39], PBO[40].

R. Haggenmueller et al combined the solvent casting and melt mixing to disperse SWNT in PMMA[38]. They broke solvent casting film into pieces and hot pressed the pieces at 180℃ and 3000lb for 3 minutes. The melt mixing procedure was repeated up to 25 times. The dispersion result detected by optical microscope can be seen in Figure 1.26.

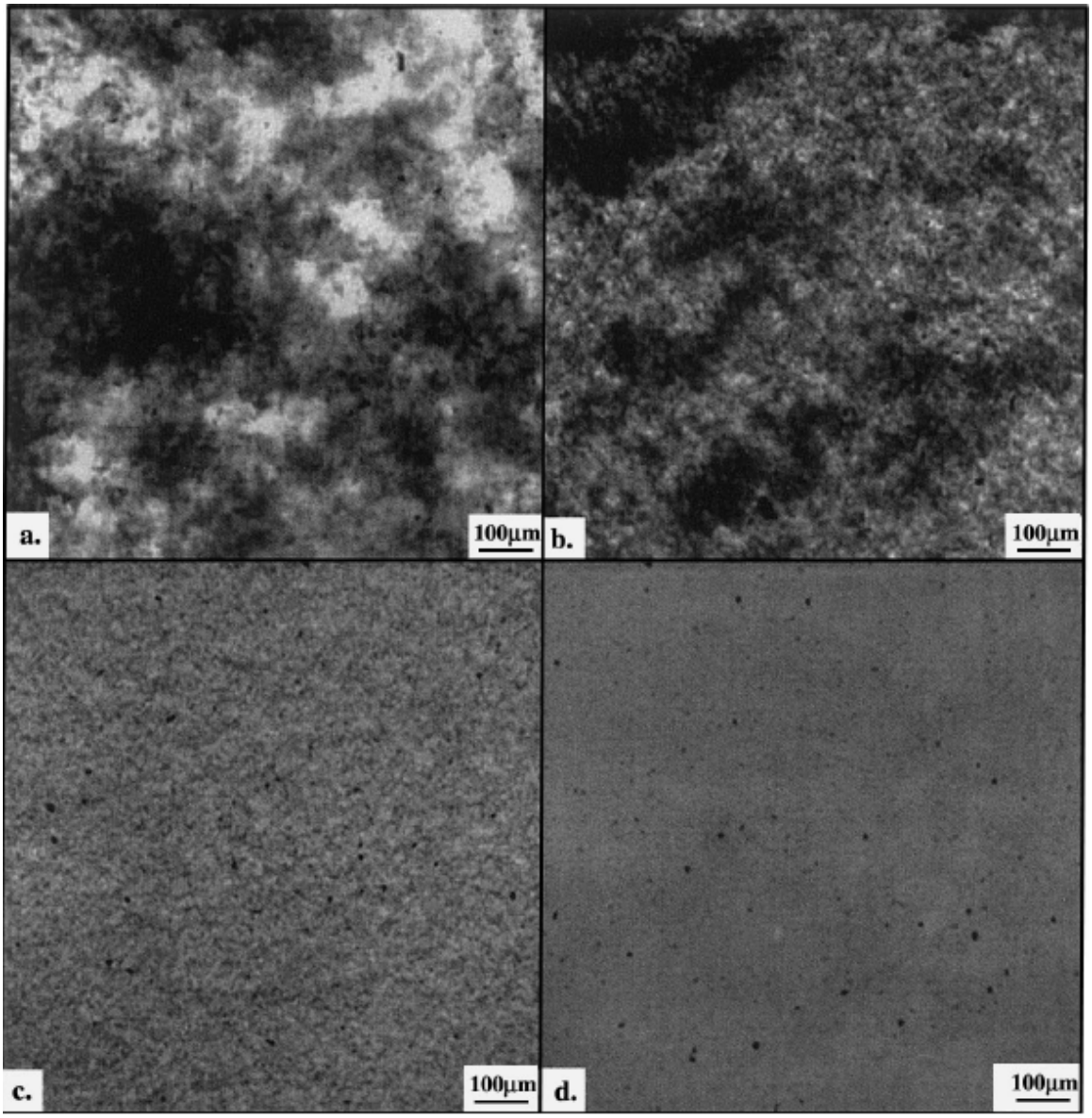

Figure 1.26 Optical micrographs of a SWNT±PMMA nanocomposite (a)solvent casting sample. (b) hot pressing (180°C, 3000 lb, 3 min) for 1 cycle; (c) 5 cycles; (d) 20 cycles[38].

Emilie J. Siochi et al used melt extrusion and fiber drawing process to align SWNT in the fiber direction and achieved higher tensile moduli and yield stress[41]. Figure 1.27 show the single screw extruder developed at NASA Langley Research Center. A filter (component 4 in the figure) was used in the nozzle to help breaking up agglomerations.

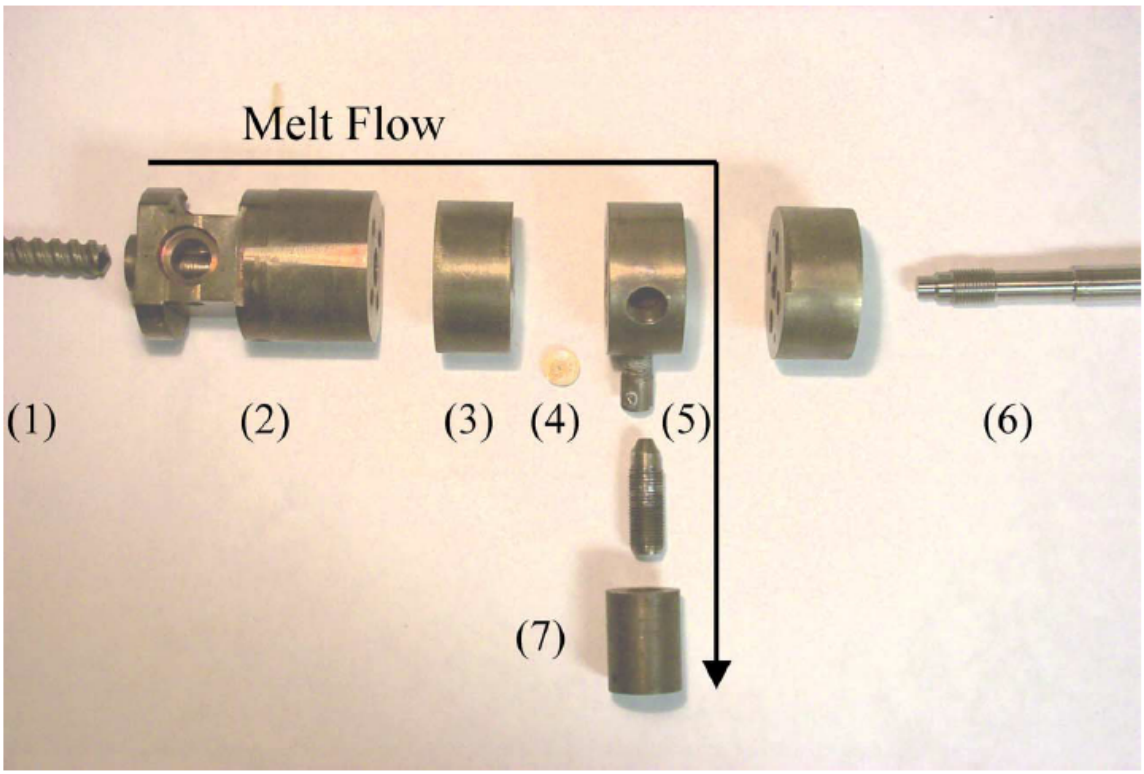

Figure 1.27 Components of extruder used for melt processing of SWCNT/Ultem nanocomposites[41].

Arup R. Bhattacharyya et al[42] mixed polypropylene with 1wt% SWNT in a Haake rheomix mixer at 240℃ at 50rpm for 30min and passed the PP/SWNT composite through a 300, 250, 120 and 80 mesh filters at 240℃. X-ray diffraction was obtained to confirm the existence of α-crystal formation of polypropylene, as showed in Figure 1.28.

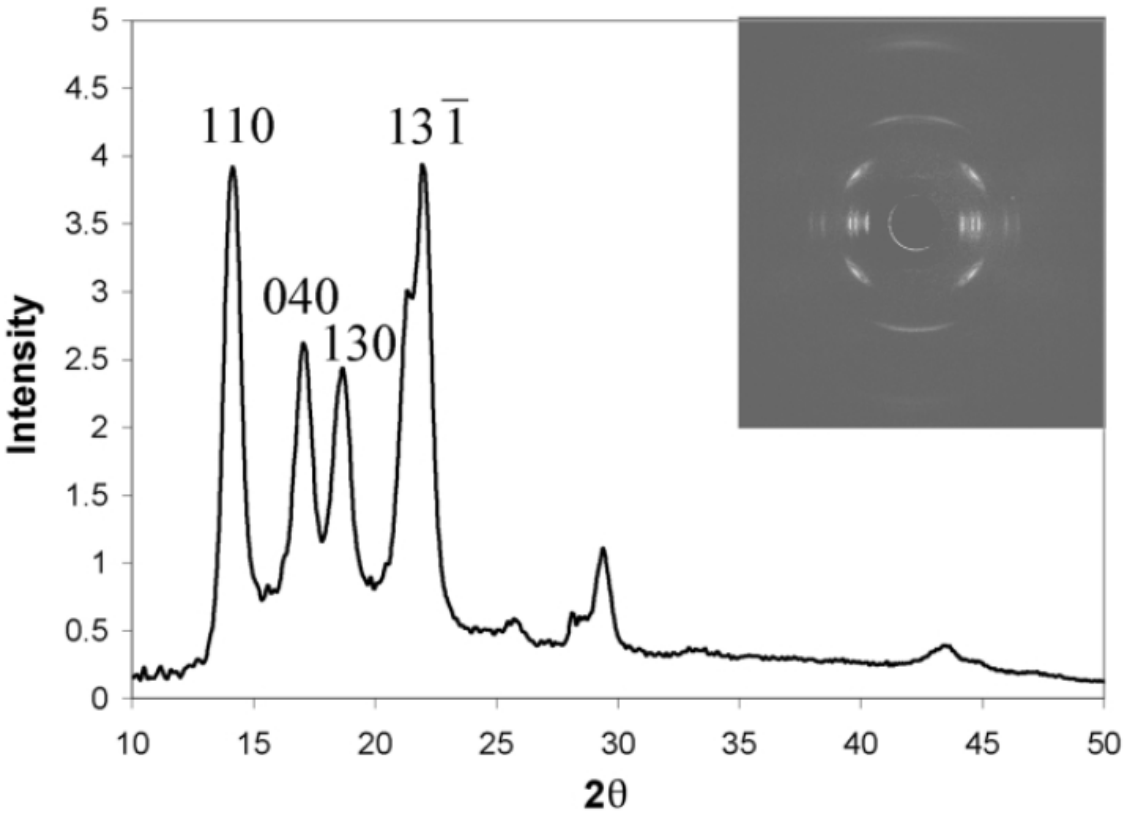

Figure 1.28 Integrated wide angle X-ray diffraction intensity of PP/SWNT composite fiber[42].

1.9.3 In Situ Polymerization

In situ polymerization applies condensation reactions to connect functionalized nanotubes to the polymer matrix by covalent bonding[43]. The Chemical modification and functionalization of nanotube can enhance the interaction between pristine nanotubes and surrounding matrix. If the interfacial bonding is not strong enough, the load transfer from polymer to nanotube could be limited[44]. Also the sliding of the SWNTs within the blending of bundles limits the mechanical enhancement due to the disorder of the alignment [45, 46].

Jiang Zhu et al used optimized acid treatment and subsequent fluorination to disperse functionalized SWNTs into an epoxy composite, increasing 30% in modulus and 18% in tensile strength[47]. Xiaoyi Gong et al reported the introduction of surfactant as processing aid increased the glass transition temperature from 63℃ to 88℃. The elastic modulus was also increased by more than 30%[34]. Mohammad Moniruzzaman et al applied high shear mixing of the epoxy resin and SWNT and heat treating the mixture prior to introducing the hardener to prepare SWNT/epoxy nanocomposites. The whole method is showed in Figure 1.29. They researched an improvement of 17% in flexural modulus and 10% in flexural strength at 0.05wt% of nanotubes[48].

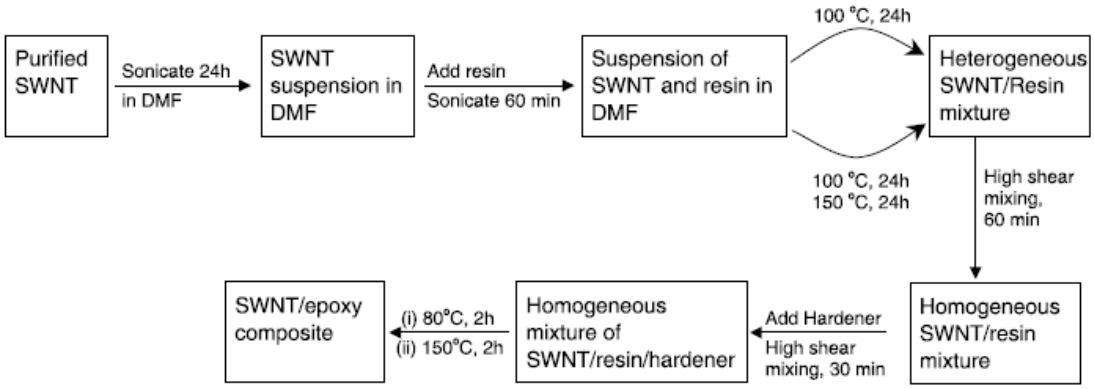

Figure 1.29 Schematic of the preparation of SWNT/epoxy nanocomposites[48]

1.10. Application of Carbon Nanotube Composites

It has been reported that the tensile modulus and strength of the nanotubes range about 270Gpa to 1TPa and 11-200GPa [49, 50]. The carbon nanotubes exhibit excellent tensile strength compared with graphite, Kevlar fibres and stainless steel, as showed in Figure 1.30[10]. Since the carbon-carbon covalent bonds are one of the strongest in nature, the tube structure based on such bonds would produce an extraordinary strong material along the axis of tube. The nanotubes are 100 times stronger than steel but only one-sixth as heavy as steel making it enable to be used as reinforcements in high strength, light weight, high performance composites.

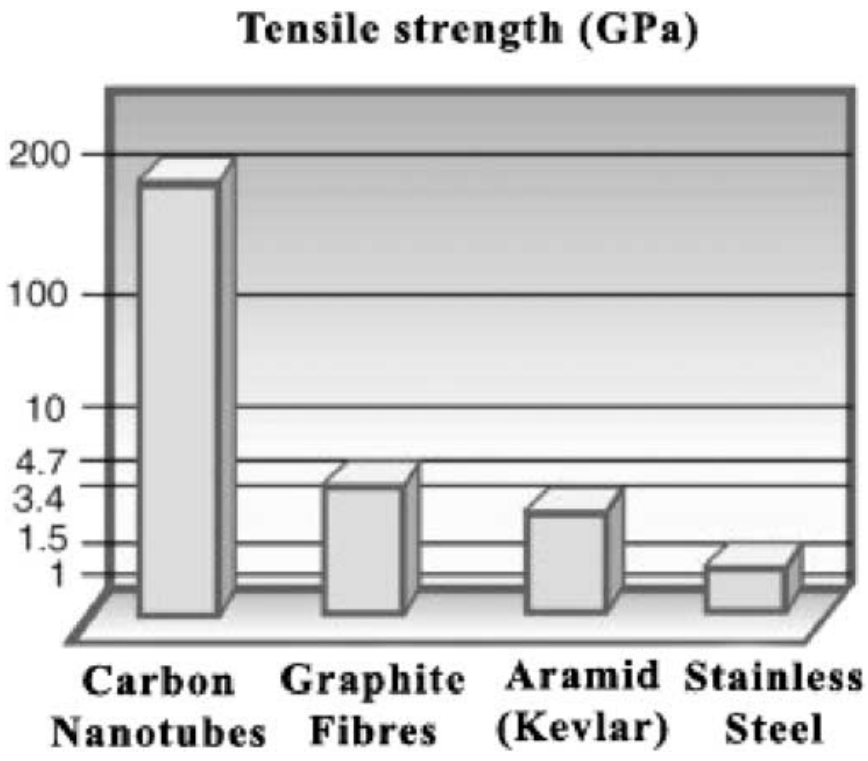

Figure 1.30 The tensile strength of different engineering materials in log scale[10]

CHAPTER 2 TITANIUM DIOXIDE AND POLYANILINE COMPOSITE

2.1 Thermoelectric Effect and Applications

The thermoelectric effect is the direct conversion of temperature differences to electric voltage and vice-versa. An applied temperature gradient can cause charge carriers in the material to diffuse from the hot side to the cold side. Conventional metal or metal alloys can generate tens of microvolts per degree temperature difference. They are used in the measurement of temperature or as sensors to operate control systems. However, the modern semiconductors with material properties and geometry specifically tailored possess Seebeck coefficients of hundreds of microvolts per degree. The term "thermoelectric effect" encompassed three separately identified effects: the Seebeck effect, Peltier effect and Thomson effect.

2.1.1 Seebeck Effect

The Seebeck effect is the conversion of temperature differences directly into electricity. The thermoelectric energy conversion can be discussed in with reference to the schematic of a thermocouple shown in Figure 2.1. A and B are two thermoelecments electronically connected. The junctions of A and B are maintained at different temperature T_1 and T_2. The voltage V developed can be derived from:

where and are the thermopowers of material A and B as a function of temperature. For a small temperature differences the relation is linear, the above formula can be approximated as:

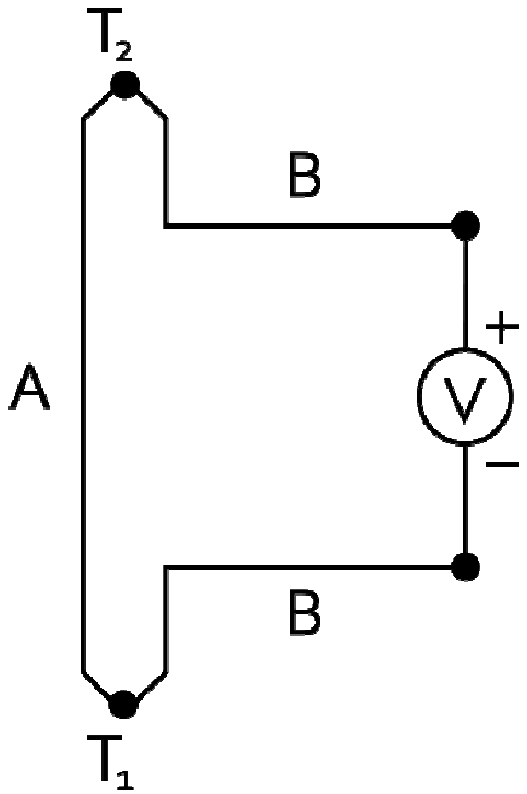

Figure 2.1 Schematic basic thermocouple. A and B are two different materials.

2.1.2 Peltier Effect

In Figure 2.1, if the reverse situation is considered with an external V voltage applied and a current I flows around the circuit then a rate of heating q occurs at one junction between A and B and a rate of cooling $-q$ occurs at the other. The ratio of I to q defines the Peltier coefficient $\Pi = \frac{q}{I}$, representing how much hear current is carried per unit charge through a given material.

2.1.3 Thomson Effect

The Thomson effect describes the heating or cooling of a current-carrying conductor with a temperature gradient. If a current density J is passed through a homogeneous conductor, and there is a temperature difference between two points of the conductor, the material will either absorb or release heat. The rate of the generation of heat q per unit volume is:

$$q = \rho J^2 - \mu J \frac{dT}{dx}$$

where ρ is the resistivity of the conductor, μ is the Thomson coefficient. The first term is the Joule heating, the second term is the Thomson heating following J sign changing.

2.1.4 Application of Thermoelectric Devices

Thermoelectric devices are simple and have no moving parts. As shown in the Figure 2.2 left, when an external power is applied on the thermal couple, negatively charged electrons carry electrical current in the n-type leg, and positively charged holes carry the current in the p-type leg. Both the electrons and the holes carry heat away from the cold side, resulting cooling. Inversely, if a heat source is applied on one side of the device, as shown in Figure 2.2 right, a voltage can develop on the other side, converting heat energy to electrical power.

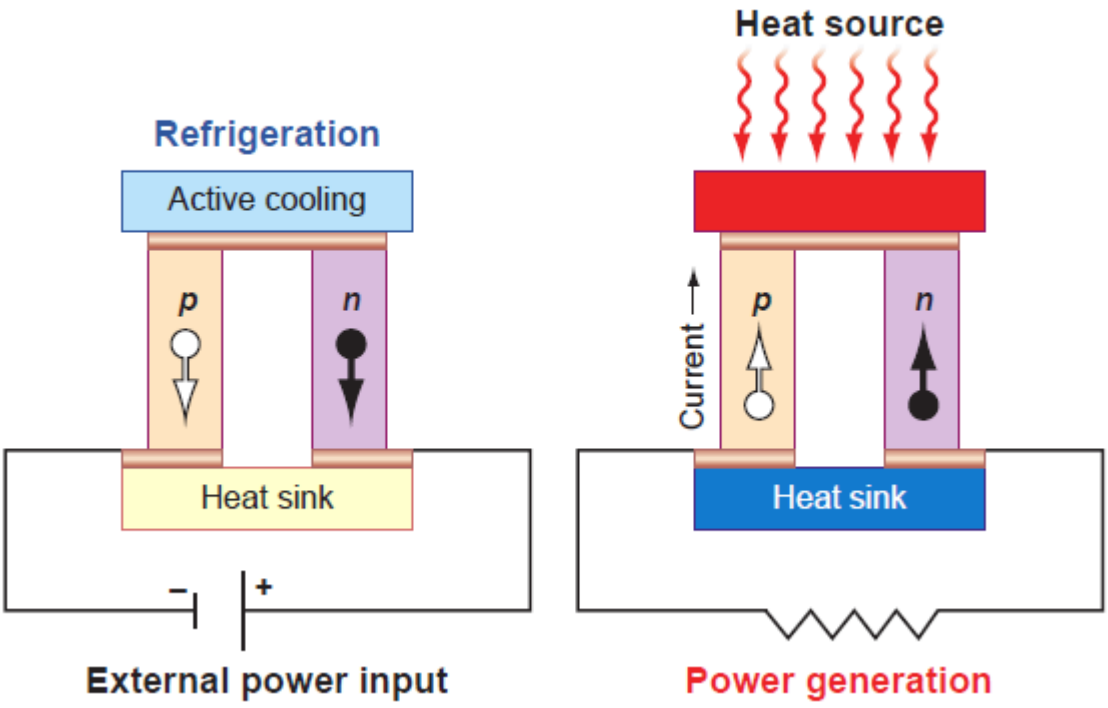

Figure 2.2 Thermoelectric refrigeration and power generation[51].

The critical issue with the thermoelectric device is the poor efficiency. The material properties of the n- and p- type semiconductor plays an important role in improving the energy conversion efficiency. The efficiency of the thermo electrical material is determined by a dimensionless parameter ZT, called figure of merit:

$$ZT = \frac{\sigma S^2}{\kappa}$$

where σ is the electrical conductivity, S is the Seebeck coefficient, and κ is the thermal conductivity. Effective thermoelectric materials have a low thermal conductivity but a high electrical conductivity.

2.2 Titanium Dioxide and Polyaniline Composite

Recently conducting polymer with heavily doped semiconductors has become popular due to the fact that insulators have poor electrical conductivity and metals have low Seebeck coeffient. Titanium dioxide stands out among the most promising transition semiconductors because of its special chemical and physical properties[52]. However, low value of ZT and other unmatched mechanical properties limit its application.

Polyaniline (PANI) is one of the most important conducting polymers because of its high environmental stability, low cost and reversible control of its conductivity[53]. Polymer/inorganic composites have received much attention due to their independent electrical, optical, and mechanical properties[54-56]. The combination of conducting polymers and semiconducting inorganic materials with the properties of semiconducting inorganic particles has brought new prospects for applications[57]. Usually, the strong interaction between eigenstate PANI rigid chains leads to low conductivity. However, H^+ can be easily poured into the PANI molecular chains, and thus increases the level of charge delocalization and improves the conductivity. Up to now, various protonic acids have been used as dopants during the process of synthesis. Commonly, these protonic acids were inorganic acids (e.g. HCl, H_2SO_4, H_3PO_4, and $HClO_4$) [58-60]. Recently, it has been reported that PANI doped with organic acids, such as benzenesulfonic acid (BSA)[61], sulfosalicylic acid (SSA)[62], camphorsulfonic acid (CSA)[63] and p-styrenesulfonic acid (PSSA)[64], are prone to improve their thermal stability.

To deal with the aggregation of TiO_2 nano-particles, we introduce attapulgite(ATT) into the material system. ATT is a species of hydrated manesium aluminum silicate non-metallic mineral [$(H_2O)_4(Mg,Al,Fe)_5(OH)_2Si_8O_{20} \bullet 4H_2O$] with commonly a fibrous morphology, is characterized by a porous crystalline structure containing tetrahedral layers alloyed together along longitudinal sideline chains[65]. Presently ATT has been widely used as adsorbents, adhesives, and catalyst supports, owing to its unique structure and considerable textual properties[66, 67].

2.3 Synthesis of TiO_2/PANI Nano-composites

ATT/TiO_2 (ATO) nano-particles were first prepared by heterogeneous nucleation method; then, ATT/TiO_2/PANI (ATOP) was synthesized by *in situ* polymerization in the presence of ATO nano-particles under various acids (HCl, SSA, HCl+SSA dual acid, $HClO_4$). The ATT was used as support to reduce the aggregation and improve the dispersibility of nano-particles, and reduce the thermal conductivity simultaneously. We systematically investigated the effects of various acid-doping on the morphology, crystallographic, thermal stability and thermoelectric properties of ATOP nano-composites.

Figure 1 shows the flow chart of preparation on the ATOP nano-composites. The ATT/TiO_2 (ATO) nano-particles were synthesized firstly. 10 ml Tetrabutyl titanate ($Ti(OBu)_4$) was dissolved into 100 ml absolute alcohol (C_2H_5OH) solution with a

smidgeon of triethanolamine (about 0.2 ml) by vigorous mechanical stirring (namely solution A). 1.3 ml HNO_3 in 2 ml distilled water was added to 10 ml absolute alcohol (namely solution B). Then solution B was added dropwise to solution A with vigorous stirring for 1 h at room temperature. After mixing uniformly, transparent, stable and flaxen TiO_2 sol was added dropwise to the pure ATT suspension with sonic stirring for 1h. After aging for 4 h in the air, the mixture was washed with distilled water. The resulting solid was dried at 353 K for 24 h and subsequently calcined at 723 K for 3 h; then the solid was ground into ATO nano-particles. The second step was to fabricate ATT/TiO_2/PANI (ATOP) nano-composites, which were synthesized by the oxidation of precursor with ammonium peroxydi-sulfate (APS) as oxidant. ATO (0.64g) was dispersed into 40ml 1.0 M acid solution (HCl, SSA, HCl+SSA dual acid, HClO4) by sonication respectively. Then 1.86g aniline and little surfactant hexadecyl trimethyl ammonium bromide (CTAB) were added into ATO acid solution under protection of nitrogen atmosphere. The molar ration of aniline/surfactant was taken as 10. After 30 min, APS (3.65g) in 20ml 1.0 M acid solution was added dropwise to this mixture. Polymerization was carried out at 273 K under nitrogen atmosphere with controlled stirring for 5 h. Dark green ATOP nano-composites was filtered and washed with distilled water before it is dried at 353 K under vacuum for 24 h.

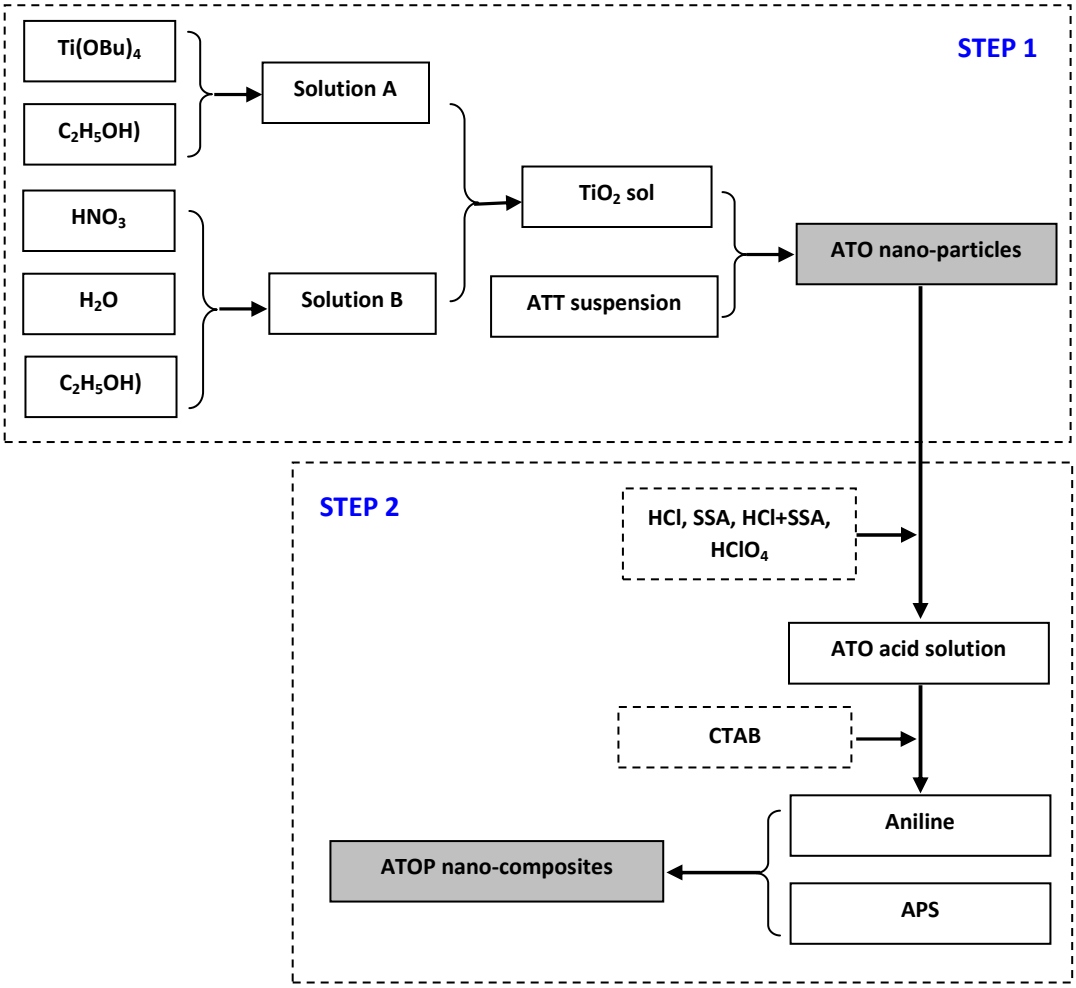

Figure 2.3 Flow chart of preparation on the ATOP nano-composites

2.4 Characterization of TiO_2/PANI Nano-composites

The surface morphology of the TiO_2/PANI nano-composites was examined by a Hitachi S-3000N scanning electron microscope (SEM). X-ray powder diffraction were performed on a D8 Advance diffractometer (XRD) using Cu-K_α radiation (λ=0.15405 nm). FTIR spectra were recorded using a Nicolet 5700 Fourier Transform Infrared Spectrometer in a dry-nitrogen atmosphere. Thermo-gravimetric analysis was performed with NETZSCH STA409PC thermal analyzer at a heating rate of 15 K/min from 298 K to 473 K under a nitrogen atmosphere. The thermal conductivity of the composites was measured using EKO HC-110 thermal conductivity test meter, which is based on a steady-state heat flux technique. The powder samples were in the form of compressed pellet (Φ22 mm×2 mm) for the thermoelectric related measurements. Electrical conductivity was measured by ST2253 four-probe tester. The Seebeck coefficient was tested on BHTE-08 Seebeck Measurement System.

2.4.1 Scanning Electron Microscopy

Figure 2.4 (a)-(d) shows the SEM micrographs of HCl, SSA, HCl+SSA and HClO4 doped ATOP nano-composites, respectively. Hereinafter these samples were denoted as ATOP-1, ATOP-2, ATOP-3, and ATOP-4. It can be seen that all the samples are of rod-like structure with a length of ~650 nm and diameter of ~100nm, which agrees with the fact that ATT is a type of natural fibrillar silicate clay mineral. Compared with

the pure ATT, the surface of samples is not smooth; and the dimensions of samples are increased. This may attribute to the extra TiO_2 and PANI coatings, confirming a good cladding structure.

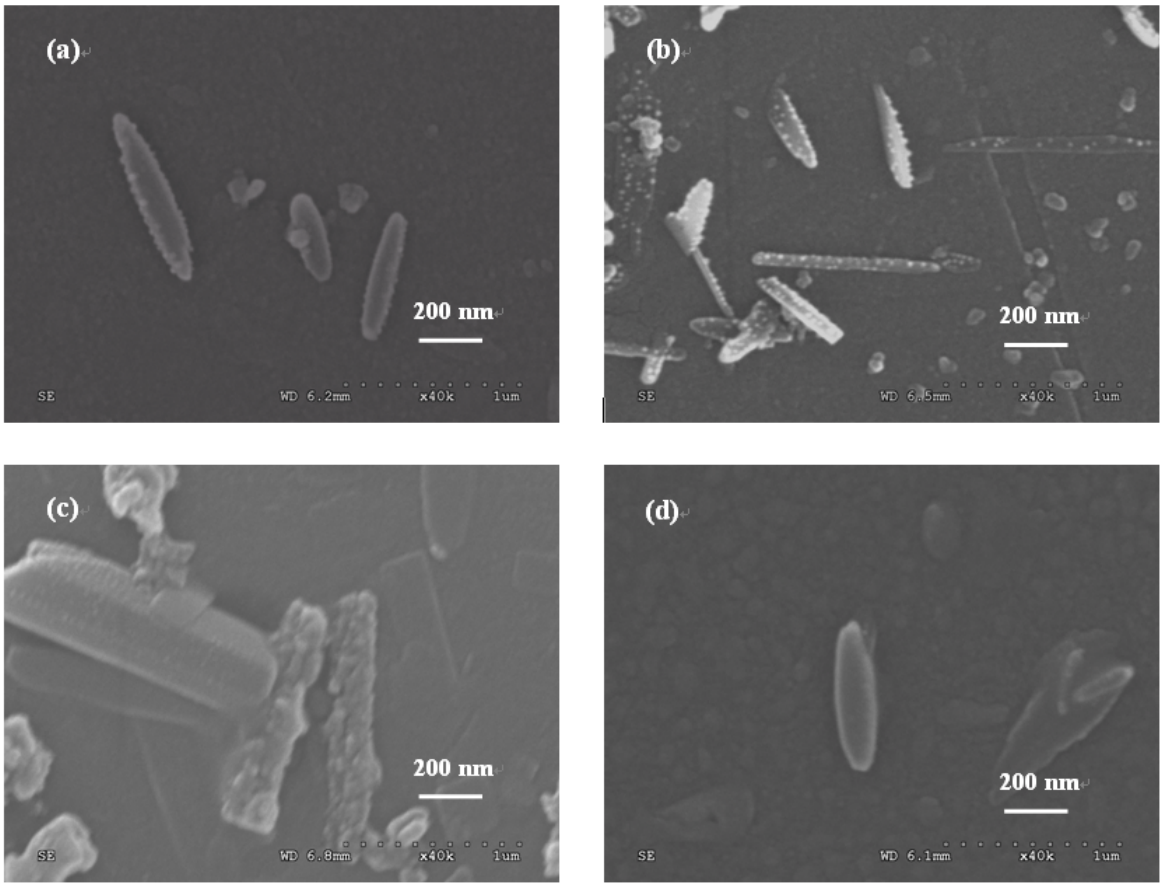

Figure 2.4 SEM image of ATOP nano-composites. (a) ATOP-1 nano-composites; (b) ATOP-2 nano-composites; (c) ATOP-3 nano-composites; and (d) ATOP-4 nano-composites.

2.4.2 X-Ray Powder Diffraction

Fig. 3 displays the XRD pattern of various acid-doped ATOP samples. Pure TiO_2, ATT and PANI are also listed for the comparison. It can be seen that the diffraction patterns of all ATOP samples match well with the typical patterns of ATT、PANI and TiO_2. The peaks at 8.56° can be observed in the doped samples, which is ascribed to {110} crystal face of ATT. The distinct peaks of 2θ at 25.4°, 38°, 48.3°, 54.1°, 55.2°, 53.9°, 62.8°and 70.5° are in agreement with the standard anatase TiO_2 XRD spectrum. Also the distinct peaks of 2θ at 15.1°, 20.8°and 25.4° agree with the standard PANI XRD spectrum, indicating the formation of PANI. Two peaks at 20.8° and 25.4° belong to periodicity parallel and perpendicular to polymer chain respectively. It is reported that there was a positive correlation between the conductivity and intensity of diffraction peaks at 25.4°. However, only according to the counts of diffraction peaks at 25.4°, we cannot deduce the order of electric conductivity among various acid-doped ATOP samples because the diffraction peaks at 25.4° belongs to two different materials.

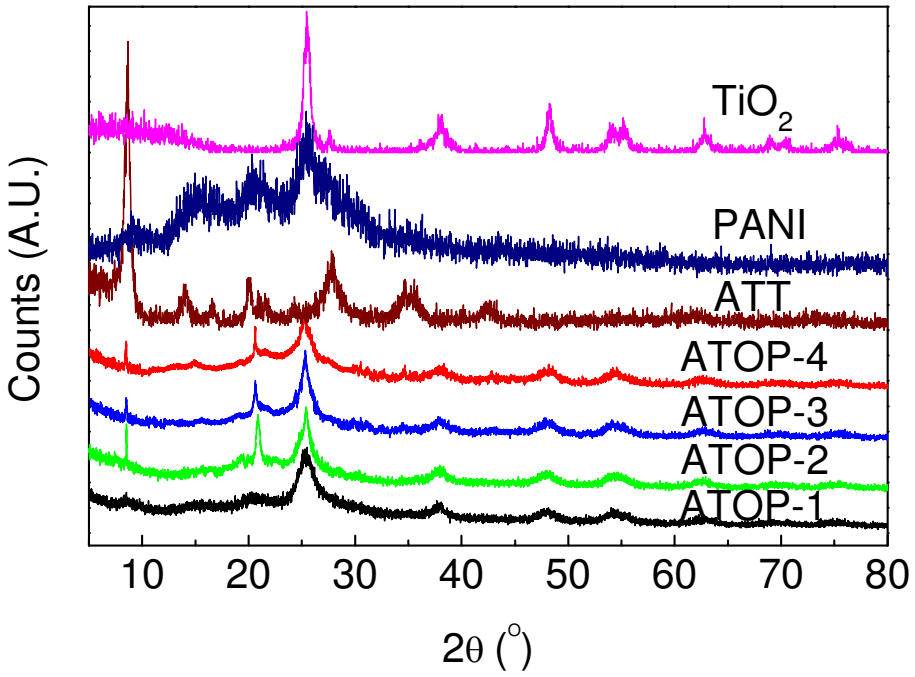

Figure 2.5 X-ray diffraction patterns of pure ATT, PANI, TiO_2, and ATOP nano-composites.

2.4.3 Fourier Transform Infrared Spectroscopy

The FTIR spectra of the ATOP samples are shown in Figure 2.6. The absorption band observed at 2912 cm-1 ~ 2851 cm-1 in the doped sample, can be ascribed to the surfactant DBSA; the absorption bands at 1676 cm-1 and 1019 cm-1 are assigned to the O=S=O stretching of organic acid. It should be noted that most PANI peaks of acid-doped ATOP samples are shifted to the lower wave number compared with that of the eigenstate PANI. Table 2.1 lists all the absorption bands in the spectra. The offset of vibration peaks can be calculated, comparing with the eigenstate PANI. The maximum offset occurs in N=Q=N bond, shifted by 22 cm-1 (ATOP-1), 6 cm-1 (ATOP-2), 26 cm-1 (ATOP-3), and 18 cm-1 (ATOP-4), respectively. This red shift phenomenon may result from conjugative effect after doped with acids. Some documents indicate that the dopants are mainly bonded with the nitrogen atoms in quinine-type. It is believed that acid-doping leads to a delocalization effect which decreases the force constant between atoms, and thus decreases the electron density on PANI chains in various levels. Similar results can be found in the published elsewhere[68].

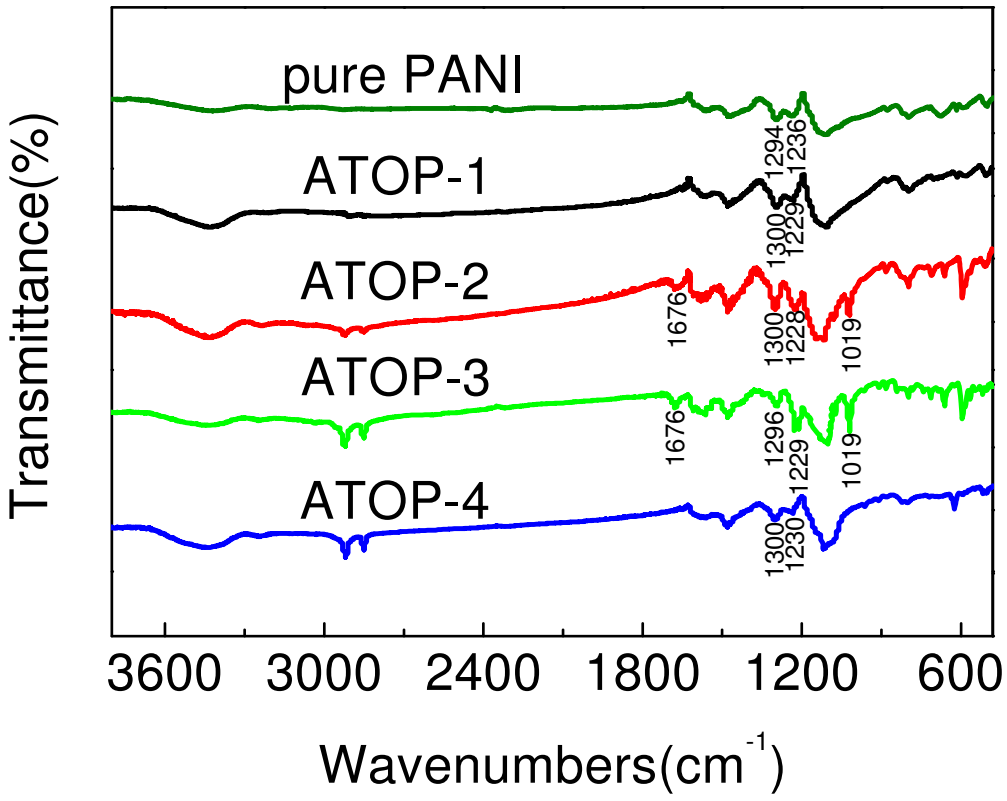

Figure 2.6 FT-IR spectra of pure ATT, PANI, TiO_2, and ATOP nano-composites.

Wavenumber（cm^{-1}）					Band characteristics
PANI	ATOP-1	ATOP-2	ATOP-3	ATOP-4	
3435	3430	3440	3436	3434	N-H stretching vibration
1586	1564	1580	1560	1568	N=Q=N vibration
1495	1480	1480	1480	1480	N-B-N stretching vibration
1230, 1302	1229, 1300	1228, 1300	1229, 1296	1230, 1300	Ar-N stretching
1121	1106	1115	1103	1109	C-H (Q) in of plane bending vibration
827	798	798	798	798	C-H (B) out of plane bending vibration
638	616	595	595	624	C-C (B) bending vibration

Table 2.1 Characteristic frequencies of Eigenstate PANI and various acids doped ATOP nano-composites

2.4.4 Thermogravimetry Analysis

The thermal analysis results of pure TiO_2, ATT, PANI and various acid-doped ATOP samples are illustrated in Fig. 5. It can be seen that the residual weight of acid-doped ATOP samples is much higher than those of pure TiO_2, ATT, and PANI. This means the thermal stability of ATOP samples can be improved after composite treatment. However, the weight loss of ATOP-1 sample is the largest, when the temperature is higher than 350 K, compared with that of other three acid-doped samples. Usually the weight loss of the samples at low temperature attribute to the removal of free water, absolute alcohol, acid and other small molecules. In fact, the weight loss of ATOP-2 sample is the minimum and that of the ATOP-3 is less. This result is in line with our expectation because hydrochloric acid is volatile; whereas organic acids and perchloric acid are less volatile. To sum up, the thermal stability of the ATOP samples doped with SSA is enhanced.

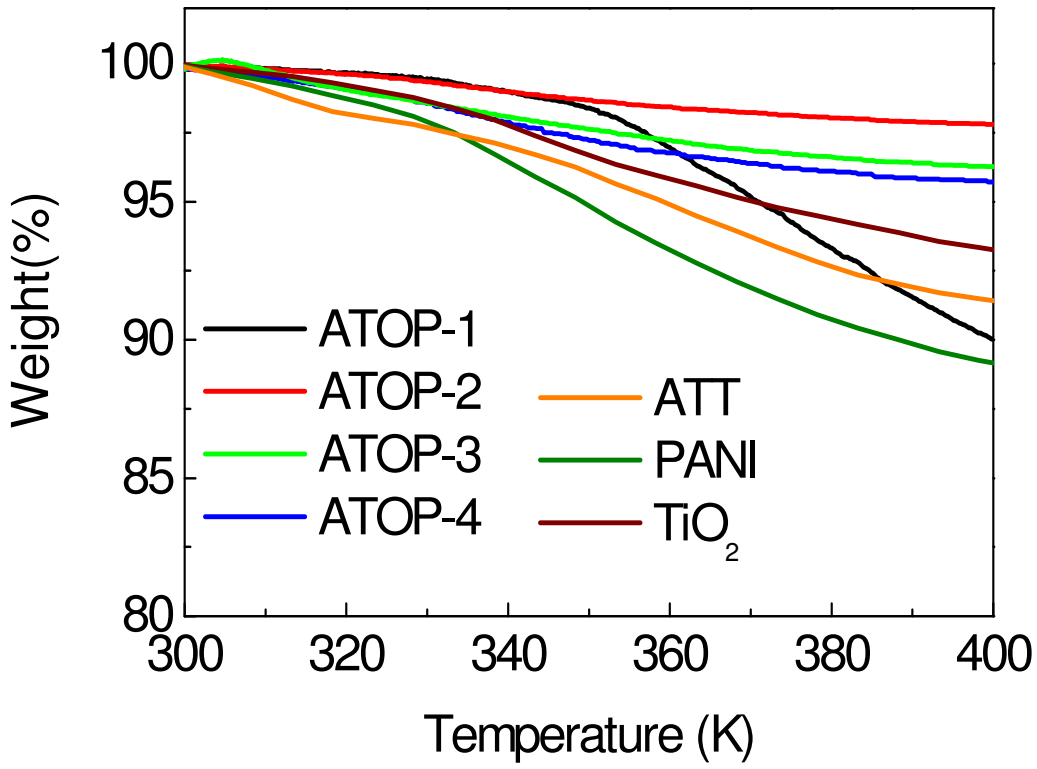

Figure 2.7 The TG analysis of pure ATT, PANI, TiO_2, and ATOP nano-composites.

2.4.5 Electrical Conductivity Measurement

The temperature dependence of electrical conductivity (σ) of pure TiO_2, PANI and various acids doped ATOP samples is shown in Figure 2.8. It is of interest that the ATOP nano-composites possess a higher electrical conductivity, compared with the pure TiO_2 and PANI. This probably originates from the compound of TiO_2 and PANI. On the one hand, TiO_2 can cause the regular arrangement of PANI chains; on the other hand, the cladding structure is conducive to electronic transfer along chain and jump between chains. Although the ATT belongs to insulator, the addition of it has no negative effect on electrical conductivity. In contrast, the electrical conductivity of ATOP samples has been improved. Moreover, it should be noted that the electrical conductivity of all the samples can reach several S/cm and exhibit a typical non-metallic temperature dependence ($d\sigma/dT>0$)[69]. This may be ascribed to the increase of the carrier concentration after the temperature elevated; and thus increase the electrical conductivity[70]. In our present work, the electrical conductivity of ATOP-3 sample is the best; it reaches the maximum (6.67 S/cm), 2 times more than that of PANI (2.58 S/cm) at 373K.

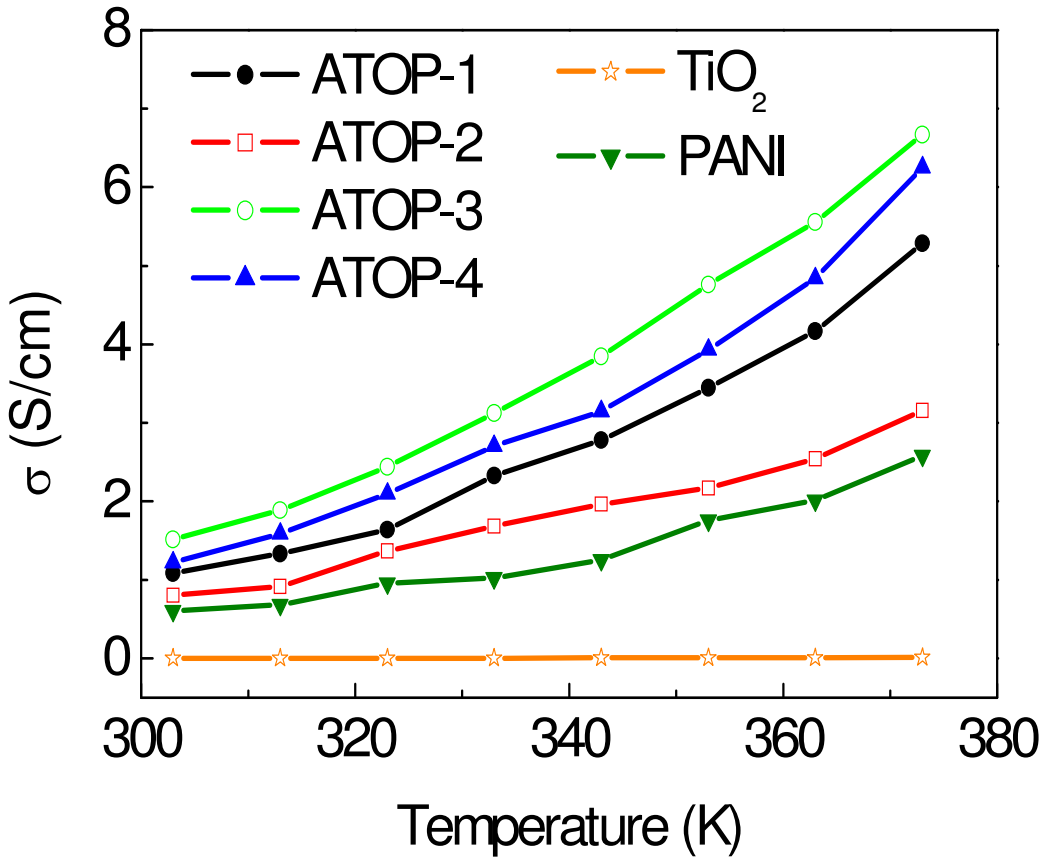

Figure 2.8 The temperature dependence of electrical conductivity of pure TiO_2, PANI, and ATOP nano-composites.

2.4.5 The Seebeck coefficient Measurement

Figure 2.9 shows the temperature dependence of the Seebeck coefficient (α) for pure TiO_2, PANI and various acids doped ATOP samples. The Seebeck coefficient shows an opposite trend to that of electrical conductivity. The pure TiO_2 and PANI are proved to be n-type inorganic semiconductor and p-type organic semiconductor, respectively. The ATOP nano-composites are classified as p-type. It is encouraging to find out that the Seebeck coefficient of acid-doped ATOP samples is about 2-4 times higher than that of pure TiO_2 and PANI. In addition, the Seebeck coefficient decreases with the temperature increasing attribute to the increase of carrier concentration[71]. The Seebeck coefficient of ATOP-3 sample is better than others in the range of 320-373 K; it keeps a higher value (57 μV/K) at 363K.

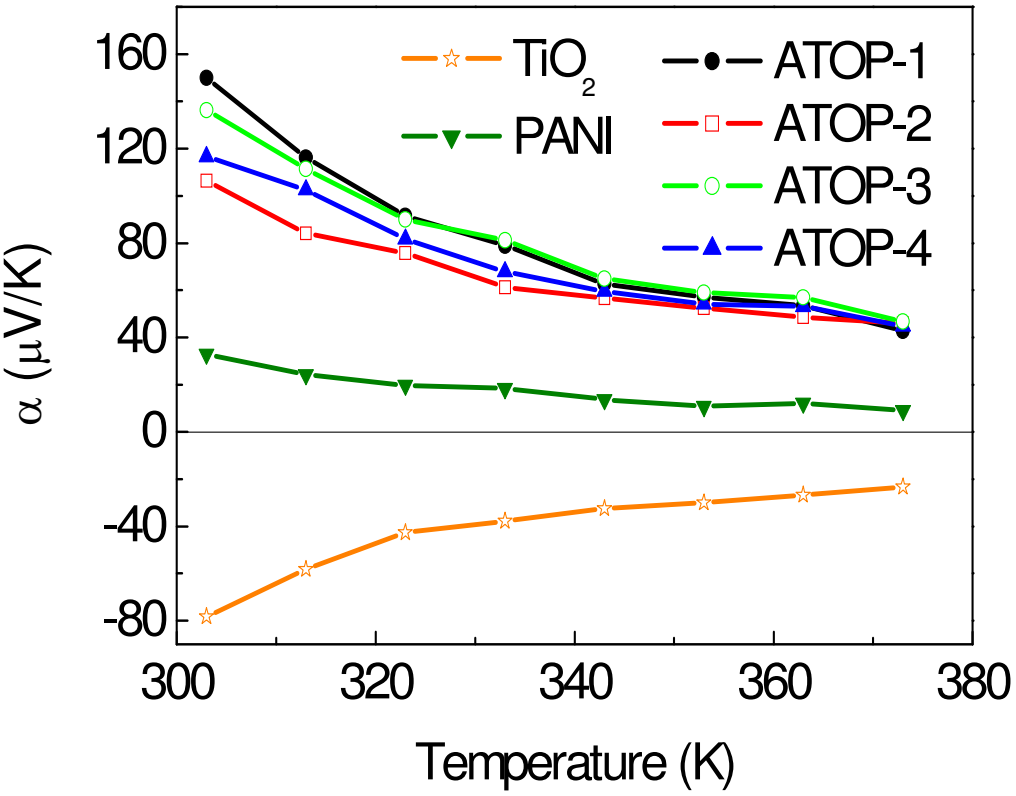

Figure 2.9 The temperature dependence of Seebeck coefficient of pure TiO_2, PANI, and ATOP nano-composites.

2.4.6 Figure of Merit

The thermoelectric figure-of-merit (*ZT*) is a common measure of a material's energy conversion efficiency:

$$ZT = (\alpha^2\sigma/\kappa)T \qquad \textbf{Equation 2.1}$$

Where α, σ, κ, and T are Seebeck coefficient, electrical conductivity, thermal conductivity and absolute temperature respectively.

The thermal conductivity of ATT is about 0.06 $Wm^{-1}K^{-1}$ and that of PANI is around 0.3 $Wm^{-1}K^{-1}$ at room temperature[72, 73]. Mun et al. have reported the thermal conductivity of TiO_2 is 0.5 $Wm^{-1}K^{-1}$ [74]. The average thermal conductivity of ATOP nano-composites is about 0.148 $Wm^{-1}K^{-1}$. We also note that the thermal conductivity do not change significantly with the temperature increased. For example, the thermal conductivity of ATOP-3 is about 0.155 $Wm^{-1}K^{-1}$ at 323 K, and is about 0.144 $Wm^{-1}K^{-1}$ at 373 K. This means that the addition of ATT can reduce the thermal conductivity efficiently and maintain a good stability over a wide temperature range.

The *ZT* of ATOP nano-composites can be calculated according to the equation 1. Figure 2.10 shows the *ZT* of ATOP-3 nano-composites as a function of temperature. Though *ZT* decrease slightly with the increase of temperature, dropped from 5.88×10^{-3} at 303K to 3.82×10^{-3} at 373K, ZT still maintain a relative higher value according to our evaluation. The ZT of ATOP-3 nano-composites is several hundred times larger than that of pure TiO_2 and PANI, which is 0.48×10^{-4} and 0.26×10^{-4} at 373K, respectively. Li *et al* have reported the maximum of ZT in doped PANI is 1.2×10^{-4} at 373 K[69]. Though the data is slight higher than our experimental, their magnitude is equivalent. Compared with

the existing literature on TiO_2, PANI or their composites, the ZT of ATOP-3 nano-composites is the largest. We believe that HCl+SSA dual acids doped ATT/TiO_2/PANI nano-composites can be promising for thermoelectric applications, especially in power generation with low temperature heat, e.g. exhaust gas, terrestrial heat, solar energy, etc. Therefore, even if a little part of waster can be converted into electricity, its impact on the energy situation would be enormous.

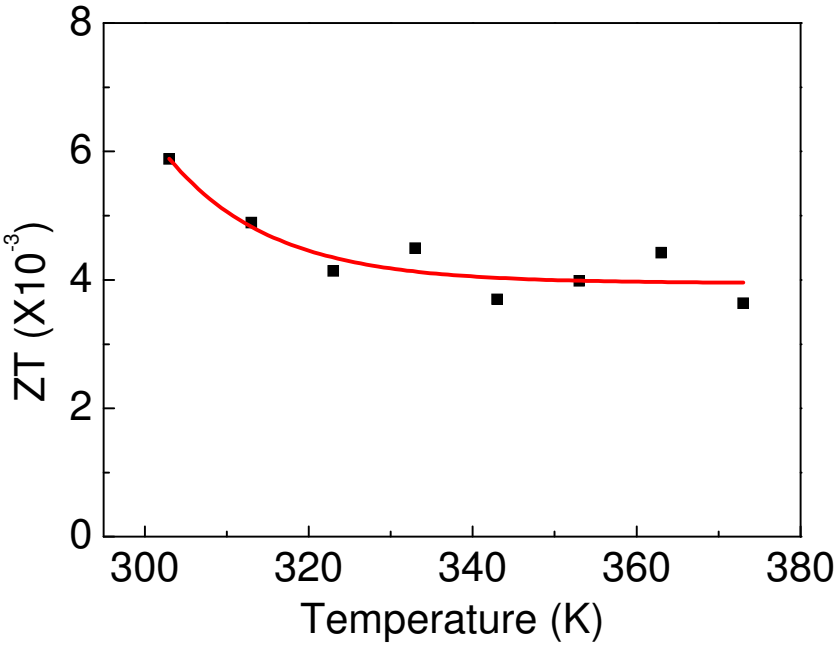

Figure 2.10 The temperature dependence of ZT of ATOP-3 nano-composites.

2.5 Summery

Acid-doped ATOP nano-composites are of rod-like structure with a length of ~ 650 nm and diameter of ~100nm. Acid-doped ATOP nano-composites possess a higher Seebeck coefficient, electrical conductivity, and a lower thermal conductivity compared with pure TiO_2, PANI or their composites. The electrical conductivity of ATOP-3 nano-composites can reach 6.67 S/cm at 373K and exhibit a typical non-metallic temperature dependence. The Seebeck coefficient of ATOP-3 sample is 57 μV/K at 363K, about 2-4 times higher than that of pure TiO_2 and PANI. The addition of ATT can reduce the thermal conductivity of ATOP nano-composites, and maintain a good stability over a wide temperature range. The thermal conductivity of ATOP nano-composites is about 0.148 $Wm^{-1}K^{-1}$. Compared with other samples, the ZT of HCl+SSA dual acids doped nano-composites is the largest and is several hundred times larger than that of pure TiO_2 and PANI. Moreover, it can maintain a relatively larger value, 3.82×10^{-3} at 373K. It is strongly believed that HCl+SSA dual acids doped ATOP nano-composites could be promising for power generation with low temperature heat.

CHAPTER 3 POLYSTYRENE-ANATASE TITANIUM DIOXIDE NANOCOMPOSITE

The dispersion of nanometer-sized fillers within polymeric matrices can affect significantly their physical properties. The main source of these modifications is due to the interface macromolecular chains-nanofiller and the large surface area of the nanofiller. Technically, in such nanocomposites, the physical properties of the interface become dominant over the bulk properties of the polymeric matrices.

The addition of nanometer-sized fillers to polymeric matrices typically affects the thermal and thermo-oxidative degradation of the polymer, the Young modulus, the strength of the polymeric matrix and the crystallization process. In most cases, the effect of nanofillers consists in a rather modest increase of the temperature at which the mass loss of the polymer is highest. This parameter, easily obtained by TGA analysis (more frequently done in inert atmosphere) can be considered as a fingerprint of the formation of a polymer-nanoparticle interface.

3.1 Synthesis of Polystyrene/TiO_2 composites

TiO_2 nanoparticles with a dominant anatase structure, spherical morphology, and an average particle size of about 15 nm were purchased from Nanostructured and Amorphous Materials Inc. and used as received. The polymeric matrix (atactic polystyrene) was purchased from Sigma-Aldrich. PS-TiO_2 nanocomposites loaded with various amounts of anatase ranging between 0 % wt. and 11 % wt., have been obtained

by dissolving PS in cyclohexane (CH), who is a theta solvent at room temperature. Consequently, the interactions between the polymeric segments are balanced by the interactions with solvent's molecules. TiO_2 nanoparticles have been added to the PS-CH solution and the as obtained mixture was sonicated at 1 kW for 100 minutes by using a Hielscher sonicator. This process aimed to a homogeneous distribution of nanoparticles within PS. As no significant shifts in the glass transition temperature of polystyrene was noticed after the sonication of PS-CH solution for 100 minutes, it was concluded that PS is not degraded by sonication. The as obtained homogeneous solution was cast on microscope glass slides. It was noticed (from TGA data) that the solvent was not fully removed after storing the samples in air, at room temperature for a week. Consequently, an additional heat treatment of PS-TiO_2 films in a vacuum oven at 150 ℃, for 3 hours, has been performed. TGA data confirmed the complete removal of the solvent after this additional thermal treatment, within an ± 1% accuracy. TGA measurements have been performed in nitrogen atmosphere by using a TGA Q 500 instrument. The as obtained thermograms (residual mass versus temperature and mass derivative versus temperature) were fitted by using Origin 8.1 Pro (both built-in functions as well as user defined functions).

3.2 Thermogravimetric Analysis

This subsection was focused on the simulation of Thermogravimetric Analysis data, aiming to a refined understanding of the interactions between of polystyrene and TiO_2 nanoparticles. The dependence of the first derivative of residual mass on temperature has been used to determine more accurately the temperature at which the mass loss is maximized. Several functions have been used to simulate the dependence of the first derivative of mass loss on the temperature of the sample. An increase of the thermal stability of the polymeric matrix upon loading with TiO_2 was also investigated.

3.2.1 Introduction of TGA Curve and Avrami Equation

Thermogravimetric Analysis (TGA) examines the dependence of the mass of the sample on temperature, in a controlled atmosphere. TGA curve of polystyrene (PS) and polystyrene-TiO_2 (PS-TiO_2) nanocomposites in nitrogen atmosphere are single sigmoids, characterized by a single inflection point. The mass of the sample starts to decrease slowly; as the temperature is increased the mass loss rate becomes larger and larger until the inflection temperature T_i is reached. At the inflection point, the mass loss rate m_i is highest. As the temperature exceeds T_i, the mass loss starts to decrease and eventually becomes zero (when all the mass of the sample is volatilized). The thermogravimetric analysis was performed on Q 500 TGA TA Instruments, Figure 3.1.

Figure 3.1 Q 500 Thermogravimetric Analyzer

Avrami equation[75] can be used to describe the temperature evolution of the mass of a polymer or polymer-based nanocomposites.

$$m(T) = m(T_0) + Ae^{-C(T-T_0)^n} \qquad \textbf{Equation 3.1}$$

where $m(T)$ is the residual mass at a temperature T, $m(T_0)$ is a fitting constant associated to the position of the zero line, A is the amplitude of the degradation process (amount of vaporized polymer), T_0 represents the temperature at which degradation starts, C is a constant connected to the volatilization rate, and n is a parameter. Avrami equation has been frequently used to investigate crystallization processes. In our cases, n is ranging between 0.5 and 4 and C is positive and smaller than 1.

TGA allows also the recording of the mass derivative as a function of temperature. Such dependence presents a single maxim at the inflection point of the mass versus temperature dependence. A detailed analysis reveals that this derivative is not perfectly symmetric, while the Avrami equation describes symmetrical sigmoids. This justifies the effort to find better functions to simulate the dependence of the mass derivative on temperature.

3.2.2 Interface between Polymer and Nanoparticles

Typically, the filling of polymeric matrices by nanoparticles results in the formation of a polymer-nanoparticle interface. Due to the huge surface area of nanoparticles, the fraction of polymer belonging to this interface can be appreciable and consequently the physical properties of the polymeric matrix modified[25]. In most cases, this interface increases the stability of polymeric matrices shifting the inflection temperature towards higher values. The increase of the concentration of nanoparticles enhances the total surface of nanoparticles, confining more and more polymer within the interface. A saturation point is expected, where (almost) all polymer is interacting with the nanofiller.

3.2.3 Experimental Results and Discussions

The dependence of mass loss versus temperature for some PS-TiO_2 nanocomposites containing various amounts of TiO_2 is shown in Figure 1. The actual

thermograms are represented by single sigmoids. The TGA measurement is from room temperature to 700°C by 10°C heating rate. It is noticed that the temperature at which the mass loss reaches the highest value (i.e. the inflection point, or T_M) increases by more than 25℃ as the concentration of the filler is increased up to 11wt%. Further increase of the filler concentration does not resulted in a further increase of the degradation temperature. This demonstrates the formation of an interface between the nanofiller and the nanocomposites.

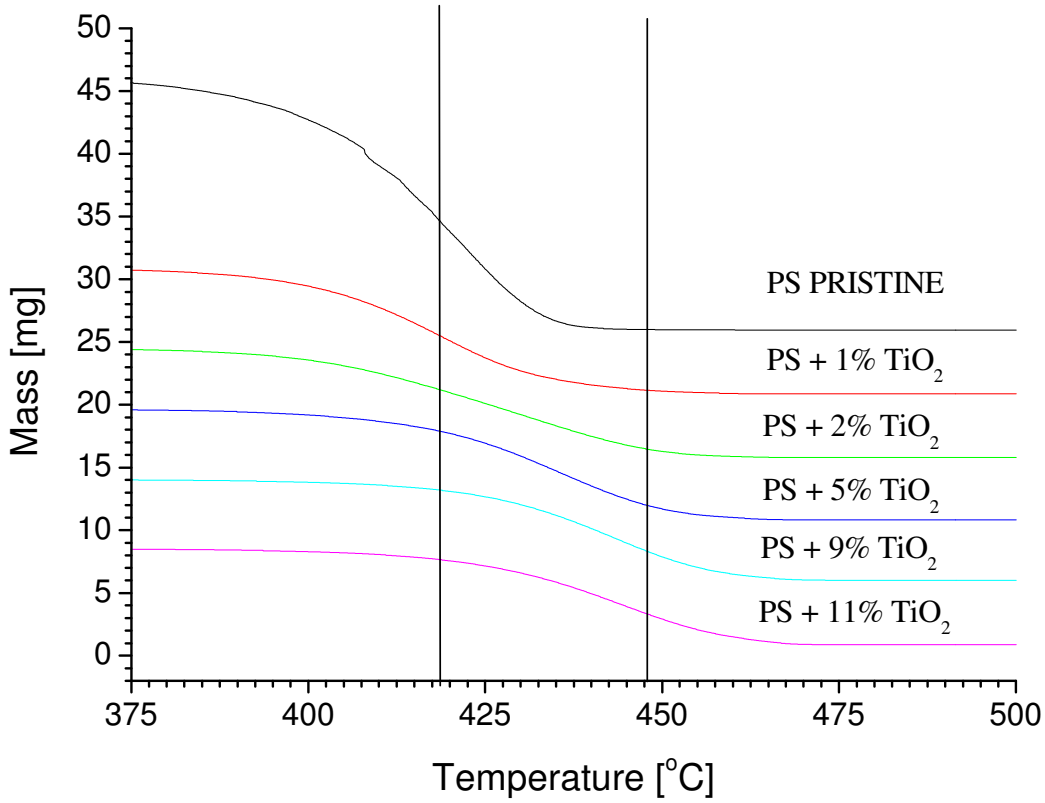

Figure 3.2 TGA thermograms of PS loaded with various amounts of TiO_2 [% wt.]

In order to determine accurately T_M and the width of the thermal degradation process the as recorded thermograms have been fitted by a modified Breit-Wigner lineshape.

$$M(T) = M_0 \frac{1 + p(\frac{T - T_0}{d})}{[1 + (\frac{T - T_0}{d})^2]} \qquad \textbf{Equation 3.2}$$

Where M_0 is the mass of the sample, at the inflection temperature T_M, d describes the width of the thermal degradation process, and p is a parameter associated with the departure from a symmetric Lorentz line.

3.2.4 Mathematical Simulation on Thermal Analysis

The temperature dependence of the mass derivative (which is the first derivative of the residual mass versus temperature) can be described with an acceptable accuracy by using symmetrical equations such as simple Gaussian (Equation 3.3) and Lorentzian (Equation 3.4) line shapes. The inflection point of the mass versus temperature dependence is converted into an extreme point in the mass derivative versus temperature dependence.

$$m_d(T) = m_{d0G} + A_G e^{-\frac{(T-T_{iG})^2}{W_G^2}} \qquad \textbf{Equation 3.3}$$

$$m_d(T) = m_{d0L} + \frac{A_L W_L}{W_L^2 + (T-T_{iL})^2} \qquad \textbf{Equation 3.4}$$

where m_{d0G} adjust the zero, A_G and A_L are the amplitudes of mass loss rates, T_{iG} and T_{iL} are the temperature at which the mass loss is maxim, W_G and W_L describe the width of the dependence mass derivative m_d versus temperature. The subscripts G and L identifies the Gaussian and Lorentzian lineshapes. While this approach results in reasonable values for the extreme (inflection) temperatures, it fails to explain the asymmetry of experimental data.

Based on the fact that either Lorentzian or Gaussian lineshapes describe with an acceptable accuracy the dependence of m_d on temperature, a convolution like line shape (Voigt-see Equation 3.5) was considered to fit the asymmetrical data.

$$m_d(T) = m_{d0V} + A_V(2\alpha/\pi)\frac{W_L}{W_L^2 + 4(T - T_{iV})^2} + (1-\alpha)\sqrt{\frac{4\ln 2}{\pi W_G}}e^{-\frac{4\ln 2}{W_G^2}(T-T_{iV})^2} \qquad \textbf{Equation 3.5}$$

where α is a fitting parameter and the subscript V identifies the Voigt line shape. Asymmetrical lineshapes have been simulated in spectroscopy by using various functions. The Breit-Wigner-Fano (BFW - see Equation 3.6) lineshape has been frequently used to simulate asymmetrical Raman spectra:

$$m_d(T) = m_{doBWF} + A_{BWF}\frac{1 + p(\frac{T - T_{iBWF}}{W_{BWF}})}{[1 + (\frac{T - T_{iBWF}}{W_{BWF}})^2]} \qquad \textbf{Equation 3.6}$$

Where the fitting parameter p describes the deviation from the Lorentzian lineshape. An asymmetric lineshape is typically associated with a non constant width; i.e. the width of the left side is not identical to the width of the right side of the extreme (inflection) point. Accordingly, the dependence of the mass derivative on temperature has been fitted by asymmetrical Gaussians and BWF lineshapes (see Equation 3.7and Equation 3.8):

$$m_d(T) = \begin{cases} m_{d0G2} + A_{GL}\exp-\dfrac{(T - T_{iG})}{w_{GL}^2} & T < T_{iG} \\ m_{d0G2} + A_{GR}\exp-\dfrac{(T - T_{iG})}{w_{GR}^2} & T \geq T_{iG} \end{cases} \qquad \textbf{Equation 3.7}$$

$$m_d(T) = \begin{cases} m_{doBWF2} + A_{BWFL} \dfrac{1 + p_L(\dfrac{T - T_{iBWF}}{W_{BWFL}})}{[1 + (\dfrac{T - T_{iBWF}}{W_{BWFL}})^2]} & T < T_{iBWF} \\ m_{doBWF2} + A_{BWFR} \dfrac{1 + p_R(\dfrac{T - T_{iBWF}}{W_{BWFR}})}{[1 + (\dfrac{T - T_{iBWF}}{W_{BWFR}})^2]} & T > T_{iBWF} \end{cases} \quad \textbf{Equation 3.8}$$

where L and R identifies the left and right sides of the lineshape. Tentatively, a continuous and monotonous modification of the linewidth across the lineshape was considered and embedded within an extended BWF equation (see Equation 3.9).

$$m_d(T) = m_{d0BWFE} + A_{BWFE} \frac{[2W_{BWFE} e^{-\alpha T} + p_0(T - T_{iBWFE})]}{[W_{BWFE}^2 e^{-2\alpha T} + 4(T - T_{iBWFE})^2]} \quad \textbf{Equation 3.9}$$

Where α describes the dependence of the line width on T. For p_o=0 and α=0 eq. 8 degenerates into a symmetrical Lorentzian line.

Figure 3.3 shows the best fits obtained by using the above mentioned equations for pristine PS. Similar fits have been obtained for each PS-TiO_2 sample. For the fit of Gaussian, Lorentzian, and Voigt line shapes the built-in functions of Origin 8.1 PRO have been used. All other lineshapes were fitted by using the user-defined function capability, in °C.

The analysis of the resonance lineshape revealed that the overall degradation process can be described by several parameters such as the temperature at which the mass loss rate is maxim. the maxim value of the mass loss, the width of the mass derivative dependence on temperature and the asymmetry parameter, defined as the ratio between

the left and the right widths. Unexpectedly, the continuous variation of the linewidth (as exp-αT) did not result in an improved agreement between experiment and fitting function.

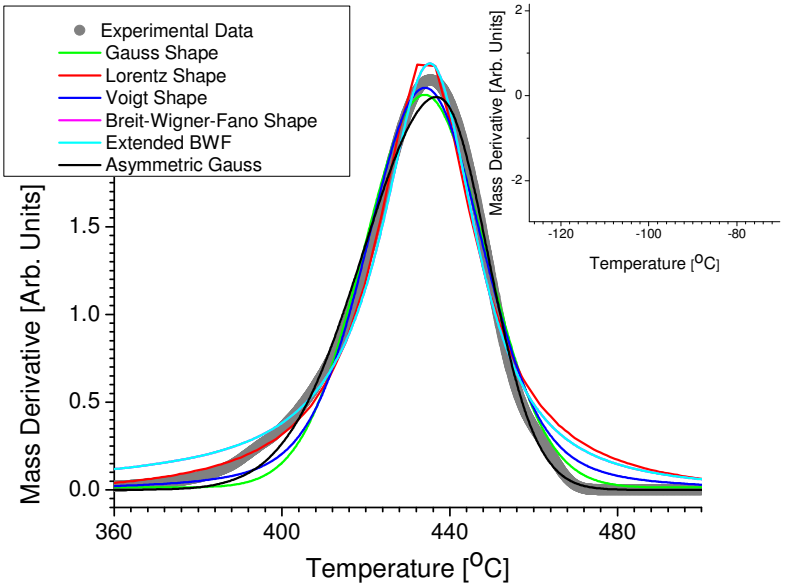

Figure 3.3 Mass derivative versus temperature for pristine PS. Experimental data (thick lines) and best fits (thin lines)

Samples of PS-TiO_2 containing residual amounts of solvent (CH) have been measured by TGA. Figure 3.4 depicts the temperature dependence of the mass derivatives (thick line) and the best fit obtained by connecting two Gaussians. The fit is excellent, demonstrating that Equation 3.7 can be used even for two competing processes. The fitting reveals that the peak related to solvent evaporation is completely symmetric whereas the proper thermal degradation peak has an asymmetry (i.e. ratio between the left width and right width equal to 1.18±.05 °C) significantly larger than experimental errors. Previous TGA data on isotactic polypropylene filled with vapor grown carbon nanofibers demonstrated that the width of mass derivative versus temperature reflects the

changes in the thermal conductivity of the sample. Based on TGA data, we suggest that the width of mass derivative versus temperature is affected by diffusion processes, thermal conductivity, and energy barriers. Hence, a complete analysis of TGA data should include the extreme (inflection) temperature, the mass loss at the extreme (inflection) temperature, the asymmetry ratio, and the width of the recorded line shape.

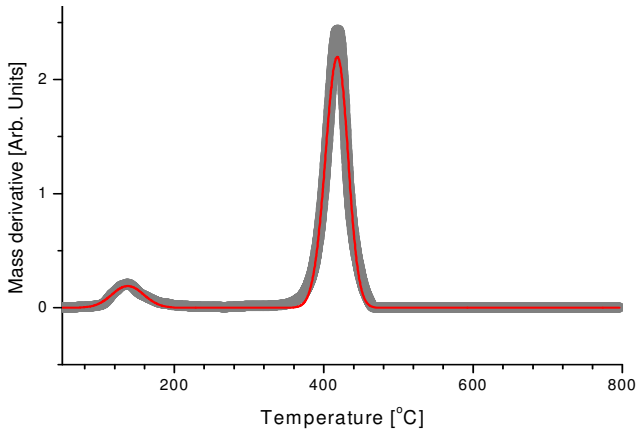

Figure 3.4 Thermogram of PS-TiO_2 containing solvent (CH) residues

The best fit of the mass derivative dependence on temperature has been obtained for the double Gaussian dependence (see Equation 3.7). This demonstrates that the shape asymmetry implies different linewidth on the left and on the right of the extreme temperature T_i. While thermal degradation processes that involve complex chemical reactions were characterized by asymmetric lineshape, the thermal evaporation of residual solvent was described by a symmetric lineshape. This suggests that the possibility to determine the width and the asymmetry of thermograms may add additional information about the overall thermal degradation process. It was speculated that the

linewidth includes information about the thermal conductivity of the sample and diffusion constants.

3.3 Raman Spectroscopy and Wide-angle X-ray Scattering

The atomic and molecular vibrations of polystyrene and TiO_2 nanoparticles in nanocomposites materials can be revealed by Raman spectroscopy. The dispersion of nanoparticles within polymeric matrices results in the appearance of an interface between the nanoparticles and macromolecular chains. Due to the huge surface area of nanoparticles, the enhanced physical properties of the interphase start to control the behavior of polymer-based nanocomposites. The present study focuses on the atomic and molecular vibrations of polystyrene and TiO_2 nanoparticles in nanocomposites materials-as revealed by Raman spectroscopy.

Here the novel synthesis of a polymer-nanofiller composite obtained by exploiting the physical characteristics of theta solvent and theta temperature is investigated. The main feature of a polymer in a theta solvent at theta temperatures is that the second virial coefficient becomes zero. The theta temperature (or Flory temperature) is the temperature at which the interactions between macromolecular units are balanced by the interactions between macromolecular units and solvent molecule. At this temperature, the macromolecular chain reaches the maximum extend while not being subjected to intermolecular forces (in equilibrium). The size of the macromolecular chains in good solvents is typically larger than the size of the same macromolecular chain at theta

temperature. This reflects the effect of the solvent – polymer segments interactions. The goal of this research was to take advantage of the theta solvent/theta temperature characteristics to obtain a better dispersion of nanofillers (in this case are TiO_2 nanoparticles) within macromolecular chains and to reduce at maximum the mechanical perturbation of macromolecular chains due to polymer segment-solvent interactions.

Raman spectra have been obtained using a Bruker Senterra micro Raman spectrometer operating at 785 nm (see Figure 3.5). The laser power was kept at 1 mW, in order to avoid the thermal destruction of samples.

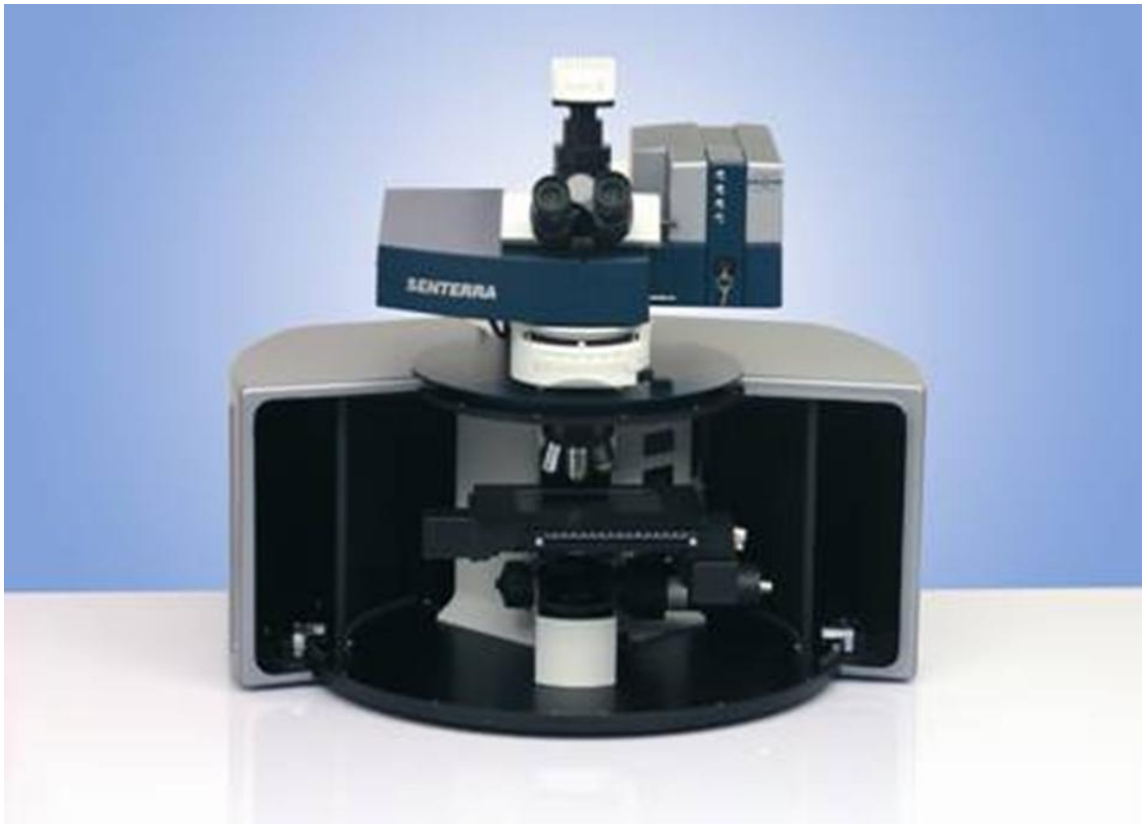

Figure 3.5 Bruker Senterra micro Raman spectrometer

Raman spectra have been fitted by a Breit-Wigner lineshape

$$I(w) = I_0 \frac{1 + p(\frac{w - w_0}{d})}{[1 + (\frac{w - w_0}{d})^2]}$$ **Equation 3.10**

Where I_0 is the amplitude of the Raman line, at resonance, ω is the shift of the Raman line, w_0 identifies the position of the Raman line, d describes the width of the Raman line, and p is a parameter associated with the departure of the Raman lineshape from the theoretical symmetrical Lorentzian line.

For a more accurate deconvolution of Raman lines, ranges containing up to 10 lines have been fitted. The actual expression used to simulate the Raman spectrum in each range was:

$$I(spectrum) = \sum_{j=1}^{10} I_{0j} \frac{1 + p_j(\frac{w_j - w_{0j}}{d_j})}{[1 + (\frac{w_j - w_{0j}}{d_j})^2]} + A + Bw + Cw^2$$ **Equation 3.11**

Where A, B, and C are parameters defining the base line correction (up to the quadratic term) and j identifies the component of the Raman line.

PS showed Raman lines below 300 cm^{-1}. These lines, typically define the boson peak, are associated to the amorphous features of the polymeric matrix. The actual spectrum of PS containing 10 % TiO_2 in the Raman shift range 100 to 900 cm^{-1} is shown in Figure 3.6. A very good correlation is noticed between the experimentally obtained spectrum (black circles- see Fig. 2) and the simulated spectrum (red line). Similar data for the shifts ranging from 900 cm^{-1} to 1400 cm^{-1} and from 1500 cm^{-1} to 2100 cm^{-1}.

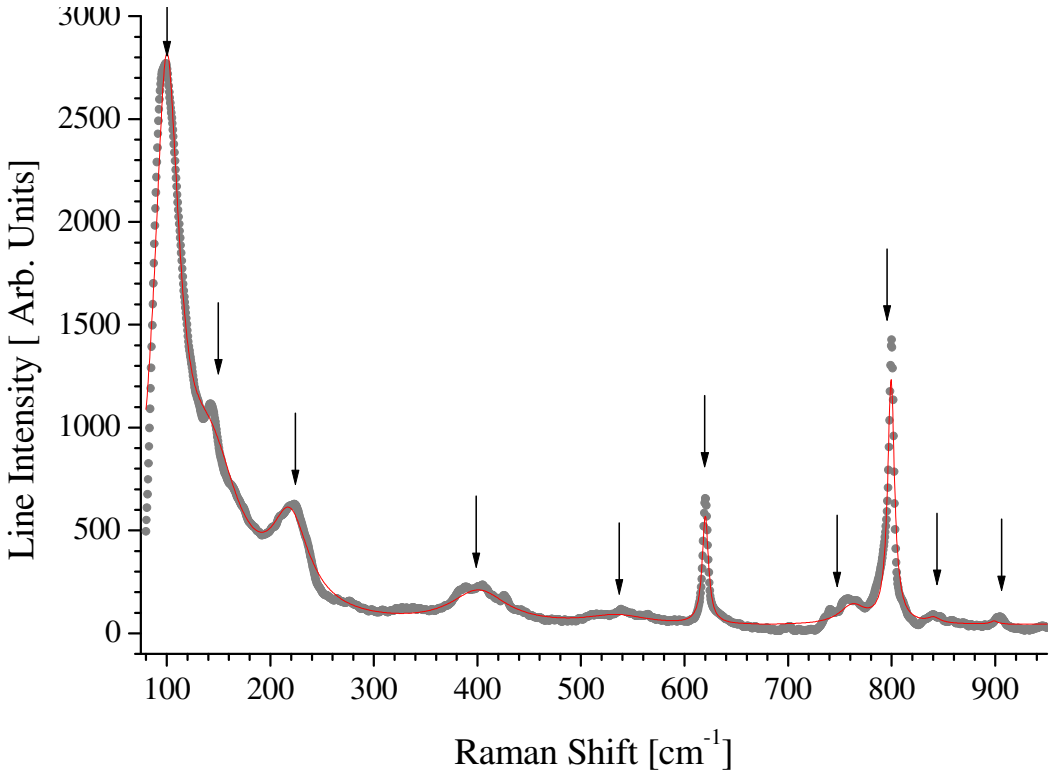

Figure 3.6. Raman spectrum of PS-TiO_2 at low Raman shifts

WAXS spectra of TiO_2 nanoparticles dispersed within PS (10 % wt TiO_2), at various temperatures ranging from 25 ^oC to 105 ^oC are shown in Figure 3.7. The line amplitude and position confirmed that anatase is the dominant phase.

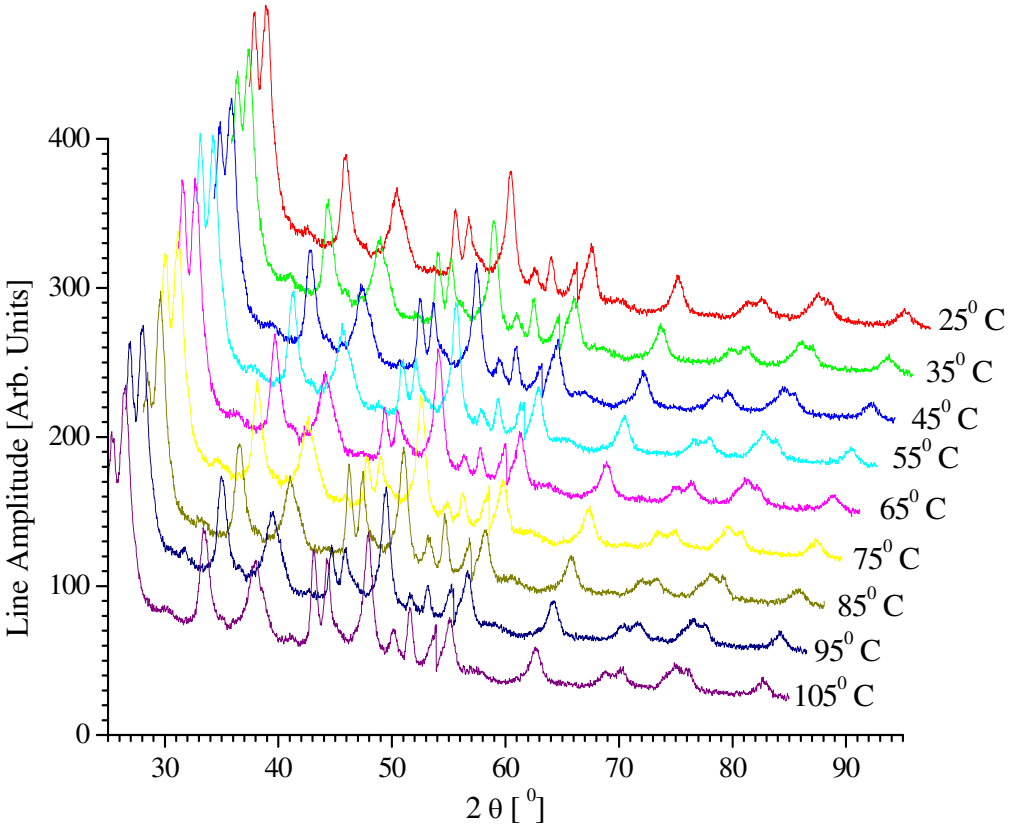

Figure 3.7. WAXS spectra of PS-TiO_2 composites containing 10 % wt. TiO_2.

CHAPTER 4 POLYSTYRENE-POLYANILINE-TIO_2 TERNARY POLYMERIC NANOCOMPOSITE

4.1 Introduction

The thermoelectric effect describes the direct conversion of a temperature difference into an electric voltage or the direct conversion of an applied electric voltage into a temperature difference. The performance of thermoelectric materials (TEM) is quantified by the merit factor MF, which depends on temperature *T*, the electrical conductivity σ, the thermal conductivity λ, and the Seebeck coefficient *S*:

$$M_F = \frac{\sigma S^2 T}{\lambda} = ZT \qquad \textbf{Equation 4.1}$$

Where *Z* is the merit figure parameter. A simple inspection of Equation 4.1 shows that in order to increase the merit factor is necessary to increase the electrical conductivity and to drop the thermal conductivity. A large Seebeck coefficient is extremely important for high performance TEM. Typically, high electrical conductivities are associated with large thermal conductivities and consequently the requirements for high merit figure are contradictory.

In order to decouple the electrical features from the thermal characteristics, the research focused on nanocomposites obtained by dispersing conducting nanoparticles within an insulating phase. The nanometer-size confinement of the thermoelectric component limits the values of the thermal conductivity. In order to maintain a sufficiently large electrical conductivity for the thermoelectric composite (TEC) and

eventually to reach a high MF, polyaniline (PANI), which is a conducting polymer was considered as component of the TEC. PANI has a high electrical conductivity and good thermal and thermo-oxidative stability. However, PANI does not exhibit good mechanical properties. To achieve a high quality TEC, the research was focused on a ternary system consisting of polystyrene (PS), polyaniline, and TiO_2. In this TEC polystyrene provides the mechanical strength, PANI is a conducting polymer that provides an additional increase of the electrical conductivity, and TiO_2 nanoparticles are the thermoelectric component.

The dispersion of nanoparticles within polymeric matrices results in the appearance of an interface between the nanoparticles and macromolecular chains. Due to the huge surface area of nanoparticles, the enhanced physical properties of the interphase start to control the behavior of polymer-based nanocomposites. The present study concentrates on the thermal analysis of ternary nanocomposites PS-PANI-TiO_2.

4.2 Methodology

Almost cubic TiO_2 nanoparticles (anatase) with a size of about 15 nm have been purchased from Nanostructured and Amorphous Materials, Inc. Atactic polystyrene (PS) has been purchased from Sigma Aldrich. PS is an amorphous polymer with almost 0 % degree of crystallinity, good mechanical properties, soluble in selected organic solvents, characterized by a glass transition temperature of about 100 ^oC. High conductivity PANI polymer has been purchased from Sigma.

The ternary TEC system has been obtained by dissolving the polymeric matrix (PS) within a theta solvent (cyclohexane-CH), at the theta temperature (actually room temperature).

TiO_2 nanoparticles and PANI powder have been added to this solution. In order to obtain a homogeneous distribution of nanoparticles and of PANI particles, the mixture PANI-PS-TiO_2-CH has been sonicated using a Hielscher high power sonicator operating at 1 KW for about 90 minutes. Composites loaded with various amounts of nanofiller, ranging from 0 to 20wt%. TiO_2 and 0 to 20wt%. PANI have been obtained.

The effect of the nanofiller on the glass transition temperature of the polymeric matrix is rather complex, shifts towards lower and higher temperature being reported. While the actual glass transition temperature is extremely important for the final physical properties and applications of the nanocomposites, the shift of the glass transition temperature is not always a correlated in a simple manner to the existence and the size of polymer-nanofiller composite.

The present study is focused on the thermal features of ternary PS-PANI–TiO_2 nanocomposites. The polymeric matrix is completely amorphous –a feature that simplifies the experimental study as melting and crystallization effects are not involved. TiO_2 nanoparticles are among the smallest nanoparticles available commercially. This allows for huge areas of contact between the nanofiller and the polymeric matrix and reduces the thermal conductivity of TiO_2.

The thermal degradation of PS is well known. The depolymerization process is well understood; consequently, the effect of the nanometer-sized filler on the thermal stability of the polymeric matrix can be easily assessed. Both PANI and TiO_2 nanoparticles have a good thermal and thermo oxidative stability and will not contribute to the evolution of the mass of the sample as the temperature is increased. Hence the temperature dependence of the mass of the sample in nitrogen will be controlled by the degradation of PS.

4.3 Experimental Data

Figure 4.1 is the TGA result for PS-PANI composite. The TGA measurement is The TGA measurement is from room temperature to 700°C by 10°C heating rate. From the result we can see that the degradation temperature, T_0, not change very much, just about 5°C, when the concentration of PANI increase from 0% to 10%. Compare with the large change by TiO_2 nanofillers, this demonstrate that there is no interface formed between the PS matrix and PANI fillers.

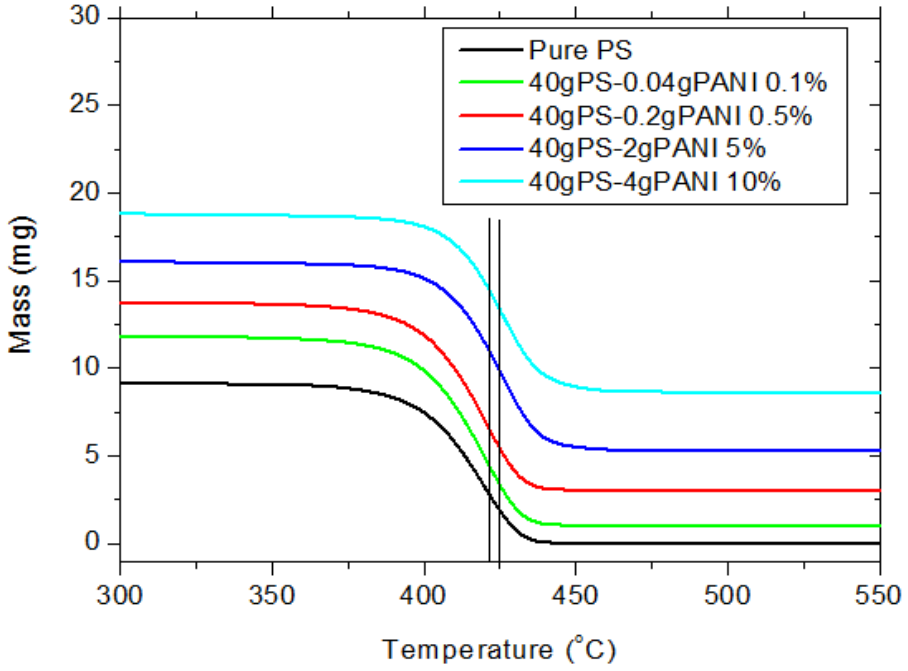

Figure 4.1 TGA results of PS-PANI composite with different PANI concentration.

Figure 4.2 is the TGA result for PS-PANI-TiO_2 nanocomposite. Since the result from TGA for PS-PANI shows that there is no interface formed between the PS matrix and PANI fillers, we fixed the amount of PANI and increase the amount of TiO_2 nanoparticles, in order to see the influence of the two fillers in this ternary system. And the result is impressive. From Figure 4, we see that the T_0, for this ternary system is increasing when the amount of TiO_2 is increasing and the range of increase is also about 25°C. This demonstrates that there is no influence between TiO_2 nanofillers and PANI fillers. So we can get the structure of these PS-PANI-TiO_2 ternary systems as shows in Figure 4.3.

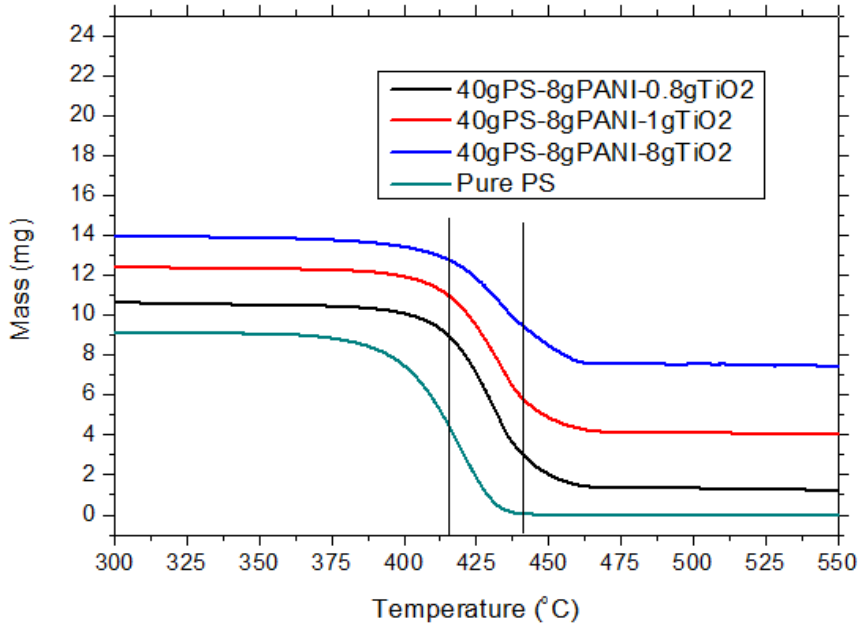

Figure 4.2 The TGA results of PS-PANI-TiO_2 nanocomposites

Figure 4.3 shows the Structure of PS-PANI-TiO_2 nanocomposite. The gray sphere represents the TiO_2 nanoparticle, the pink background is represent the PS matrix, the blue wire represent the PS chains, and the red wire represent the PANI molecular chain. We can see that the PANI does not have much interaction with the matrix and nanoparticles. Also we can see there are some PS chains which attach to the nanoparticles and form an interface between the TiO_2 nanoparticle and the PS matrix, we believe these chains have more thermal stability than the PS chains which is not attached to the nanoparticles. , this can explain why the degradation temperature is increasing when the composition of TiO_2 nanoparticles increasing. Because the more nanoparticles mean more area of interface, this will increase the thermal stability of the whole system. But why when the concentration of TiO_2 reach 11% the further increase of the concentration of nanoparticles does not resulted in a further increase of the degradation temperature. We guess this is because of the aggregation of nanoparticles. We believe there must be a critical concentration which is around 11% and when the concentration goes above it, the nanoparticles begin to aggregate into clusters and that is the limit the sonicator can disperse the nanofillers evenly into the matrix. Since the surface area of clusters is much less than the surface area of same amount of nanoparticles which is isolated. So the degradation temperature will not change very much for the further increase of the nanoparticles above the critical concentration.

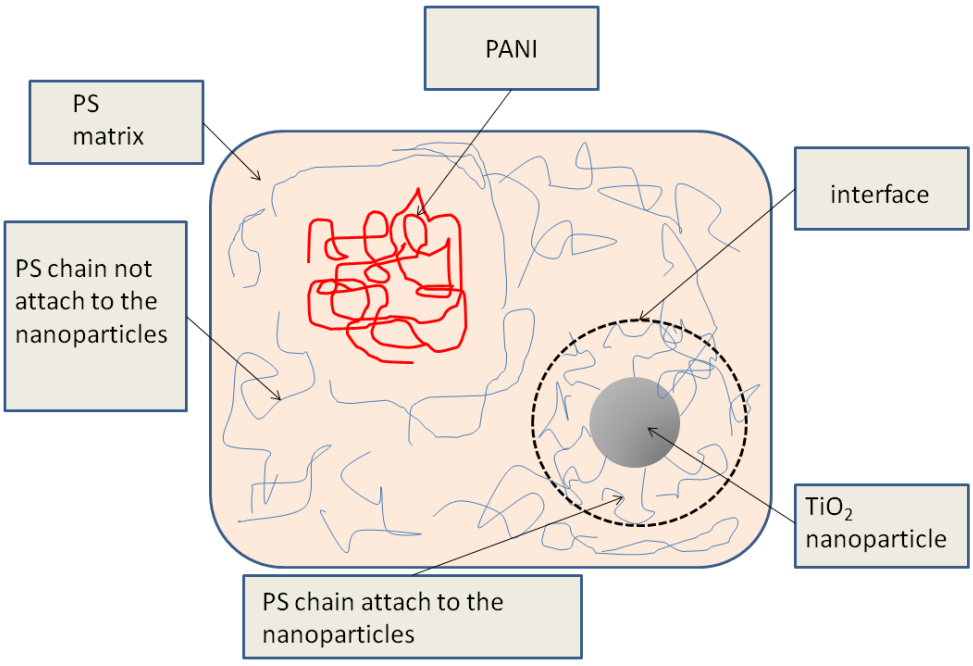

Figure 4.3 The Structure of PS-PANI-TiO_2 nanocomposite

4.4 Conclusion

The PS-PANI, PS-TiO_2, and PS-PANI-TiO_2 nanocomposites were successfully synthesized by solution blending method. The TGA results show the structure of these systems. Unlike the PS-TiO_2 system, PANI did not interact much with PS matrix, which means that there are probably weak interactions between PANI particle and PS matrix. These interactions were assigned to the electrical and thermal conductivity of PANI. So we can conclude that the significant shift of the degradation temperature of PS-PANI-TiO_2 system is mainly caused by the interface between TiO_2 and PS matrix.

CHAPTER 5 POLYETHYLENE OXIDE-TIO_2 NANOCOMPOSITES

Polymer-based nanocomposites have been prepared by the dispersion of nanometer-sized TiO_2 particles within polyethylene oxide. The effect of the interactions between TiO_2 nanoparticles and macromolecular chains were investigated by differential scanning calorimetry. A weak decrease of the crystallization temperature upon the addition of TiO_2 nanoparticles was noticed.

5.1 Introduction

The dispersion of nanoparticles within polymeric matrices results in the appearance of an interface between the nanoparticles and macromolecular chains. Due to the huge surface area of nanoparticles, the enhanced physical properties of the interphase start to control the behavior of polymer-based nanocomposites. The present study focuses on phase transitions phenomena (crystallization, melting, and glass transition) in polyethylene oxide (PEO) and polyethylene oxide - TiO_2 nanocomposites (PEO-TiO_2).

Polythylene oxide or polyoxyethylene is a synthetic polymer (linear homopolymer of ethylene oxide) with an average molecular weight (MW) equal or larger than 100,000. Shorter macromolecular chains are known as polyethylene glycol (PEG). Both polymers (PEO and PEG) are water soluble and nontoxic.

In order to exploit the new physical properties triggered by the huge surface area of nanoparticles it is necessary to achieve a uniform dispersion of nanoparticles. This is

not trivial as nanoparticles have the tendency to agglomerate. Here the novel synthesis of a polymer-nanofiller nanocomposite obtained by using high pressure homogenization in the fluid phase is reported.

The sonication method cannot disperse the nanoparticles into the polymer matrix very well without present of surfactant. In order to disperse particles into matrix evenly, there are 3 methods: magnetic stirring, sonication, and high pressure homogenizer. Magnetic stirring is the most common and cheapest method in mixing, but it cannot disperse the nanosized filler evenly into the liquid. Sonication is the most popular method to disperse nanoparticles into liquid, but the result in this case it is not sufficient to meet the goal. Before turning to the surface modification of the nanoparticles or in-situ method to synthesis the nanocomposites, there is one choice available which is high pressure homogenization method. The high pressure method which is called Dynamic High Pressure Homogenization Technology is based on the use of pressure on liquids to subdivide particles or droplets insoluble in fluids into the smallest possible particle sizes and create a stable dispersion ideal for further processing. The very narrow gap which the product is passing thorough under high pressure is able to break macro size dispersed clusters down to the order of magnitude of micrometers or nanometers particles. The reported results show that for homogenize purpose the efficiency of high pressure is higher than sonication and stirring. Yujin Hwang et al have compared the average size of clusters in the fluids after high pressure, sonication, stir respectively. Their research shows that the high pressure homogenization is the most efficiency in these three methods[76]. Also Juliane Floury et al[77], and Andreas Hakansson, et al[78], shows the mechanism and create a mathematical model of the high pressure homogenization. Here

we are trying to use the high pressure homogenization method to disperse our TiO_2 nanoparticles into polymer matrix. Since our high pressure homogenizer can only handle water dissolvable polymer, so we decide to use poly(ethylene oxide) (PEO) as polymer matrix. The purpose is only to see how well the high pressure homogenizer can get in dispersion of TiO_2 nanoparticles into the PEO matrix.

5.2 Methodology

Almost cubic TiO_2 nanoparticles (anatase) with a size of about 13 nm have been purchased from Nanostructured and Amorphous Materials, Inc. PEO has been purchased from Sigma Aldrich. PEO is an amorphous-crystalline polymer. PEO-TiO_2 nanocomposites were processed by high pressure homogenization using a Nano DeBee equipment (produced by BEE International: http://www.beei.com/products_lab.html), at room temperature.

The water dissolvable polymer, Poly(ethylene oxide), with M_w=900,000 g/mol was bought form Sigma-Aldrich. The synthesis procedure is: 1. Dissolve 2g PEO into 200ml or 100ml distilled water, the viscosity of the matrix solution can be adjusted by changing the amount of distilled water; 2. Stir over night at room temperature until the PEO has totally dissolved; 3. Add certain amount of TiO_2 nanoparticles in the polymer matrix solution and stir for another 2 hours at room temperature to get an unstable suspension; 4. Feed the unstable suspension into high pressure homogenizer (Nano DeBEE 45 homogenizer) for 3 cycles at 15,000 psi, then we can get stable suspension; 5.

Pour the stable suspension on the glass slides and dry it in the air for several days then we can get PEO-TiO_2 nanocomposite films. SEM (LEO 1530VP FESEM) was used to measure the average cluster size of TiO_2 in the PEO-TiO_2 nanocomposites. DSC (Q1000 DSC TA Instruments) was used to do the thermal analysis for some of my samples. The reason we use different amount of distilled water to dissolve the PEO is to see the influence of viscosity of PEO matrix solution to the cluster size and the dispersion of the TiO_2 nanoparticles.

5.3 Experimental Data

Figure 5.1 shows the SEM image of PEO-TiO_2 nanocomposite in different concentration of TiO_2 nanoparticles synthesized by 200ml distilled water dissolved PEO matrix. Figure 5.1(a) is pure PEO without TiO_2 nanoparticles, we can see the surface is very clean and smooth. Figure 5.1(b) to (e) shows that the concentration of TiO_2 below 20wt%, the image shows that the cluster size is up to 1um to 2 um, but the clusters disperse evenly in the PEO matrix. Figure 5.1(f) to (i) shows that the concentration of TiO_2 form 20wt% to 40wt%, we can see the cluster size is suddenly increase to very large size, and also the dispersion is not good enough.

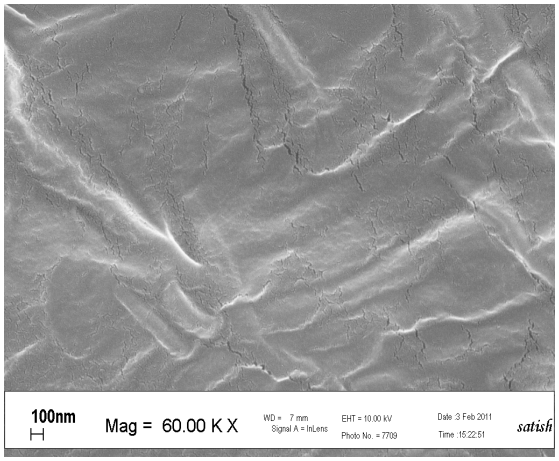

(a) PEO-0wt%TiO_2

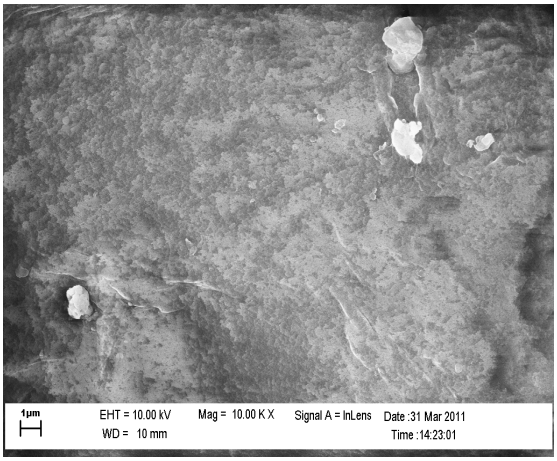

(b) PEO-1wt%TiO_2

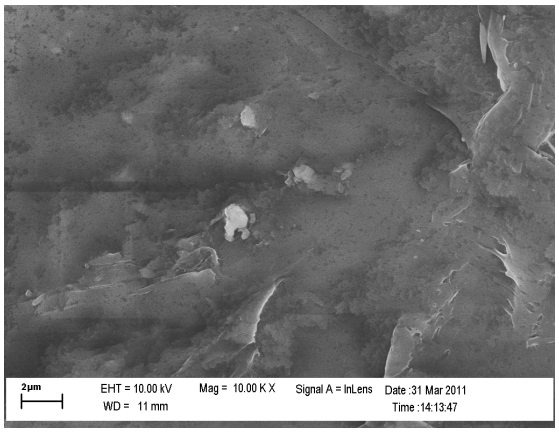

(c) PEO-5wt%TiO_2

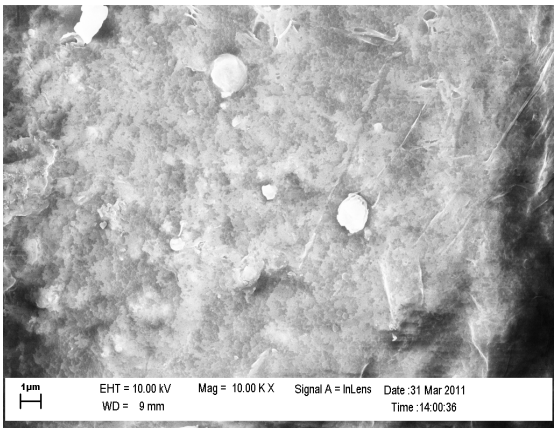

(d) PEO-10wt%TiO_2

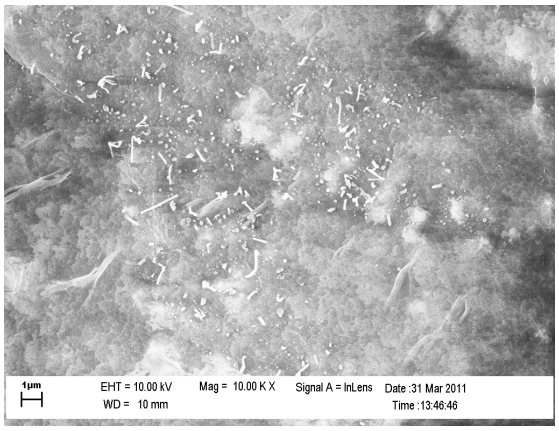

(e) PEO-15wt%TiO_2

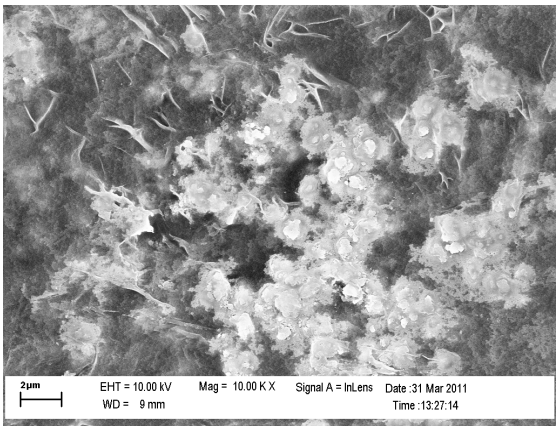

(f) PEO-20wt%TiO_2

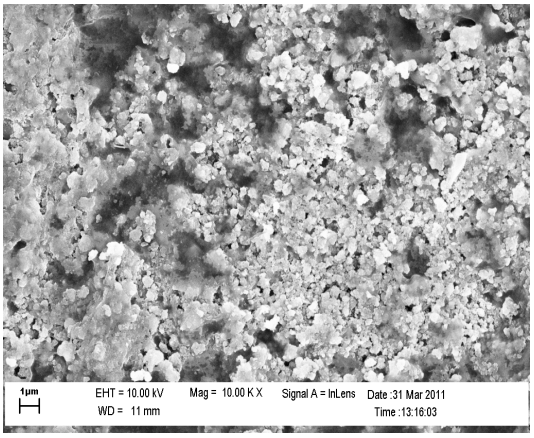

(g) PEO-25wt%TiO_2

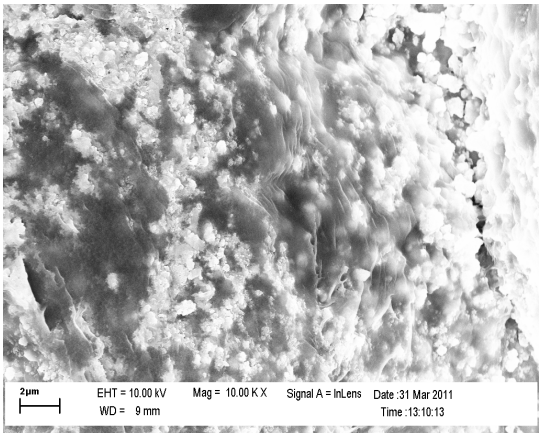

(h) PEO-30wt%TiO_2

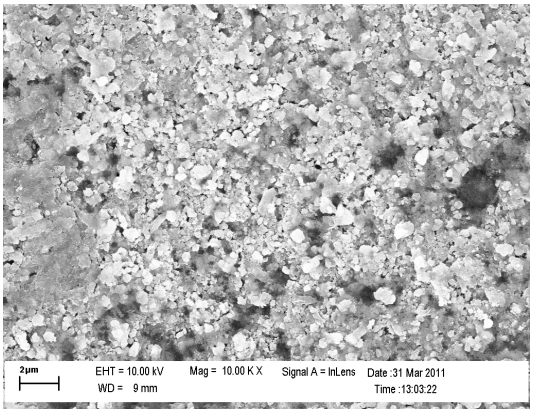

(i) PEO-40wt%TiO_2

Figure 5.1 SEM images for PEO with 0wt%-40wt% TiO_2 nanoparticles, respectively, prepared by 200ml DI water dissolved PEO matrix solution.

Figure 5.2 shows the SEM image of PEO-TiO_2 nanocomposite in different concentration of TiO_2 nanoparticles synthesized by 100ml distilled water dissolved PEO matrix. Since the solvent is cut half but the solute remains the same, the viscosity of the polymer matrix solution is significantly increased. Figure 5.2 (b) to (f) shows the SEM image of PEO-TiO_2 nanocomposite with the concentration of TiO_2 nanoparticles below 25%, the image reveals that the cluster size is around 100nm and the dispersion is very good. But the cluster size is suddenly increased into micron size when the concentration of TiO_2 reached 25wt% and also the dispersion is going bad, showing in Figure 5.2(g) to (i), but it is still better than the results from the same concentration of TiO_2 synthesized by less viscose polymer matrix solution.

By comparing of these two groups of samples, we can conclude that the viscosity of the polymer matrix solution has significantly influence on the final cluster size and dispersion of the nanofillers, we successfully maintain the clusters within the nano scale with the concentration of TiO_2 up to 30wt%. This demonstrates that the high pressure method is more efficient than sonication method (reached up to 11wt% TiO_2 in PS matrix). From the result above, two solutions can be proposed to further control the cluster size and dispersion of nanofillers. The first one is to use the oven to speed up the drying process which can “freeze” the nanofiller before they aggregate in large size. The second one is to increase the viscosity to a higher level. As a result a larger sheer force of the fluid can be generated to break up the local aggregation.

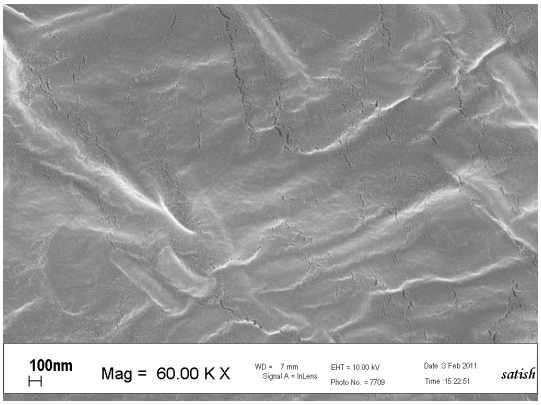

(a) PEO-0wt%TiO_2

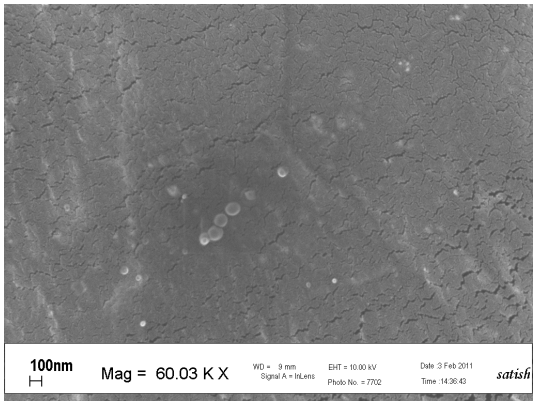

(b) PEO-1wt%TiO_2

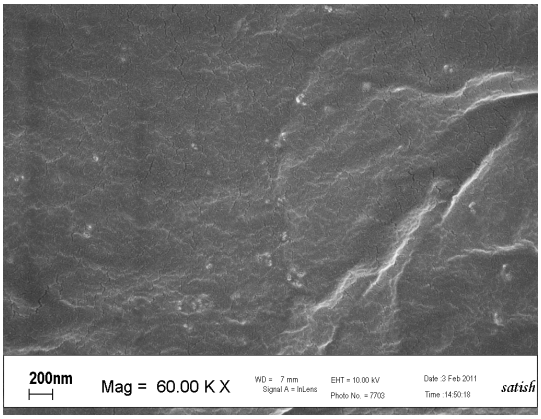

(c) PEO-5wt%TiO_2

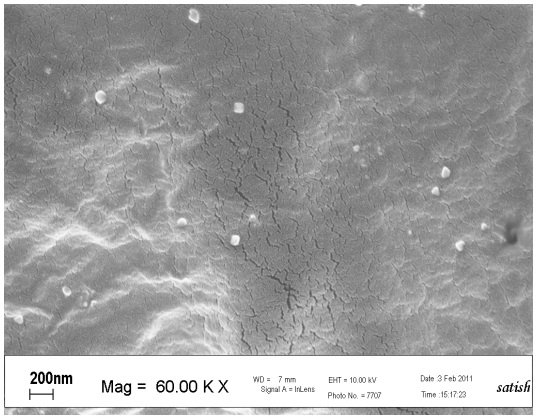

(d) PEO-10wt%TiO_2

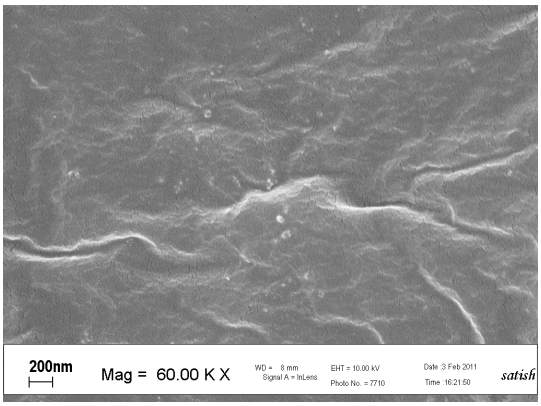

(e) PEO-15wt%TiO_2

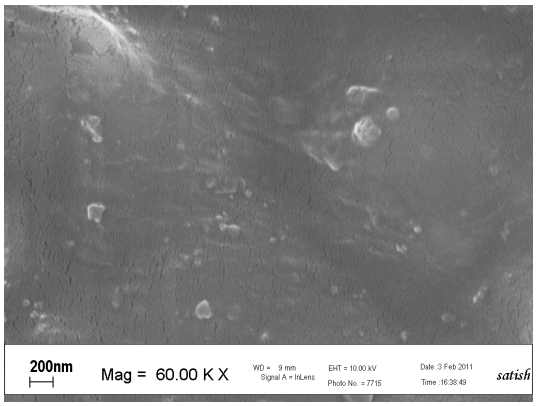

(f) PEO-20wt%TiO_2

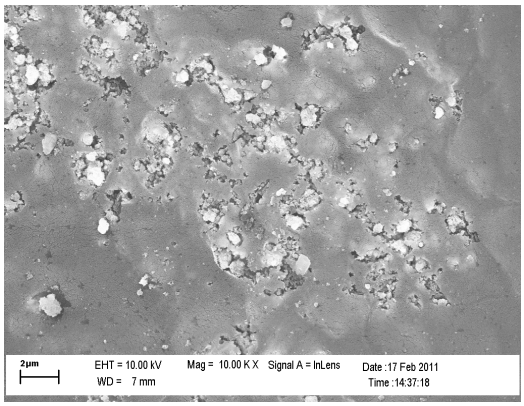

(g) PEO-25wt%TiO_2

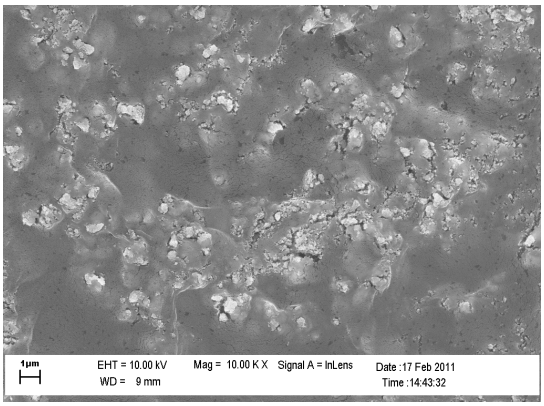

(h) PEO-30wt%TiO_2

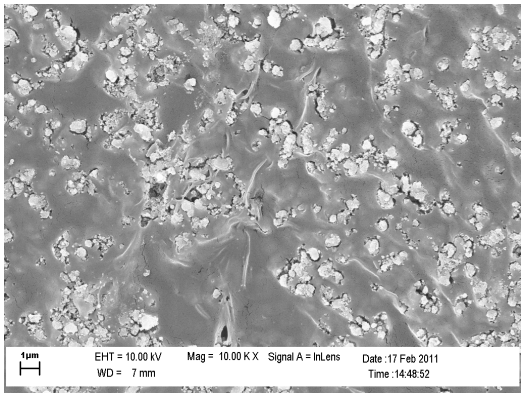

(i) PEO-40wt%TiO_2

Figure 5.2 SEM images for PEO with 0wt%-40wt% TiO_2 nanoparticles, respectively, prepared by 100ml DI water dissolved PEO matrix solution.

Isothermal scans have been performed at various heating rates ranging from 5 ^{o}C/min to 25 ^{o}C/min in the temperature range -70 ^{o}C to 150 ^{o}C. These investigations aimed at the estimation of the glass and melting (during the heating cycle) and crystallization and glass (during the cooling cycle) temperatures as a function of heating rate and TiO_2 concentration.

First cycle (heating from room temperature to 150^{o}C, annealing at 150 ^{o}C for 10 minutes, cooling from 150 ^{o}C to -70 ^{o}C, equilibration at -70 ^{o}C, heating from -70 ^{o}C to 150 ^{o}C and annealing for 10 minutes at 150 ^{o}C) has been discarded for all heating rates and samples as it was affected by the thermal history of the samples. It was checked for all heating rates and samples that the second and third cycles are identical. The data obtained during the second cycle have been investigated in detail (see Figure 5.3).

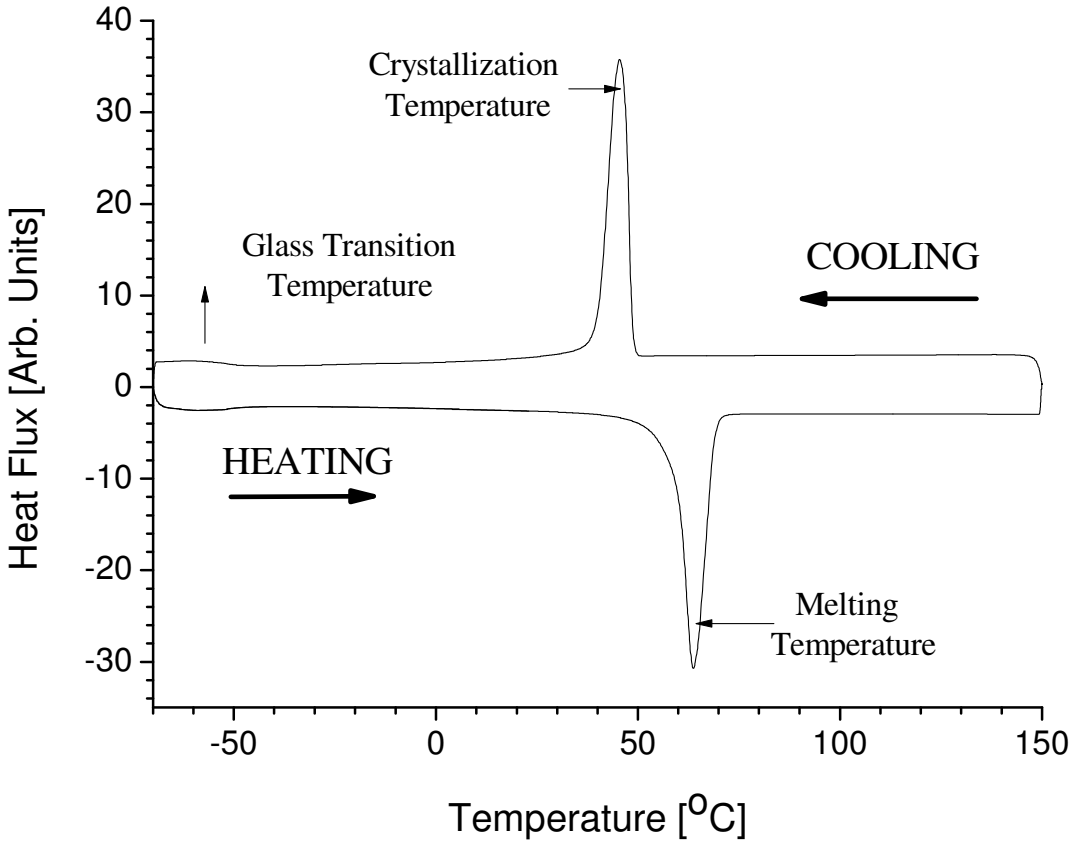

Figure 1.

Figure 5.3 DSC heating/cooling cycle of pristine PEO (second cycle) recorded at a heating/cooling rate of 5°C/m

The peaks of the crystallization, melting, a glass transition temperature were affected by the loading with TiO_2 and heating rate. Figure 5.4 shows the effect of the heating rate on the crystallization peaks for several heating rates.

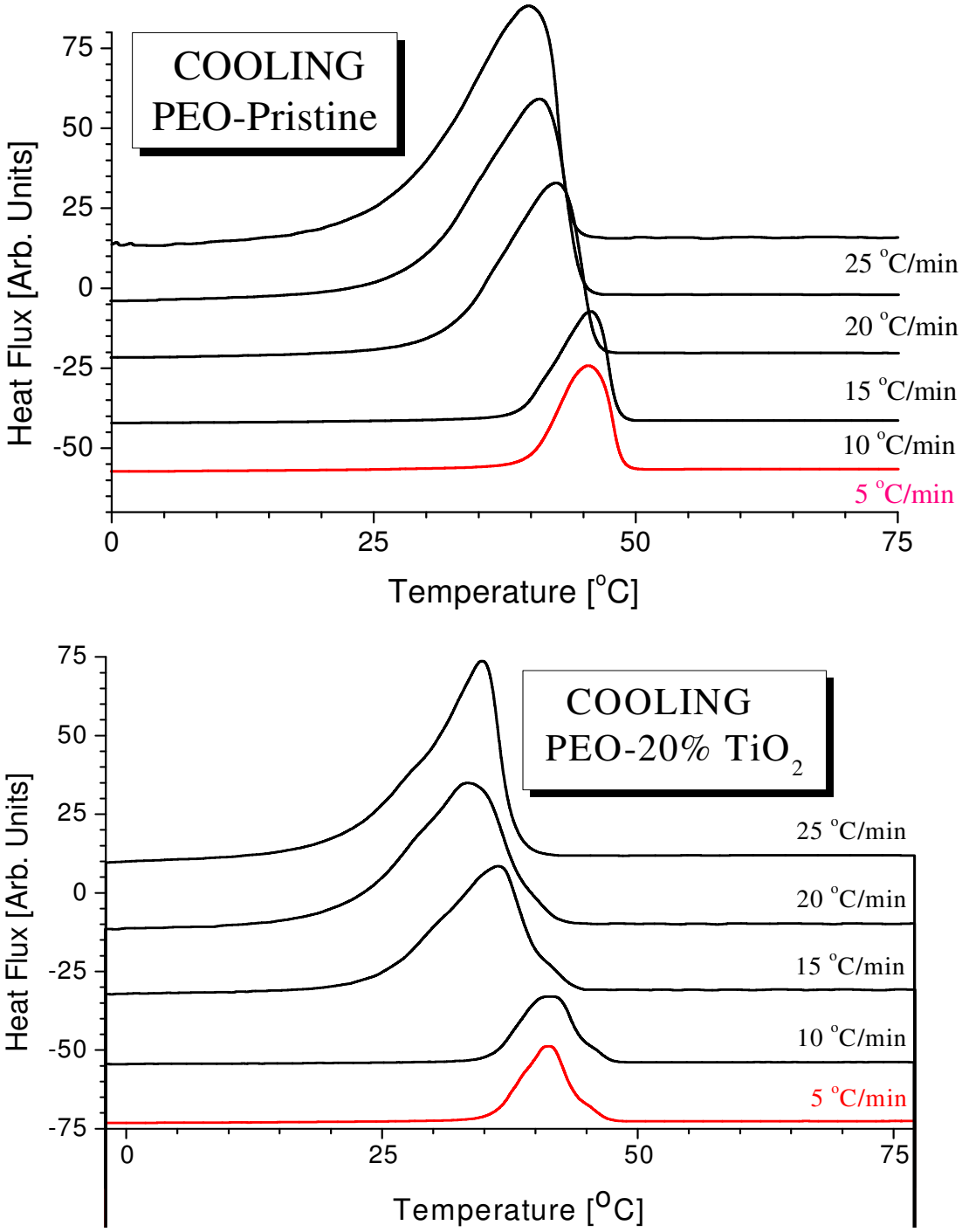

Figure 5.4 The effect of the cooling rate on the crystallization process in PEO and PEO-20% TiO_2.

Figure 5.5 and Figure 5.6 shows the DSC result for different cooling rate. We can see that excepting the anomaly at very low concentration of TiO_2, the dispersion of TiO_2 nanoparticles drops the crystallization temperature of PEO. This supports the data on the dependence of the glass transition temperature on the loading with TiO_2 and reflects a poor interface between TiO_2 nanoparticles and PEO. A higher cooling rate shifts the crystallization temperatures to lower value which is as expected. Potentially, these pair of materials behaves as expected. We will need to focus on the addition of the conducting polymer (polyaniline) to this system. Figure 5.5 shows the DSC result for heating rate at 5°C/min. From the result, we can get the same conclusion as above. Excepting the anomaly at very low concentration of TiO_2, the dispersion of TiO_2 nanoparticles drops the crystallization temperature of PEO. So a higher heating rate shifts the melting temperatures to higher value.

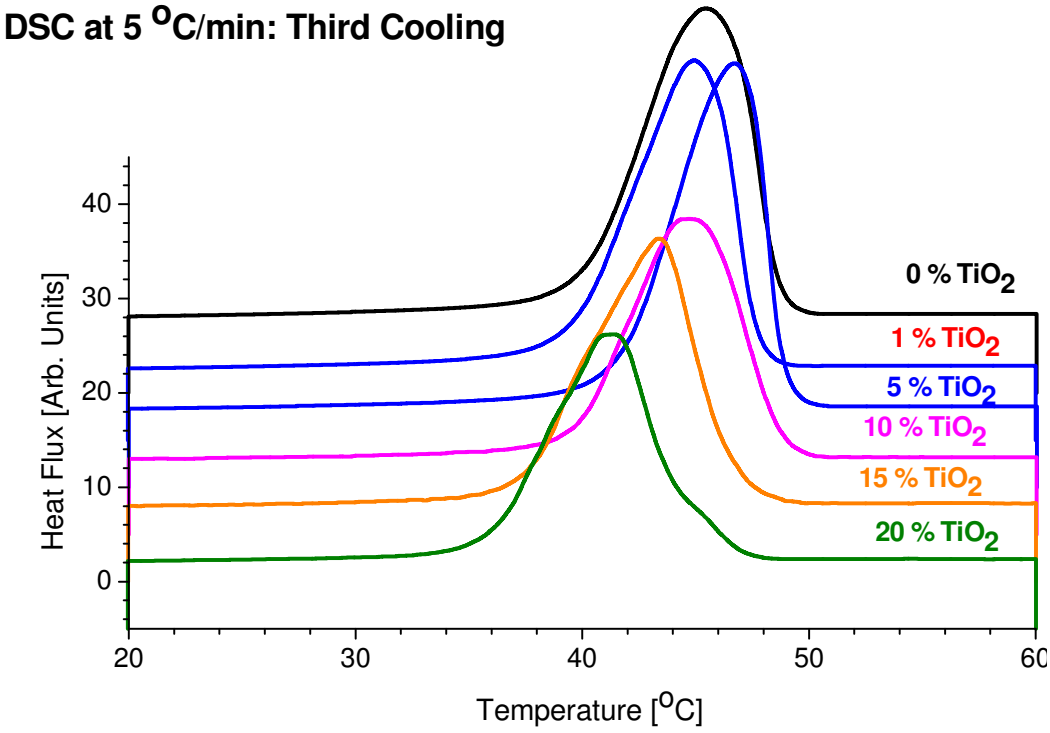

Figure 5.5 DSC result for PEO-TiO_2 nanocomposite at 5 °C/min cooling rate

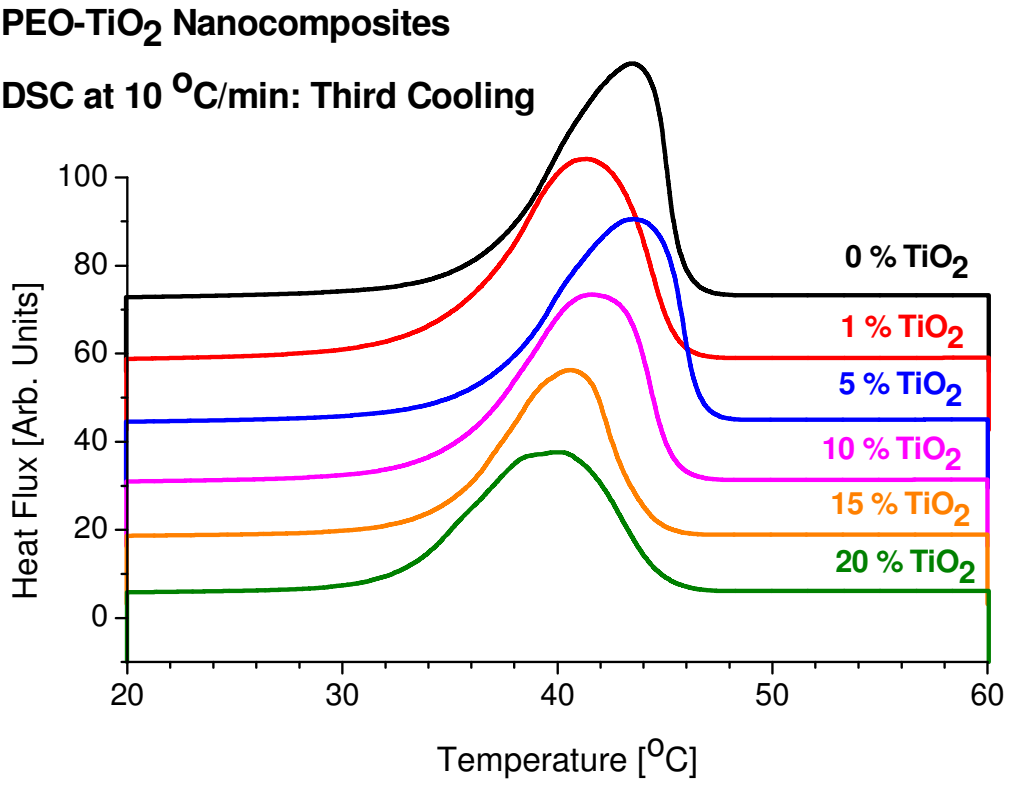

Figure 5.6 DSC result for PEO-TiO_2 nanocomposite at 10 °C/min cooling rate

The effect of the heating/cooling rate on the crystallization and melting temperature for PEO-TiO_2 nanocomposites is shown in Figure 5.7. It is observed that the crystallization temperature decreases as the concentration of TiO_2 is increased for all heating rates. Typically, lowest cooling rates result in highest crystallization temperature. The melting temperature dependence shows the same general trend with a remarkable exception between PEO and PEO 1% TiO_2.

PEO-TiO_2 nanocomposites were prepared. The observed shift of the glass, melting, and crystallization temperature due to the addition of the nanofiller confirm the formation of an interface between polymer and filler.

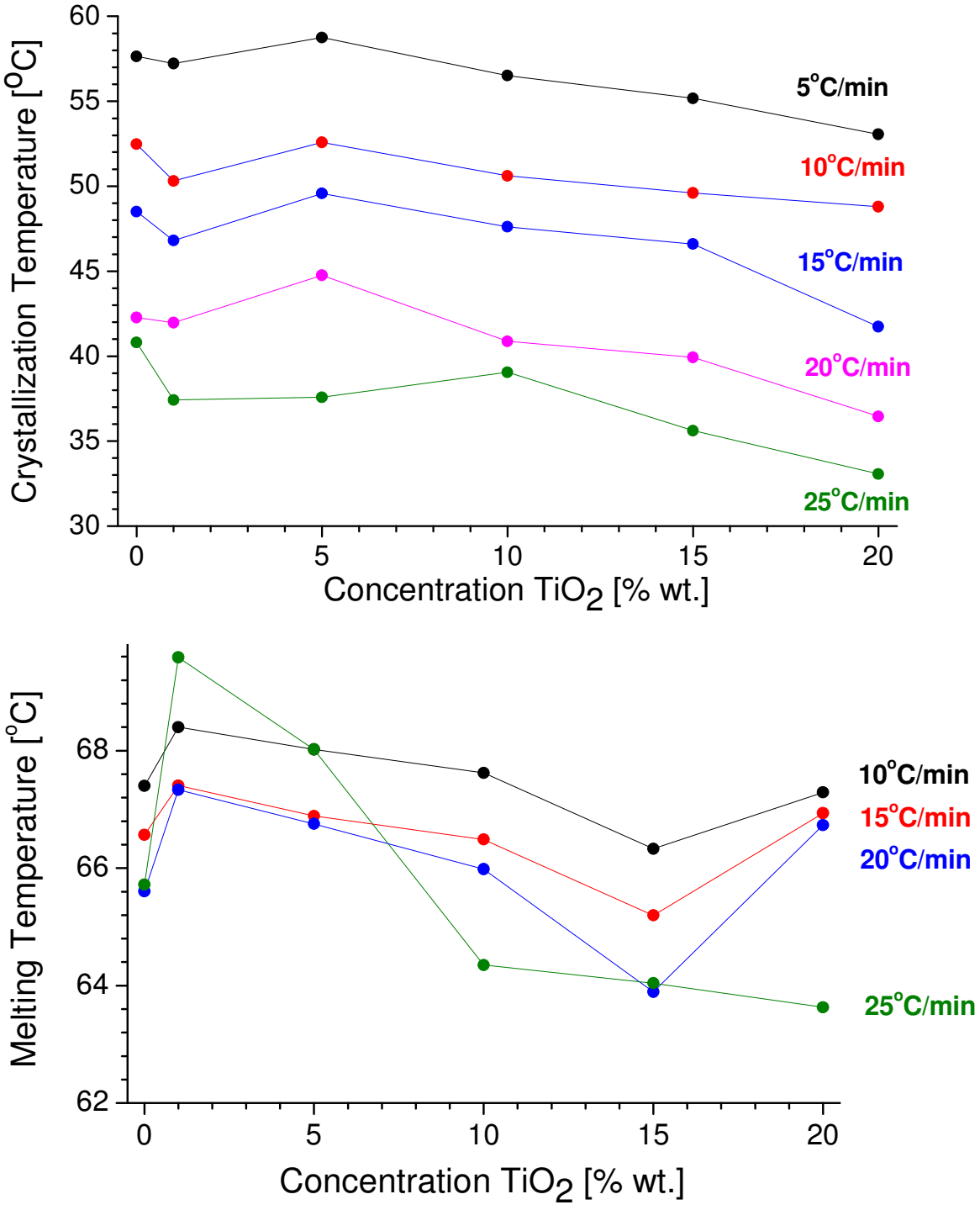

Figure 5.7 The effect of the cooling rate on the crystallization process in PEO and PEO-20% TiO_2

5.4 Conclusion

From this research, we find out that the viscosity strongly influence the dispersion of nanofillers. We can improve the dispersion of TiO_2 nanoparticles in the PEO matrix by increasing the viscosity of polymer matrix solution, and a weak drop in the glass transition (T_g) of the polymeric matrix upon the loading with TiO_2 nanoparticles. The result also reveals that excepting the anomaly at very low concentration of TiO_2, the dispersion of TiO_2 nanoparticles drops the melting temperature and the crystallization temperature of PEO. The anomaly may be caused by the dispersion of the TiO_2.

CHAPTER 6 VINYL ACETATE-ETHYLENE AND CARBON NANOTUBE COMPOSITES

6.1 Structure Introduction

6.1.1 Single Wall Carbon Nanotube

The single wall carbon nanotube has a carrier mobility of~$10{,}000 cm^2 V^{-1} s^{-1}$ [79], which is much better than silicon's~$1{,}000 cm^2 V^{-1} s^{-1}$ [80]. They can also carry an electrical current at the density of ~$4 \times 10^9 A cm^{-2}$, which is three orders of magnitude higher than a typical metal, such as copper or aluminum[81]. So we believe the combination of carbon nanotube and conducting polymer can lead to a promising conducting composite material.

The carbon nanotube we use is purchased from Cheap Tubes Inc, Figure 6.1. The 60wt% purity nanotube is used to optimize the processing condition. Once the best recipe is found out, the 90wt% purity nanotube can be used to reach the best material performance. The detailed specification of nanotube has been listed in Table 6.1. The aspect ratio (length over outer diameter) is more than 2500.

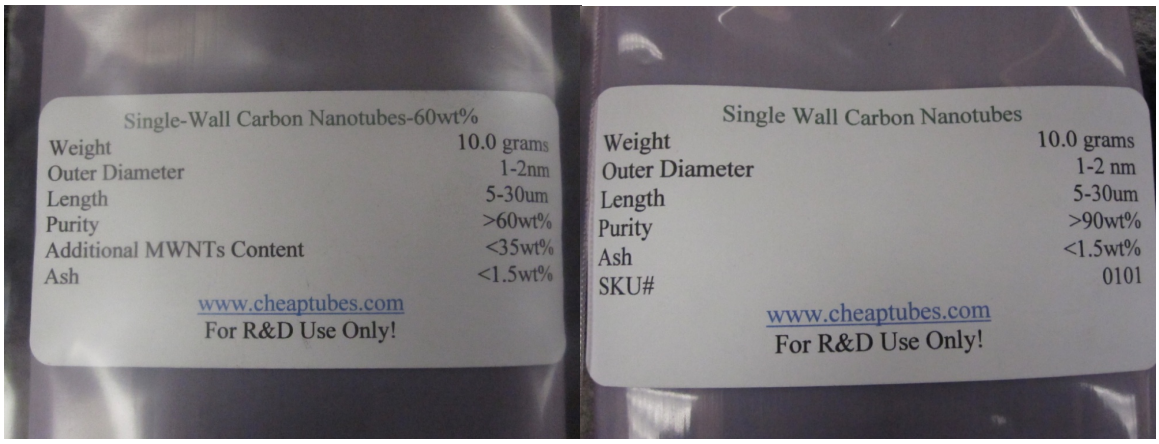

Figure 6.1 Single wall carbon nanotube from Cheap Tubes Inc.

TEM image	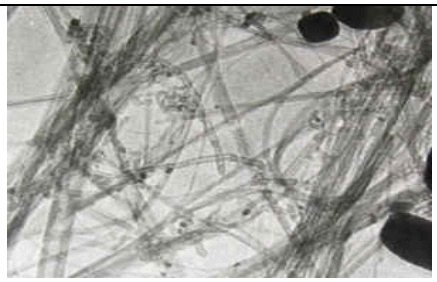	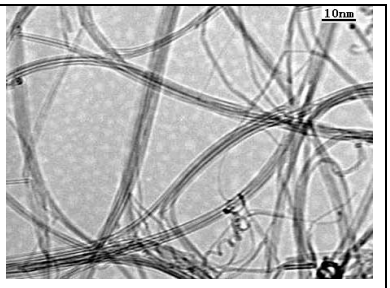
Outer Diameter	1-2nm	1-2nm
Inside Diameter	0.8-1.6nm	0.8-1.6nm
Ash	<3.0 wt%	<1.5 wt%
Purity	>60 wt%	>90 wt%
Additional MWNT content	>30wt%	>5wt%
Amorphous Carbon Content	<5wt%	<3wt%
Length	5-30um	5-30um
Specific Surface Area	407 m^2/g	407 m^2/g
Electrical Conductivity	>100 S/cm	>100 S/cm
Bulk density	0.14 g/cm^3	0.14 g/cm^3
True density	~2.1 g/cm^3	~2.1 g/cm^3

Table 6.1 Single wall carbon nanotube specifications

6.1.2 Vinyl Acetate-ethylene Copolymer

The polymer (Vinnapas@ 401) we use as matrix is a poly(vinyl alcohol) stabilized vinyl acetate-ethylene copolymer dispersion with a glass transition temperature (T_g) of -15 °C. The low T_g helps to continues to form a film at lower temperatures and can be used in the laminating of cold substrates while still maintaining adhesion and heat resistance. The higher level of ethylene in the polymer acts as an internal plasticizer which provides flexibility and reduces or eliminates the need for plasticizer in many applications. The product specification data is showed in table 2. The VAE copolymer works well with water and can form an aqueous suspension with polymer particles of 0.14-3.5um in diameter. After water evaporate, the VEA can become solid with excellent mechanical stability.

Solids content	54.0 - 56.0
Viscosity, Brookfield RVF#3 @20 rpm, 25°C	1300 – 2200 mPa.s
pH-Value	5.0 – 6.5
VAM by Head Space GC	950 ppm max.
Protective colloid / emulsifier system	polyvinyl alcohol
Density	1,05 g/cm3
Predominant particle size	approx. 1.5 µm
Wet tack	High
Mechanical Stability	Excellent
Thickening Response	High
Freeze/Thaw Stability	Poor
Glass transition temperature DSC	approx. -15 °C
Water Resistance	Moderate
Film Clarity	Slightly Hazy
Flexibility	Excellent

Table 6.2 Vinnapas@ 401 product specifications

6.1.3 Poly(3,4-ethylenedioxythiophene)/poly(styrenesulfonate)

We use the poly(3,4-ethylenedioxythiophene)/poly(styrenesulfonate) (PEDOT:PSS) as the stabilizer in the system. The carbon nanotubes tend to tangle together. The introduction of PEDOT:PSS can modify the surface of the nanotube and help them separate from each other in the solution. PEDOT:PSS exists as a suspension containing 1.3 wt % solids (0.5 wt % PEDOT and 0.8 wt % PSS) in water. Figure 2 shows the PEDOT:PSS purchased from Sigma-Aldrich.

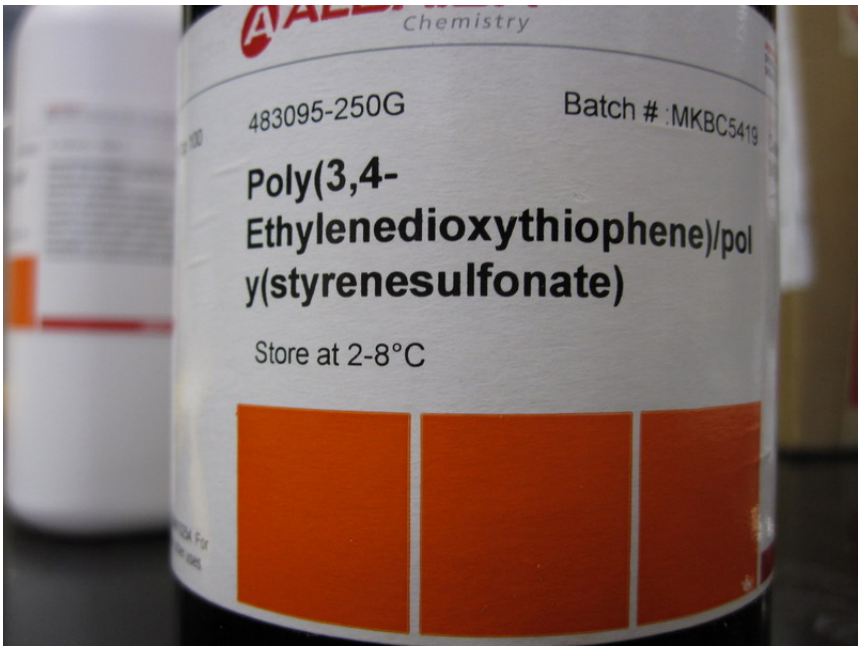

Figure 6.2 poly(3,4-ethylenedioxythiophene)/poly(styrenesulfonate) as stabilizer from Sigma-Aldrich.

6.1.4 Networks Created With a Polymer Emulsion

Figure 6.3 shows the influence of distribution of nanotube suspension in water on final material micro structure. The local tangle of nanotube in water won't form a connecting network after the water evaporates from the system. If the nanotubes are evenly distributed in the water, the polymer particle push together as the water is removed. The most connection of nanotube can be made in such a situation. The connection of nanotube plays a critical role on the electrical behavior of final material, also the on the percolation threadhold of nanotube concentration. So it becomes a key factor to avoid local tangle of nanotube when the system is in liquid status.

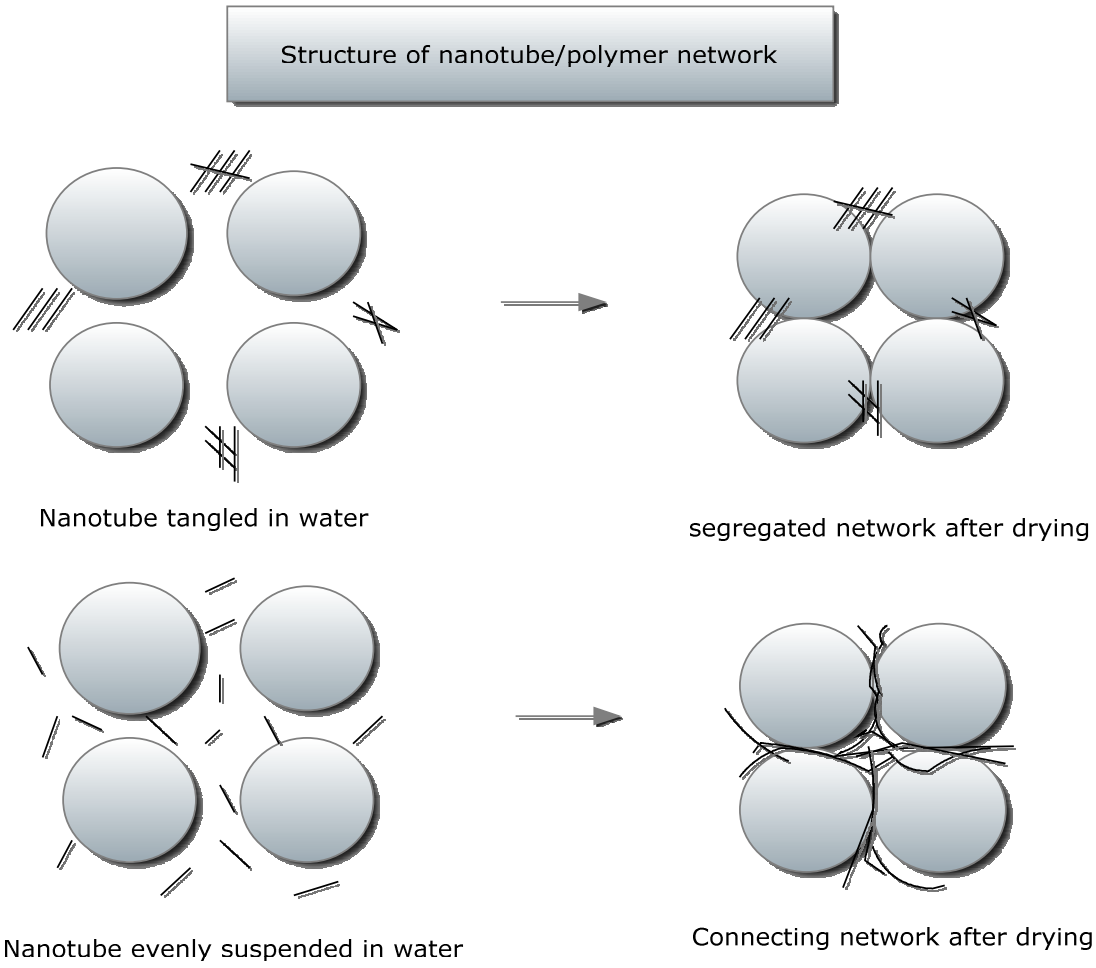

Figure 6.3 Schematic illustration of drying process for SWNT-filled polymer emulsion.

6.2 Processing Methods

6.2.1 Nanodebee

To mix the nano filler with the polymer matrix, the traditional way is sonication. However, the sonication has its own limitations: (1) it takes long time for processing. (2) It is not suitable for large volume fabrication. In most cases, the sonication method is just used in experimental lab for small scale test. Here we introduce apply the high pressure homogenizer (HPH) to solve above problems.

Figure 6.4 The Hydraulic Power Unit

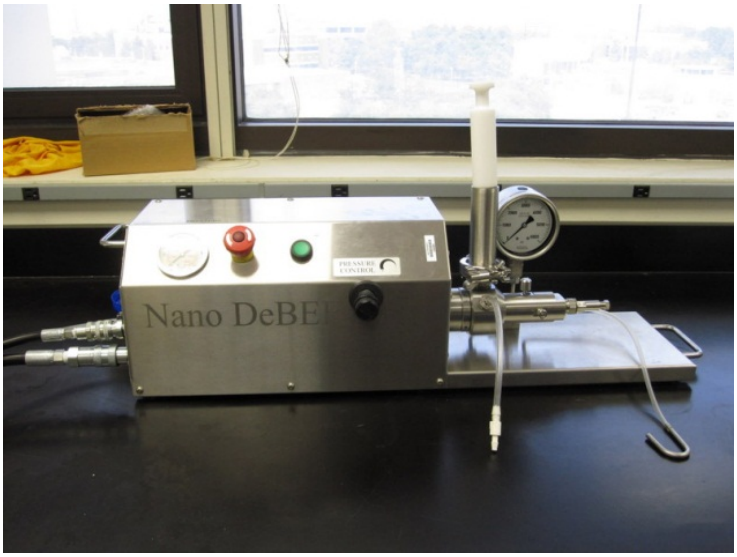

Figure 6.5 The Processing Unit

Figure 6.4 is the hydraulic power unit equiped with a standard electric motor, hydraulic pump, solenoid valves, filters and heat exchanger. It pressures oil flow from the hydraulic power unit into a hydraulic cylinder in the processing unit, causing its reciprocating action. Figure 6.5 is the processing unit. After filling the inlet reservoir with the product to be processed, the intensifier pump is turned on and starts slow cycles of suction strokes that draw fluid into the bump, and power strokes that push the product into the emulsifying cell, inside which intense and controlled forces of shear, cavitation and impact break down, mix and blend producing a thoroughly mixed product with significantly smaller particles and a uniform distribution.

Samples processed by HPH for a short time yielded similar dispersions to those obtained by sonication for prolonged time, and that the first pass through the homogenizer, which takes less than a minute, is the most significant in breaking up the

bundle. The process can be used in a continuous mode for large volumes, and is very suitable for large-scale industrial production[82].

6.2.2 Production line

PEDOT:PSS (poly(3,4-ethylenedioxythiophene) poly(styrenesulfonate)) is used as stabilizer in this system. It can modify the surface of the nanotube and make the nanotube stable in water. SWCNTs and PEDOT:PSS are mixed in deionized water and put on magnetic stirring hot plate for 15 minutes. Then VAE emulsion (vinyl acetate-ethylene copolymer) is added into the SWCNT suspension. After another 2 hours of magnetic stirring of the combination of SWCNT suspension and VAE emulsion, the suspension is processed by high pressure homogenizer to make the nanotube evenly distributed in water. Then we pour the SWCNT/VAE suspension onto glass substrate and dry it in room temperature. It takes 12 hours to remove the water and finally the solid state composite is given. The whole processing method is showed in Figure 6.6.

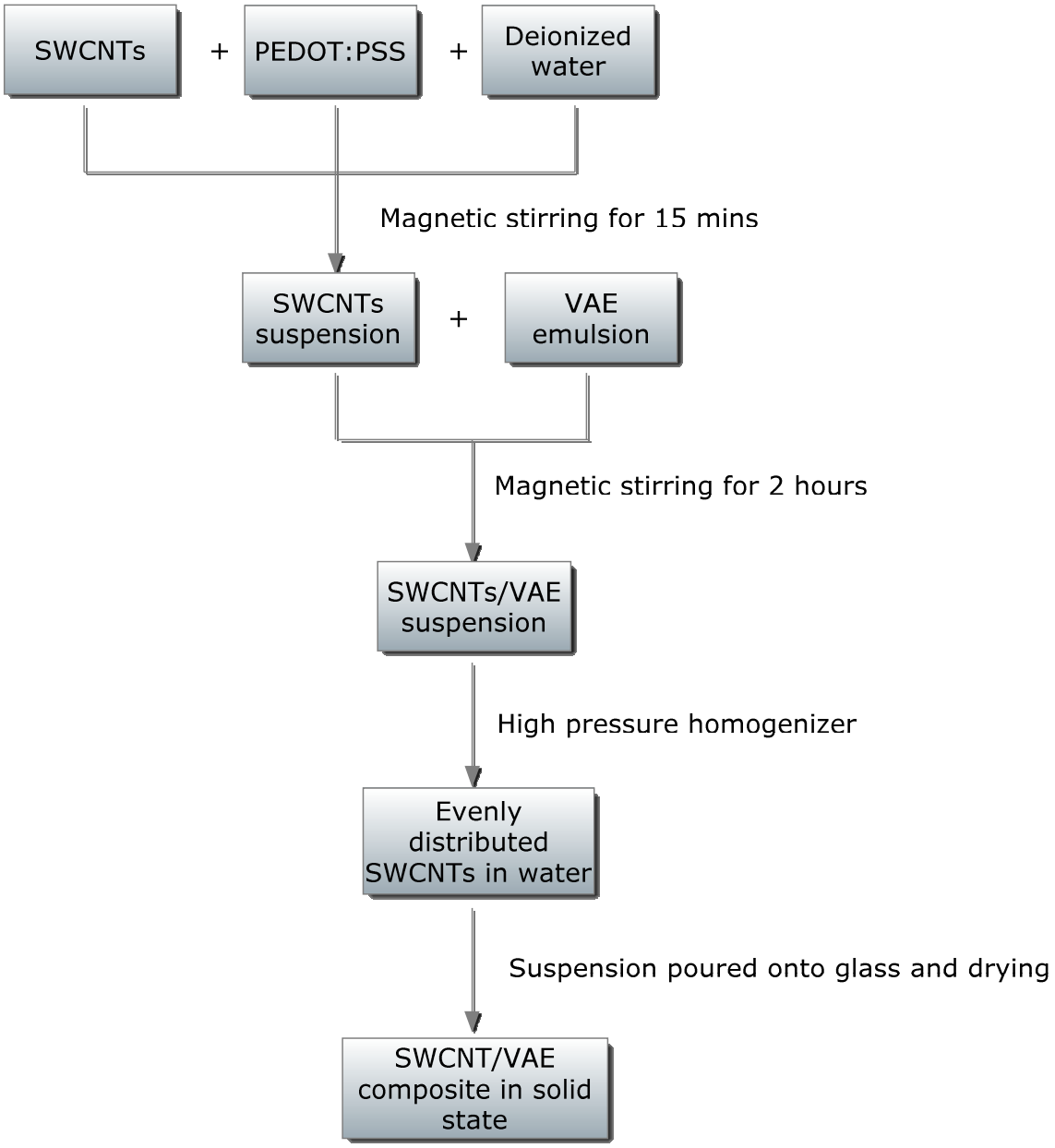

Figure 6.6 Flow chart of SWCNT/VAE production line.

6.3 Experimental data

6.3.1 Scanning Electron Microscope Characterization

Figure 6.7 shows the comparison of sonication and high pressure homogenizer. Here we used SEM to characterize the sample surface structure. Figure 6.7(a) is the sample processed by sonication. It can be seen that the sample surface is rough and the local island shape clusters appear everywhere. Figure 6.7(b) is the sample processed by Nanodebee, which has a dense and homogeneous structure. There is no local aggregation detected like the sonication sample. We can infer that the high density plays an critical role in the electrical conductivity of the material. In addition, high pressure homogenizer has huge advantage on processing efficiency. It takes 60 minutes to finish a sample showed in Figure 6.7(a). To finish a sample showed in Figure 6.7(b), it just takes 1 minute. This means a lot in large scale manufacture fabrication. The high efficiency of high pressure homogenizer can significantly reduce the processing cost.

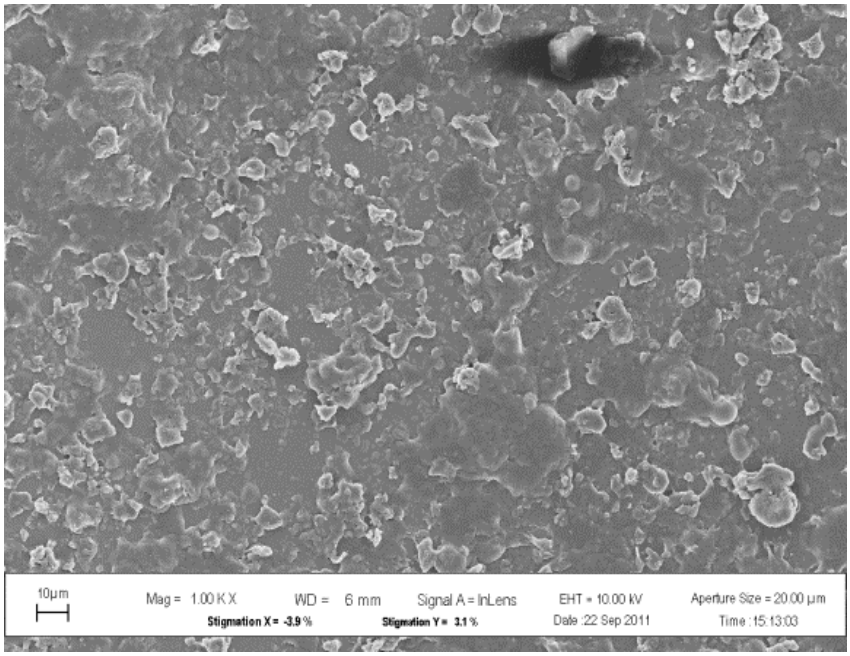

(a) SEM image of sample processed by sonication

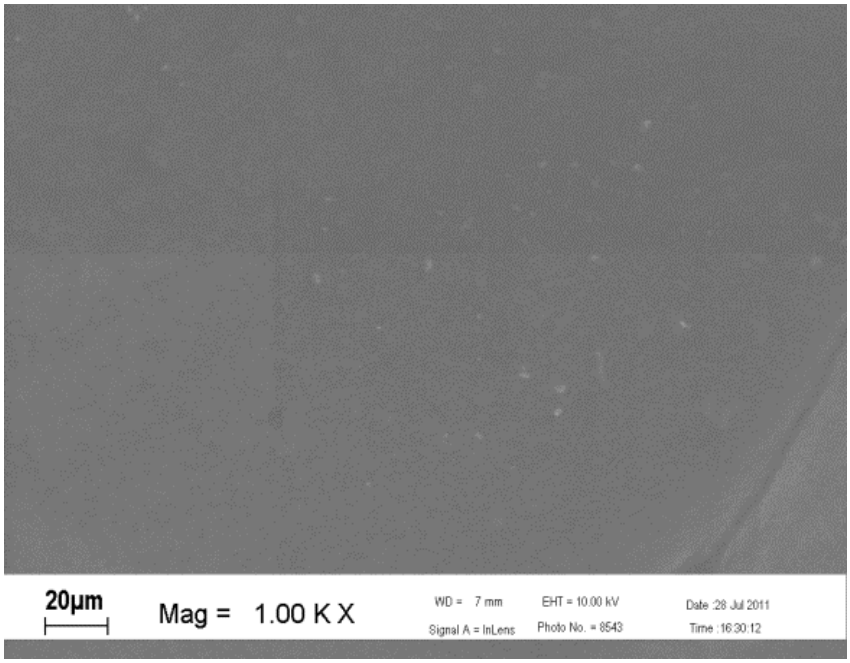

(b) SEM image of sample processed by high pressure homogenizer

Figure 6.7 The comparison on micro structure of samples processed by sonication and high pressure homogenizer

6.3.2 Raman Spectroscopy Characterization

Table 6.3 shows the 4 different concentrations of SWCNT in vinyl acetate-ethylene copolymer: 2wt%; 6wt%; 10wt%; 15wt%. We keep the same amount of water volume as 100ml for each group of sample. The mass ratio of SWCNT to PEDOT:PSS is maintained at 1:4. The volume of vinyl acetate-ethylene copolymer emulsion is adjusted according to concentration of SWCNT.

Vinapas@401 (ml)	3.87	3.27	2.84	2.43
SWCNTs(g)	0.045	0.1154	0.1667	0.2143
PEDOT:PSS(g)	0.1817	0.4615	0.6667	0.8571
Water(ml)	100	100	100	100
wt%	2%	6%	10%	15%

Table 6.3 Different concentrations of SWCNT in polymer matrix

Every band in the Raman spectrum corresponds to a specific vibrational frequency of a bond within the molecule. The vibrational frequency and hence the position of the Raman band is very sensitive to the orientation of the bands and weight of the atoms at either end of the bond.

The Raman peak at 1580cm^{-1} is radial breathing mode, also called G-band, originating from sp2 carbon. The observation of G-band in the Raman spectrum is direct evidence that single wall carbon nanotube exists in these composites.

In most cases, finite-size grapheme stacks disorder between layers and atomic defects within the layer. The disordered carbon corresponds to the D-band feature at 1300cm^{-1} ~1410cm^{-1}, as shown in Figure 6.9. The move of the D line towards lower Raman shifts reflects the pressure exerted by the polymeric matrix on nanotubes, which is strongly influenced by the amount of carbon impurities present.

The relative intensity of D to G band determines the in-plane crystallite size or the amount of disorder in the samples. The intensity of D-band, G-band and the relative value is listed in Table 6.4. We plot relative intensity as a function of SWNT concentration, as showed in Figure 6.8. The relative values are 0.67 at 15wt% and 2.88 at 2wt%. It can be seen that the less concentration of SWNT in the system, the higher level of disorder between grapheme layers, which might due to the less amount of SWNT has more interaction with the polymer matrix.

	D-band intensity	G-band intensity	D/G
VAE-15wt%SWNT	5939	9011	0.67
VAE-10wt%SWNT	11602	6852	1.69
VAE-6wt%SWNT	16333	14462	1.13
VAE-2wt%SWNT	14990	5211	2.88

Table 6.4 Relative intensity of D-band over G-band at 4 different concentration of SWNT

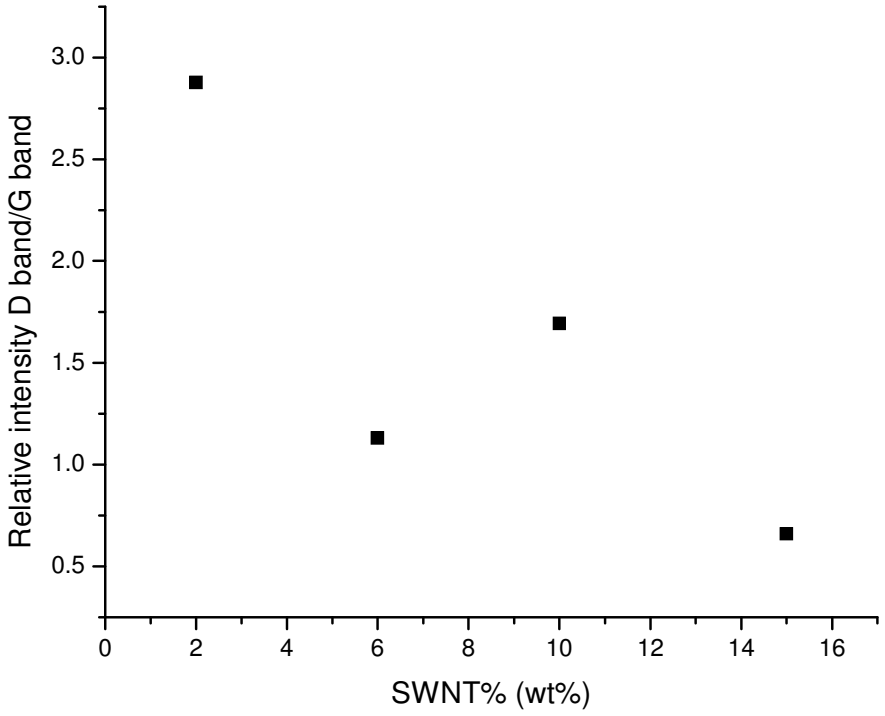

Figure 6.8 Relative D/G intensity as a function of SWNT concentration

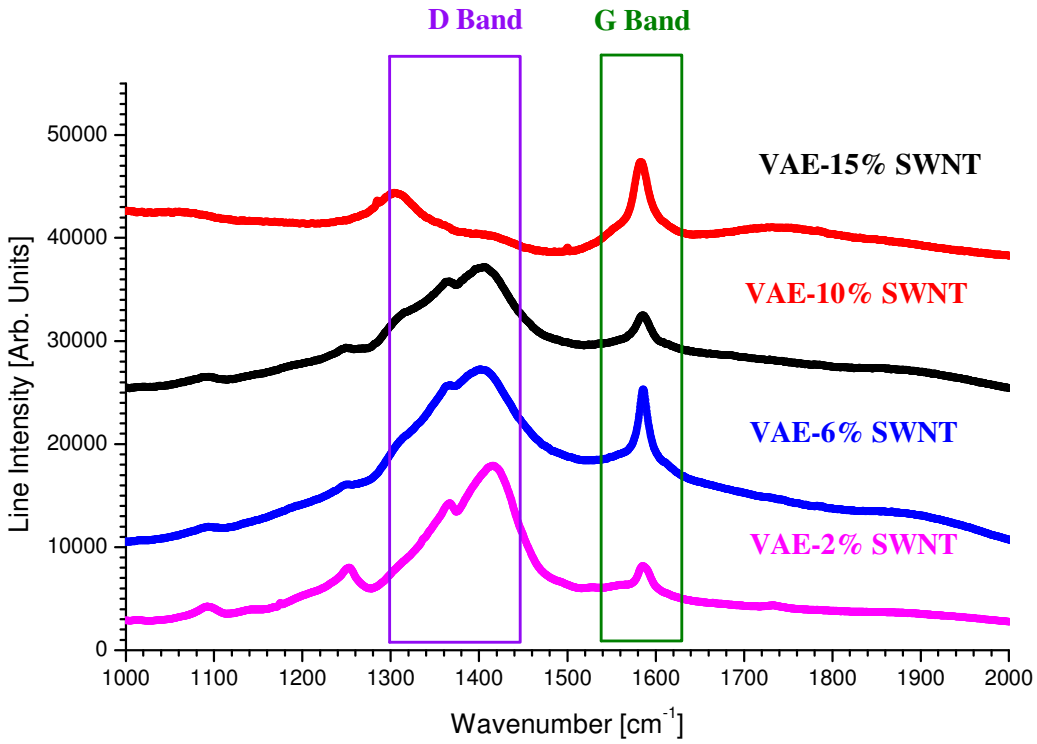

Figure 6.9 Raman spectrum from SWNT/VAE composites at 4 different concentrations.

6.3.3 Atomic Force Microscope Characterization

The tapping mode of atomic force microscope, Figure 6.10, is used to characterize the surface roughness of the composite at SWNT concentration of 2wt%, 6wt%, 10wt%, 15wt%. We obtain both average roughness and root mean square roughness from the AFM software calculation.

The value of R_a, average roughness, represents the arithmetic average of the height of the roughness irregularities above the mean line along the sample length.

$$R_a = \frac{y_1 + y_2 + y_3 + \ldots + y_n}{n} \qquad \textbf{Equation 6.1}$$

The roughness parameter R_q represents the root mean square (RMS) of the peak heights and is more sensitive to the occurrence of the occasional high and low points.

$$R_q = \sqrt{\frac{y_1^2 + y_2^2 + y_3^2 + \ldots . y_n^2}{n}} \qquad \textbf{Equation 6.2}$$

(a)AFM probe from Veeco company

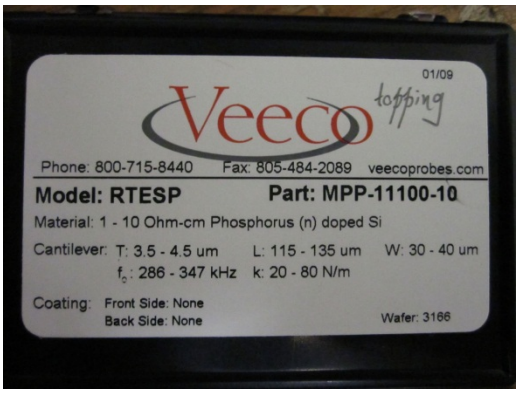

(b) Probe specifications

(c) Fixing probe on the AFM amount

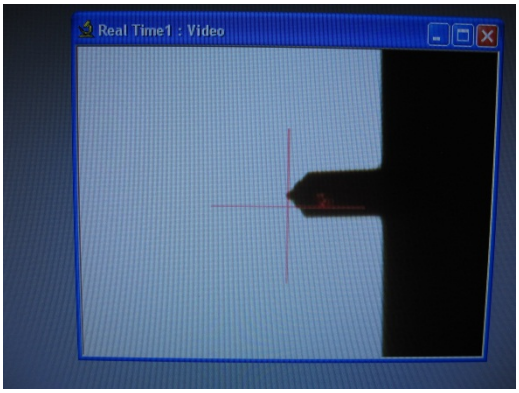

(d) the probe under optical microscope

Figure 6.10 Surface roughness testing by Atomic Force Microscope from Veeco.

The trace and retrace line can be used to check if the probe and sample surface tracks well. We adjust the scanning parameters and came up with the trace and retrace line like showed in Figure 6.11, meaning the AFM tip kept tracking the surface all the time. It is inferred that the higher loading of nanotube might have influence on the system viscosity during the high pressure processing.

Figure 6.11 AFM trace and retrace line during surface roughness test.

Figure 6.12 is the 3 dimensional surface plot detected by AFM. The probe recorded the height value as a function of position within a 10nm by 10nm square area. It can be clearly seen that the samples with lower SWNT concentration of 2wt% and 6wt% tend to show a smoother surface, while a rougher surface goes with higher SWNT loading. The average roughness and RMS are directly calculated by the software. Two types of roughness with respect to SWNT concentration is showed in Table 6.5 and plotted in Figure 6.13. When the concentration of SWNT goes from 6wt% to 10wt%, both kinds of roughness increase approximately by 4 times.

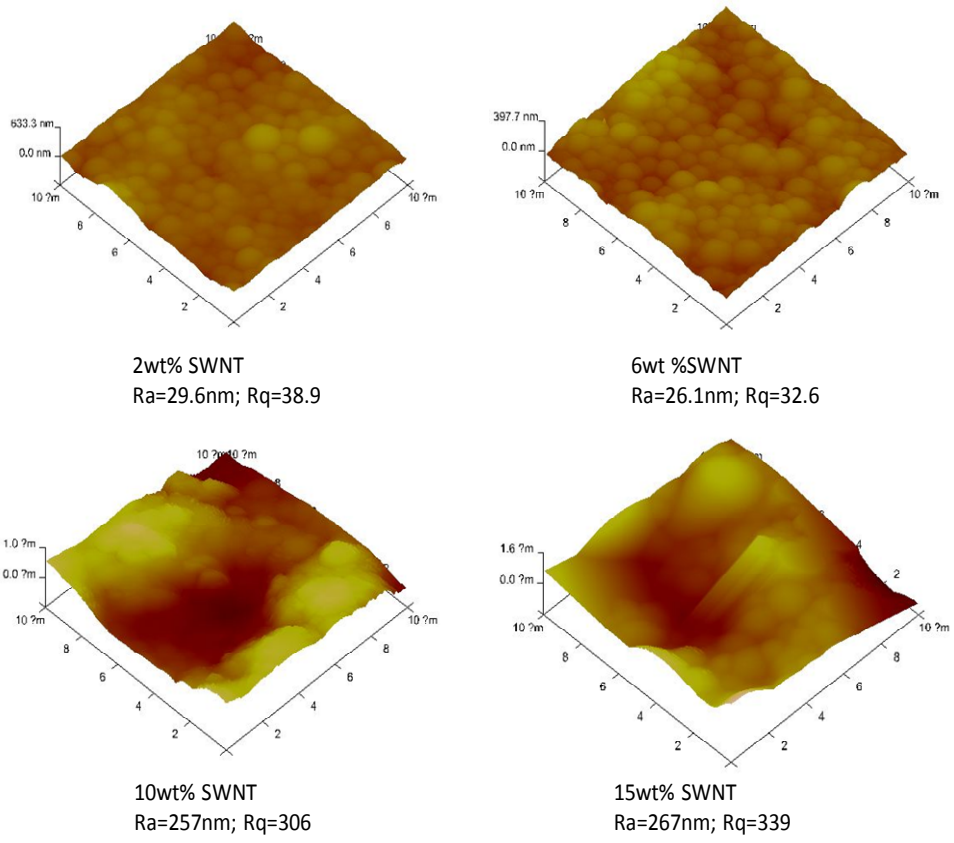

Figure 6.12 3D surface plot of VAE/SWNT composites

SWNT%	R_a(nm)	R_q(nm)
2wt%	29.6	38.9
6wt%	26.1	32.6
10wt%	257	306
15wt%	267	339

Table 6.5 Average roughness and root mean square roughness at different concentrations

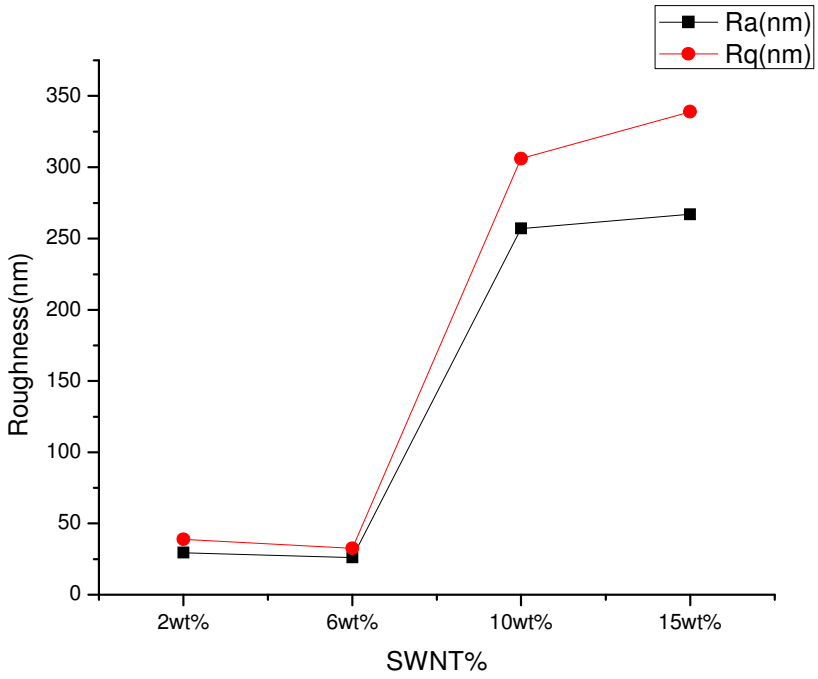

Figure 6.13 Average roughness and root mean square roughness as a function of SWNT concentration.

The 2wt% SWNT sample was taken as an example to evaluate the experimental error of Z value acquisition. Other 3 samples were measured under the same parameters (feedback and scan rate). Figure 6.14 is the topography of 2wt% SWNT sample and height curve along diagonal; Figure 6.15 is the amplitude error of 2wt% SWNT sample along diagonal. When the probe of AFM is scanning across the sample surface, a feedback circuit is applied to keep the tip-sample interaction constant. Amplitude error signal describes difference between the instantaneous amplitude of oscillation and the amplitude setpoint. The amplitude error is zero in perfect situation. But the delay of the feedback always happens in practice. In our case, amplitude error is maintained at (-300,200) mV, which means the feedback gains and scan rate were setup in appropriate values.

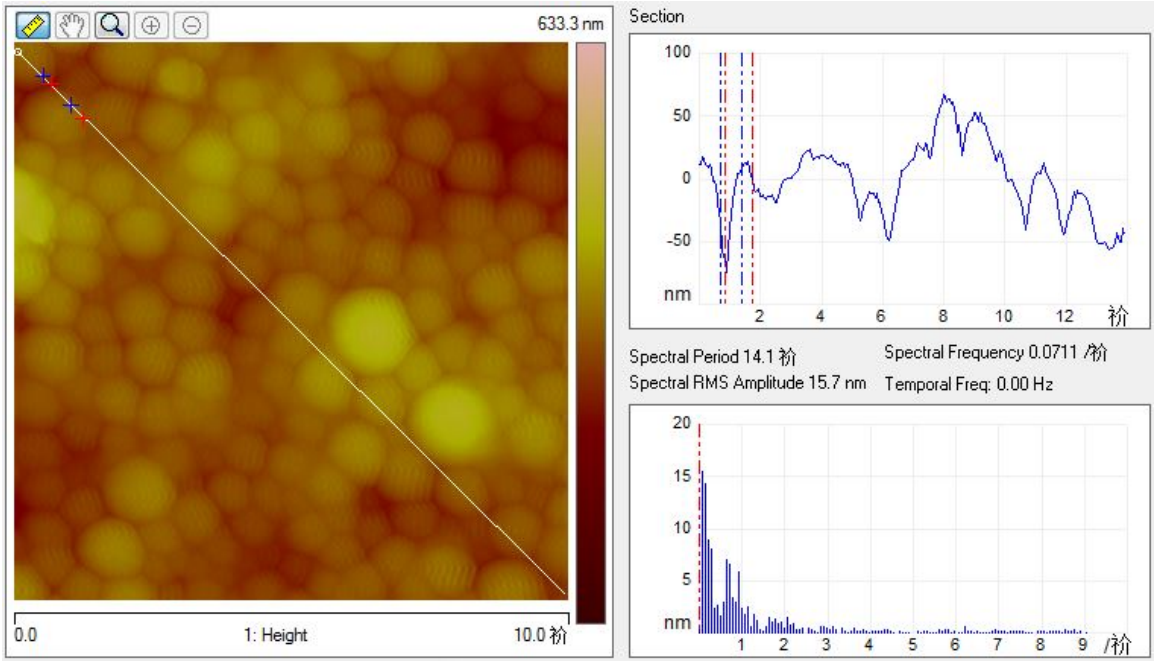

Figure 6.14 Topography of 2wt% SWNT sample and height curve along diagonal.

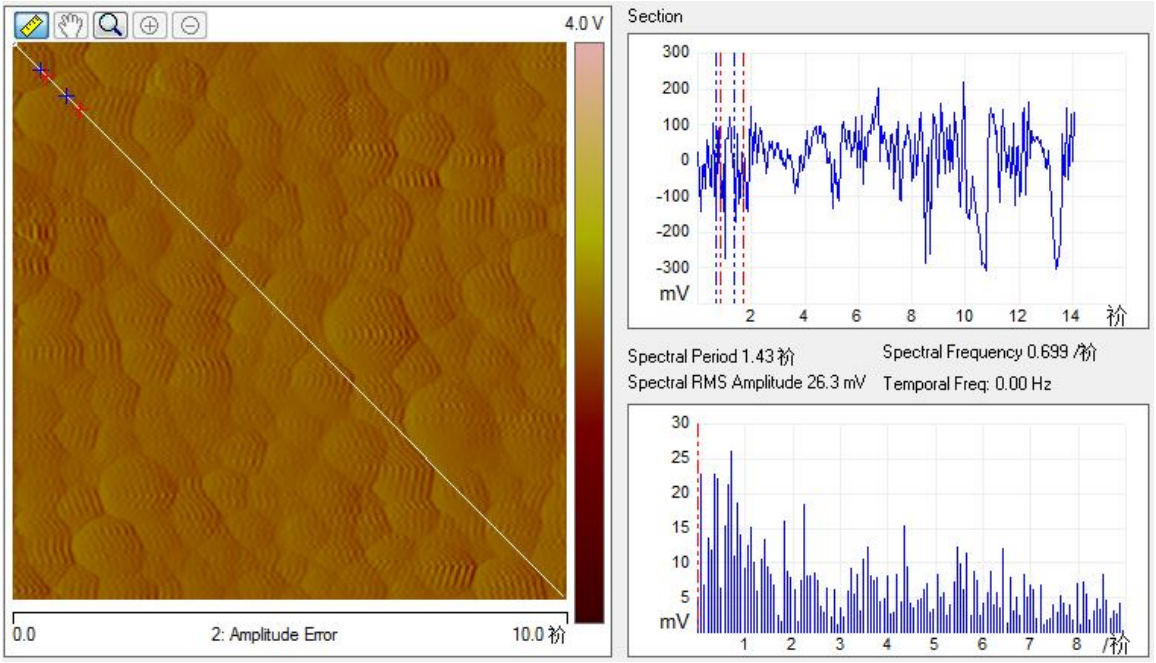

Figure 6.15 Amplitude error of 2wt% SWNT sample along diagonal

6.4 Calculation of Conducting Percolation in SWNT Composites

Excluded volume theory has been approved to be a powerful tool to estimate the conducting percolation threshold of composites containing conducting fillers with high aspect ratios. The goal of this modeling is to find a quantitative relationship between the conducting percolation threshold and the aspect ratio of single wall carbon nanotube. When the loading of conducting filler reach the critical volume fraction, a touching network of the nanotube described in Figure 6.3 can be given in polymer matrix.

The exclude volume of the nanotube in this model is not the true physical volume. Considering we have a single wall carbon nanotube A in 3D space, the excluded volume of this carbon nanotube A is the surrounding space that another some shaped nanotube B passing around A without penetrating A. The percolation threshold is linked to the exclude volume of nanotube A instead of nanotube itself. The connecting network of nanotube in polymer matrix can be formed when the exclude volume of carbon nanotube is equal to the product of total volume of nanotubes at percolation and the critical number density of nanotubes at percolation.

6.4.1 Assumptions

1. The single wall carbon nanotubes have high aspect ratios, $\left(\frac{l}{2r}\right) > 1000$.

2. The carbon nanotubes are considered as capped cylinders, as show in Figure 1.

3. The alignment of carbon nanotube is isotropic in polymer matrix.

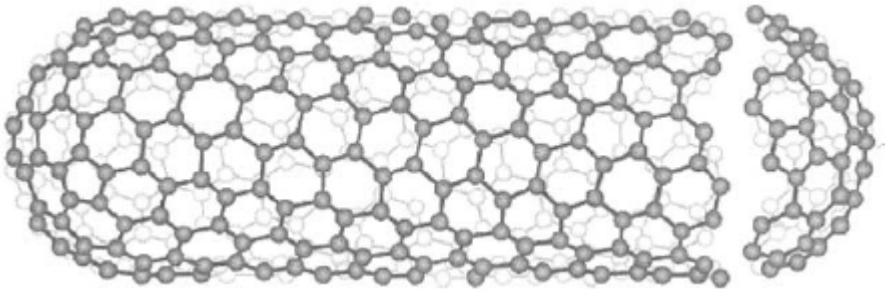

Figure 6.16 Nanotube is shaped as capped cylinder

Parameters

l, length of cylinder

r, radius of cylinder

V_{cyl}, volume of capped cylinder

V_{ex}, excluded volume of capped cylinder in 3D space

ρ_c, the critical number density of capped cylinders at percolation

V_c, total volume of capped cylinders at percolation

ϕ_c, volume fraction of carbon nantubes at percolation

A, aspect ratio

6.4.2 Calculation

Considering the cap as the hemisphere, the volume of capped cylinder is,

$$V_{cyl} = \frac{4}{3}\pi r^3 + \pi l r^2 \qquad \textbf{Equation 6.3}$$

The excluded volume of a capped cylinder in three dimensional space is[83, 84],

$$V_{ex} = \frac{32}{3}\pi r^3 + 8\pi l r^2 + 4l^2 r < \sin(\gamma) > \qquad \textbf{Equation 6.4}$$

According to excluded volume theory[83], the critical number density is inverse of the excluded volume,

$$\rho_c \propto (V_{ex})^{-1} \qquad \textbf{Equation 6.5}$$

Linking the excluded volume and the critical volume fraction[85],

$$\phi_c = 1 - \exp\left(-\frac{V_c V_{cyl}}{V_{ex}}\right) \qquad \textbf{Equation 6.6}$$

The total volume of capped cylinders at percolation[86],

$$V_c = 1.4$$

The volume fraction of nanotube at percolation becomes,

$$\phi_c = 1 - \exp\left(-\frac{1.4\left(\frac{4}{3}\pi r^3 + \pi l r^2\right)}{\frac{32}{3}\pi r^3 + 8\pi l r^2 + 4l^2 r < \sin(\gamma) >}\right) \qquad \textbf{Equation 6.7}$$

Using the isotropic assumption[87], $< \sin(\gamma) >= \frac{\pi}{4}$, above is simplified to

$$\phi_c = 1 - \exp\left(-\frac{1.4\left(\frac{4}{3}\pi r^3 + \pi l r^2\right)}{\frac{32}{3}\pi r^3 + 8\pi l r^2 + \pi l^2 r}\right)$$

Equation 6.8

Substituting aspect ratio$A = \frac{l}{2r}$, the final expression of fraction volume becomes,

$$\phi_c = 1 - \exp\left(-\frac{28 + 42A}{160 + 240A + 60A^2}\right)$$

Equation 6.9

Then we plot the value ϕ_c with respect to aspect ratio A, using the Wolfram Mathematica software, to get the curve as showed in Figure 6.17.

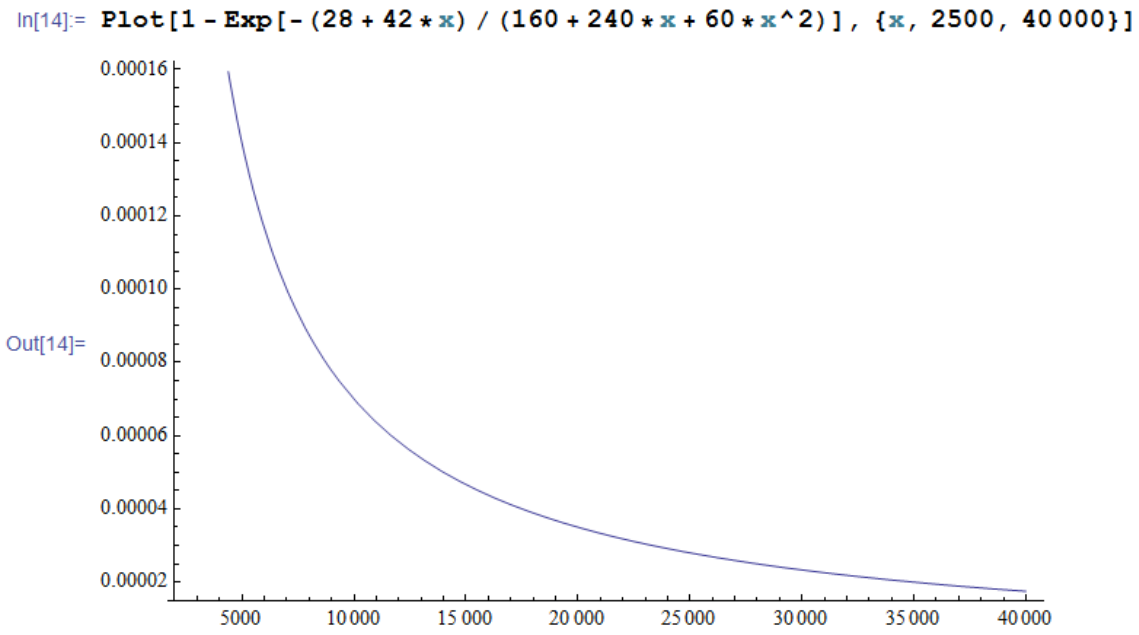

Figure 6.17 Critical volume fraction as a function of aspect ratio

The carbon nanotube we used has a diameter of 1-2nm, and length of 5-30um, as showed in Figure 6.1, which give us the domain of$A \in [2500,30000]$, then$\phi_c \in [2.3 \times 10^{-5}, 2.8 \times 10^{-4}]$.

CHAPTER 7 SUMMARY AND FUTURE WORK

In this thesis, 5 different combinations of nano inclusion and polymer matrix have been investigated. Titanium dioxide and single wall carbon nanotube were used as nano inclusions. The polymer matrix are polyaniline, polystyrene, polyaniline and polystyrene mixture, polyethylene, vinyl acetate-enthylene copolymer. We have applied 2 synthesis methods: in situ polymerization and solution blending. Two types of solution blending methods, sonication and high pressure homogenizer, were used to mix the nano inclusion and polymer. Physical properties like electrical conductivity and thermal conductivity were studied. As for the structure investigation, the interactions between the nano inclusion and polymer matrix and the dispersion of nanotube or nanoparticles have been studied. Detailed information has been summarized in Table 7.1.

Nano inclusion	Polymer matrix	Synthesis method	Research Target
Titanium dioxide	Polyaniline	*in situ* polymerization	Energy conversion efficiency
Titanium dioxide	Polystyrene	solution blending (sonication)	Mathematical simulation on thermal analysis
Titanium dioxide	Polyaniline and polystyrene	solution blending (sonication)	Interaction between nanoparticles and polymer
Titanium dioxide	Polyethylene	solution blending (high pressure homogenizer)	Dispersoin of nanoparticles
Carbon nanotube	Vinyl acetate-enthylene copolymer	solution blending (high pressure homogenizer)	Dispersoin of nanotube and conducting percolation

Table 7.1 Overview of five different composite materials in this thesis

Attapulgite/TiO_2/PANI nano-composites were synthesized by in situ polymerization under different doping-acids (HCl, sulfosalicylic acid (SSA), HCl+SSA dual acids, $HClO_4$).The doping-acids can help with the improvement of microstructure, thermal stability and thermoelectric properties of the composite material. We come up with the result that HCl+SSA gave the biggest boost on electrical conductivity and seebeck coefficient. A higher value of ZT is kept in the range of 323-373 K for the HCl+SSA dual acids doped ATOP nano-composites. The electrical conductivity of nano-composites with HCl+SSA can reach 6.67 S/cm at 373K and exhibit a typical non-metallic temperature dependence and the Seebeck coefficient reachs 57 μV/K at 363K. it is believed that HCl+SSA dual acids have a promising industrial application in power generation over a wide temperature range.

The introduction of anatase titanium dioxide can significantly affects the physical properties of the composite material due to the large surface area of the nanofiller and its interaction with macromolecular chain. TGA analysis can detect the fingerprint of the formation of a polymer –nanoparticle interface.The experimental results show that the temperature at which the mass loss reaches the highest value increases by more than 25℃ as the concentration of the filler is increased up to 11wt%. Further increase of the filler concentration does not resulted in a further increase of the degradation temperature. This demonstrates the formation of an interface between the nanofiller and the nanocomposites. Several mathematical equation were used to simulate the TGA curve. The best fit of the mass derivative dependence on temperature has been obtained for the double Gaussian dependence, which demonstrates that the shape asymmetry implies

different linewidth on the left and on the right of the extreme temperature T_i. WAXS spectra of TiO_2 nanoparticles dispersed within polystyrene at various temperatures ranging from 25 ^oC to 105 ^oC confirms that anatase is the dominant phase.

Polyaniline were added into the polystyrene-TiO_2 system to enhance the electrical conductivity, because of the excellent electrical conductivity and thermal-oxidative stability of polyaniline. TGA data of PS-PANI composites shows that the degradation temperature did not change too much as the concentration of PANI increased from 0wt% to 10wt%, demonstrating that there is no interface formed between the polystyrene and PANI fillers. The TGA results of PS-PANI-TiO_2 shows that the degradation temperature has 25°C with the increasing concentration of TiO_2, implying there is no interaction between TiO_2 nanofillers and PANI fillers. We can conclude that the significant shift of the degradation temperature of PS-PANI-TiO_2 system is mainly caused by the interface between TiO_2 and PS matrix.

High pressure homogenizer was applied to disperse Titanium dioxide into polyethylene matrix. The study was try to figure out the phase transition phenomena like crystallization, melting, and glass transition behavior in polyethylene oxide (PEO) and polyethylene oxide - TiO_2 nanocomposites (PEO-TiO_2). The SEM images of PEO-TiO_2 show that samples with concentrations of TiO2 below 20wt% appears an evenly distributed cluster at the size of 1um-2um. when the loading of TiO_2 went above 20wt%, the cluster size increased significantly. By comparing of these two groups of samples, we can see that the viscosity of the polymer matrix solution has a great influence on the final

cluster size and dispersion of the nanofillers, we successfully maintain the clusters into nanosize up to 30wt% of TiO_2 concentration, this demonstrates that the high pressure method is more efficient than sonication method (reaching up to 11wt% TiO_2 in PS matrix). DSC curve shows that the glass transition temperature was affected by the loading of TiO_2 and the heating rate. DSC curve for PEO-TiO_2 nanocomposites at 5 ^{o}C/min cooling rate shows the dispersion of TiO_2 nanoparticles drops the crystallization temperature of PEO.

The single wall carbon nanotube has excellent carrier mobility of$\sim 10{,}000 cm^2 V^{-1} s^{-1}$, which makes it promising nanofiller for conducting composite material. To make the suspension compatible with high pressure homogenizer, we use Vinyl acetate-ethylene copolymer emulsion because of its water solubility. High pressure homogenizer has been proved to be a much more efficiency method to mix suspension. It just takes Nanodebee 1/60 processing time of sonicator to give a much higher quality sample. Composite sample with single wall carbon nanotube at concentration of 2wt%, 6wt%, 10wt%, 15wt% were tested by Raman spectroscopy. G-band was observed in the Raman spectrum to confirm the existence of single wall carbon nanotubes in the system. The relative intensity of D to G band value showed its maximum of 2.88 at 2wt% SWNT, indicating the higher level of disorder between grapheme layers tend to happen at lower SWNT concentration. Average roughness and root mean square roughness have been obtained from atomic force microscope. Both roughness value show that lower loading of SWNT tends to give a smoother surface. Excluded volume theory was used to calculate the percolation threshold of nanotube composites. We assumed the nanotube as capped

cylinders. Expression of fraction volume was derived as a function of aspect ratio, giving a valuable reference for future design of carbon nanotube/polymer structure.

The research on nano composite materials gives promising future for creating high efficiency new energy equipment. The future work of this subject can be making thermal electric devices to convert heat to electricity or vice versa. Our experiment shows that the HCl+SSA dual acids gave the best boost of ZT value enhancement, but how the introduction of H^+ modify the micro structure of composite system remains unclear. Electrical conductivity measurement of nanotube composite can be conducted in the follow up work to verify the prediction of percolation threshold of single wall carbon nanotube concentration.

REFERENCES

1. Baekeland, L.H., Bakelite, a new composition of matter: Its synthesis, constitution, and uses. Sci. Am., Suppl, 1909. 68: p. 322.

2. Kojima, Y., et al., Mechanical properties of nylon 6-clay hybrid. Journal of Materials Research, 1993. 8(05): p. 1185-1189.

3. Royal, S. and E. Royal Academy of. Nanoscience and nanotechnologies opportunities and uncertainties. 2003; Available from: http://www.nanotec.org.uk/finalReport.htm.

4. Schulten, H.R. and P. Leinweber, Characterization of humic and soil particles by analytical pyrolysis and computer modeling. Journal of analytical and applied pyrolysis, 1996. 38(1-2): p. 1-53.

5. Thostenson, E.T., C. Li, and T.W. Chou, Nanocomposites in context. Composites Science and Technology, 2005. 65(3-4): p. 491-516.

6. Alexandre, M. and P. Dubois, Polymer-layered silicate nanocomposites: preparation, properties and uses of a new class of materials. Materials Science and Engineering: R: Reports, 2000. 28(1-2): p. 1-63.

7. Giannelis, E., R. Krishnamoorti, and E. Manias, Polymer-silicate nanocomposites: model systems for confined polymers and polymer brushes. Polymers in confined environments, 1999: p. 107-147.

8. Dresselhaus, M.S., G. Dresselhaus, and P. Eklund, Science of fullerenes and carbon nanotubes. 1996: Academic Pr.

9. Dresselhaus, M.S., et al., Raman spectroscopy of carbon nanotubes. Physics Reports, 2005. 409(2): p. 47-99.

10. Lau, A.K.-T. and D. Hui, The revolutionary creation of new advanced materials—carbon nanotube composites. Composites Part B: Engineering, 2002. 33(4): p. 263-277.

11. Wilder, J.W.G., et al., Electronic structure of atomically resolved carbon nanotubes. Nature, 1998. 391(6662): p. 59-62.

12. Iijima, S., Helical microtubules of graphitic carbon. Nature, 1991. 354(6348): p. 56-58.

13. Rinzler, A., et al., Unraveling nanotubes: field emission from an atomic wire. Science, 1995. 269(5230): p. 1550-1553.

14. De Heer, W.A., A. Chatelain, and D. Ugarte, A carbon nanotube field-emission electron source. Science, 1995. 270(5239): p. 1179-1180.

15. Collins, P.G., et al., Nanotube nanodevice. Science, 1997. 278(5335): p. 100-102.

16. Kelly, B.T., Physics of graphite. 1981: Applied Science Publishers.

17. Jian Ping, L., Elastic properties of single and multilayered nanotubes. Journal of Physics and Chemistry of Solids, 1997. 58(11): p. 1649-1652.

18. Wong, E.W., P.E. Sheehan, and C.M. Lieber, Nanobeam Mechanics: Elasticity, Strength, and Toughness of Nanorods and Nanotubes. Science, 1997. 277(5334): p. 1971-1975.

19. Binnig, G., C.F. Quate, and C. Gerber, Atomic force microscope. Physical Review Letters, 1986. 56(9): p. 930-933.

20. Barber, A.H., et al., Fracture Transitions at a Carbon-Nanotube/Polymer Interface. Advanced Materials, 2006. 18(1): p. 83-87.

21. Losic, D., et al., AFM Nanoindentations of Diatom Biosilica Surfaces. Langmuir, 2007. 23(9): p. 5014-5021.

22. Rao, A.M., et al., Diameter-Selective Raman Scattering from Vibrational Modes in Carbon Nanotubes. Science, 1997. 275(5297): p. 187-191.

23. Cooper, C.A., R.J. Young, and M. Halsall, Investigation into the deformation of carbon nanotubes and their composites through the use of Raman spectroscopy. Composites Part A: Applied Science and Manufacturing, 2001. 32(3–4): p. 401-411.

24. Schadler, L.S., S.C. Giannaris, and P.M. Ajayan, Load transfer in carbon nanotube epoxy composites. Applied Physics Letters, 1998. 73(26): p. 3842-3844.

25. Balazs, A.C., T. Emrick, and T.P. Russell, Nanoparticle Polymer Composites: Where Two Small Worlds Meet. Science, 2006. 314(5802): p. 1107-1110.

26. Wise, K.E., et al., Stable dispersion of single wall carbon nanotubes in polyimide: the role of noncovalent interactions. Chemical Physics Letters, 2004. 391(4): p. 207-211.

27. Badaire, S., et al., In Situ Measurements of Nanotube Dimensions in Suspensions by Depolarized Dynamic Light Scattering. Langmuir, 2004. 20(24): p. 10367-10370.

28. Bauer, B.J., E.K. Hobbie, and M.L. Becker, Small-Angle Neutron Scattering from Labeled Single-Wall Carbon Nanotubes. Macromolecules, 2006. 39(7): p. 2637-2642.

29. Schaefer, D.W., et al., Morphology of dispersed carbon single-walled nanotubes. Chemical Physics Letters, 2003. 375(3): p. 369-375.

30. Xie, X.L., Y.W. Mai, and X.P. Zhou, Dispersion and alignment of carbon nanotubes in polymer matrix: a review. Materials Science and Engineering: R: Reports, 2005. 49(4): p. 89-112.

31. Moniruzzaman, M. and K.I. Winey, Polymer Nanocomposites Containing Carbon Nanotubes. Macromolecules, 2006. 39(16): p. 5194-5205.

32. Islam, M.F., et al., High Weight Fraction Surfactant Solubilization of Single-Wall Carbon Nanotubes in Water. Nano Letters, 2003. 3(2): p. 269-273.

33. Bryning, M.B., et al., Thermal conductivity and interfacial resistance in single-wall carbon nanotube epoxy composites. Applied Physics Letters, 2005. 87(16): p. 161909-3.

34. Gong, X., et al., Surfactant-Assisted Processing of Carbon Nanotube/Polymer Composites. Chemistry of Materials, 2000. 12(4): p. 1049-1052.

35. Ishida, H. and T. Agag, Handbook of Benzoxazine Resins. 2011: Elsevier Science.

36. Brostow, W., Performance of plastics. 2000: Hanser/Gardner Publications.

37. Qian, D., et al., Load transfer and deformation mechanisms in carbon nanotube-polystyrene composites. Applied Physics Letters, 2000. 76: p. 2868.

38. Haggenmueller, R., et al., Aligned single-wall carbon nanotubes in composites by melt processing methods. Chemical Physics Letters, 2000. 330(3–4): p. 219-225.

39. Kumar, S., et al., Fibers from polypropylene/nano carbon fiber composites. Polymer, 2002. 43(5): p. 1701-1703.

40. Kumar, S., et al., Synthesis, Structure, and Properties of PBO/SWNT Composites&. Macromolecules, 2002. 35(24): p. 9039-9043.

41. Siochi, E.J., et al., Melt processing of SWCNT-polyimide nanocomposite fibers. Composites Part B: Engineering, 2004. 35(5): p. 439-446.

42. Bhattacharyya, A.R., et al., Crystallization and orientation studies in polypropylene/single wall carbon nanotube composite. Polymer, 2003. 44(8): p. 2373-2377.

43. Robeson, L.M., Polymer blends: a comprehensive review. 2007: Hanser.

44. Calvert, P., Nanotube composites: A recipe for strength. Nature, 1999. 399(6733): p. 210-211.

45. Xie, X.-L., Y.-W. Mai, and X.-P. Zhou, Dispersion and alignment of carbon nanotubes in polymer matrix: A review. Materials Science and Engineering: R: Reports, 2005. 49(4): p. 89-112.

46. Miyagawa, H., M. Misra, and A.K. Mohanty, Mechanical Properties of Carbon Nanotubes and Their Polymer Nanocomposites. Journal of Nanoscience and Nanotechnology, 2005. 5(10): p. 1593-1615.

47. Zhu, J., et al., Improving the Dispersion and Integration of Single-Walled Carbon Nanotubes in Epoxy Composites through Functionalization. Nano Letters, 2003. 3(8): p. 1107-1113.

48. Moniruzzaman, M., et al., Increased flexural modulus and strength in SWNT/epoxy composites by a new fabrication method. Polymer, 2006. 47(1): p. 293-298.

49. Lu, J.P., Elastic properties of single and multilayered nanotubes. Journal of Physics and Chemistry of Solids, 1997. 58(11): p. 1649-1652.

50. Li, F., et al., Tensile strength of single-walled carbon nanotubes directly measured from their macroscopic ropes. Applied Physics Letters, 2000. 77(20): p. 3161-3163.

51. Sales, B.C., THERMOELECTRIC MATERIALS: Smaller Is Cooler. Science, 2002. 295(5558): p. 1248-1249.

52. Su, L. and Y.X. Gan, Formation and thermoelectric property of TiO_2 nanotubes covered by Te–Bi–Pb nanoparticles. Electrochimica Acta, 2011. 56(16): p. 5794-5803.

53. Ghosh, P., S.K. Siddhanta, and A. Chakrabarti, Characterization of poly(vinyl pyrrolidone) modified polyaniline prepared in stable aqueous medium. European Polymer Journal, 1999. 35(4): p. 699-710.

54. Liang, J. and F. Li, Heat transfer in polymer composites filled with inorganic hollow micro-spheres: A theoretical model. Polymer Testing, 2007. 26(8): p. 1025-1030.

55. Park, O.K., et al., Effects of the surface treatment on the properties of polyaniline coated carbon nanotubes/epoxy composites. Composites Part B: Engineering, 2010. 41(1): p. 2-7.

56. Liang, J.Z., Predictions of tensile strength of short inorganic fibre reinforced polymer composites. Polymer Testing, 2011.

57. Vu, Q.T., et al., Electrophoretic deposition of nanocomposites formed from polythiophene and metal oxides. Electrochimica Acta, 2005. 51(6): p. 1117-1124.

58. Song, R.Y., et al., Supercapacitive properties of polyaniline/Nafion/hydrous RuO< sub> 2</sub> composite electrodes. Journal of Power Sources, 2007. 166(1): p. 297-301.

59. Li, H., et al., Theoretical and experimental specific capacitance of polyaniline in sulfuric acid. Journal of Power Sources, 2009. 190(2): p. 578-586.

60. Mandic, Z., M.K. Rokovic, and T. Pokupcic, Polyaniline as cathodic material for electrochemical energy sources:: The role of morphology. Electrochimica Acta, 2009. 54(10): p. 2941-2950.

61. Angelopoulos, M., N. Patel, and R. Saraf, Amic acid doping of polyaniline: characterization and resulting blends. Synthetic Metals, 1993. 55(2): p. 1552-1557.

62. Palaniappan, S., et al., Mannich-type reaction in solvent free condition using reusable polyaniline catalyst. Journal of Molecular Catalysis A: Chemical, 2004. 218(1): p. 47-53.

63. Bernard, M.C., et al., Study by optical multichannel analysis of the electrochromic phenomena in polyaniline doped with camphorsulfonic acid. Synthetic Metals, 1996. 81(2-3): p. 215-219.

64. Chen, S.A., Y. Fang, and H.T. Lee, Polyacrylic acid-doped polyaniline as p-type semiconductor in Schottky barrier electronic device. Synthetic Metals, 1993. 57(1): p. 4082-4086.

65. Van Olphen, H. and J. Fripiar, Data handbook for clay materials and other non-metallic minerals. Soil Science, 1981. 131(1): p. 62.

66. Yang, C. and P. Liu, Core-shell attapulgite@ polypyrrole composite with well-defined corn cob-like morphology via self-assembling and in situ oxidative polymerization. Synthetic Metals, 2009. 159(19): p. 2056-2062.

67. Wang, L. and J. Sheng, Preparation and properties of polypropylene/org-attapulgite nanocomposites. Polymer, 2005. 46(16): p. 6243-6249.

68. Stafström, S. and J. Brédas, Evolution of structure and electronic properties in oxidized polyaniline as a function of the torsion angle between adjacent rings. Synthetic Metals, 1986. 14(4): p. 297-308.

69. Li, J., et al., Synthesis and thermoelectric properties of hydrochloric acid-doped polyaniline. Synthetic Metals, 2010. 160(11): p. 1153-1158.

70. Zhu, P., et al., Carrier-Concentration-Dependent Transport and Thermoelectric Properties of PbTe Doped with Sb 2 Te 3. Materials transactions, 2005. 46(12): p. 2690-2693.

71. Mateeva, N., et al., Correlation of Seebeck coefficient and electric conductivity in polyaniline and polypyrrole. Journal of Applied Physics, 1998. 83: p. 3111.

72. De Albuquerque, J., W. Melo, and R. Faria, Determination of physical parameters of conducting polymers by photothermal spectroscopies. Review of scientific instruments, 2003. 74: p. 306.

73. Sun, Y., et al., A three-in-one improvement in thermoelectric properties of polyaniline brought by nanostructures. Synthetic Metals, 2010. 160(21): p. 2371-2376.

74. Maekawa, T., et al., Thermal conductivity of titanium dioxide films grown by metal-organic chemical vapor deposition. Surface and Coatings Technology, 2008. 202(13): p. 3067-3071.

75. Avrami, M., Kinetics of Phase Change. I General Theory. The Journal of Chemical Physics, 1939. 7(12): p. 1103-1112.

76. Hwang, Y., et al., Production and dispersion stability of nanoparticles in nanofluids. Powder Technology, 2008. 186(2): p. 145-153.

77. Floury, J., A. Desrumaux, and J. Lardières, Effect of high-pressure homogenization on droplet size distributions and rheological properties of model oil-in-water emulsions. Innovative Food Science & Emerging Technologies, 2000. 1(2): p. 127-134.

78. Håkansson, A., C. Trägårdh, and B. Bergenståhl, Dynamic simulation of emulsion formation in a high pressure homogenizer. Chemical Engineering Science, 2009. 64(12): p. 2915-2925.

79. Zhou, X., et al., Band Structure, Phonon Scattering, and the Performance Limit of Single-Walled Carbon Nanotube Transistors. Physical Review Letters, 2005. 95(14): p. 146805.

80. Bradley, K., J.-C.P. Gabriel, and G. Grüner, Flexible Nanotube Electronics. Nano Letters, 2003. 3(10): p. 1353-1355.

81. Dai, H., et al., Electrical transport properties and field-effect transistors of carbon nanotubes. NANO: Brief Reports and Reviews, 2006. 1(1): p. 1-4.

82. Azoubel, S. and S. Magdassi, The formation of carbon nanotube dispersions by high pressure homogenization and their rapid characterization by analytical centrifuge. Carbon, 2010. 48(12): p. 3346-3352.

83. Balberg, I., et al., Excluded volume and its relation to the onset of percolation. Physical Review B, 1984. 30(7): p. 3933-3943.

84. Balberg, I., N. Binenbaum, and N. Wagner, Percolation Thresholds in the Three-Dimensional Sticks System. Physical Review Letters, 1984. 52(17): p. 1465-1468.

85. Balberg, I., Excluded-volume explanation of Archie's law. Physical Review B, 1986. 33(5): p. 3618-3620.

86. Balberg, I., Universal percolation-threshold limits in the continuum. Physical Review B, 1985. 31(6): p. 4053-4055.

87. Celzard, A., et al., Critical concentration in percolating systems containing a high-aspect-ratio filler. Physical Review B, 1996. 53(10): p. 6209-6214.

VITA

Yun Zhai was born in Yantai, ShanDong province of China on April 14th, 1983. He was awarded with a Bachelor degree in Material Science and Engineering by Southwest JiaoTong University in 2006. Then he continued his study on Material Science in Southwest JiaoTong University and received his Master degree in 2008. In January 2009, he moved to University of New Orleans to purse his PhD in Engineering and Applied Science under the supervision of Prof. David Hui.